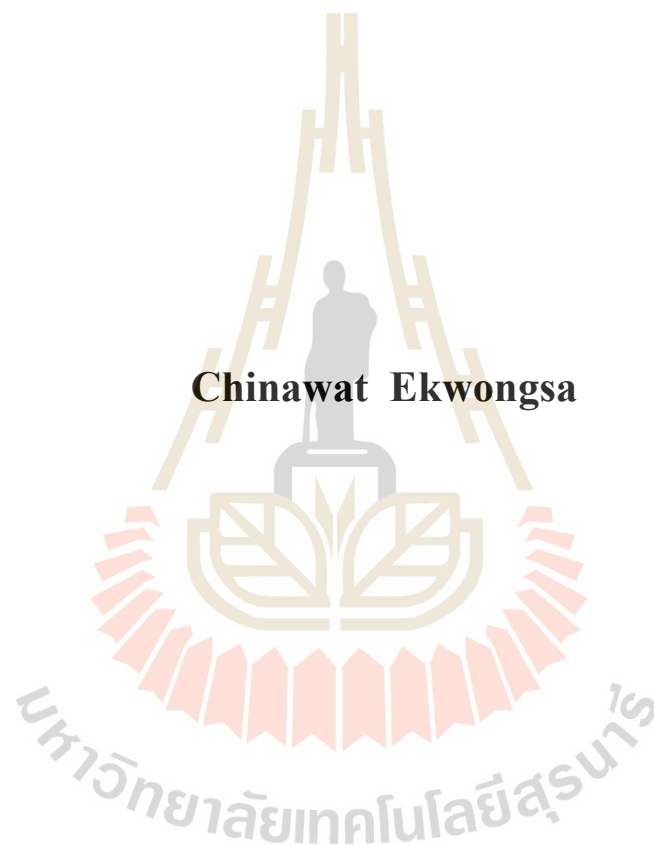


**DEVELOPMENT OF *in situ* TEMPERATURE
DEPENDENT X-RAY ABSORPTION SPECTROSCOPY**



Chinawat Ekwongsa

**A Thesis Submitted in Partial Fulfillment of the Requirements for the
Degree of Doctor of Philosophy in Applied Physics**

Suranaree University of Technology

Academic Year 2020

การพัฒนาเทคนิคสเปกโทรสโกปีการดูดกลืนด้วยรังสีเอกซ์แบบ *in situ*
ที่ขึ้นกับอุณหภูมิ



วิทยานิพนธ์นี้เป็นส่วนหนึ่งของการศึกษาตามหลักสูตรปริญญาวิทยาศาสตรดุษฎีบัณฑิต
สาขาวิชาฟิสิกส์ประยุกต์
มหาวิทยาลัยเทคโนโลยีสุรนารี
ปีการศึกษา 2563

**DEVELOPMENT OF *in situ* TEMPERATURE DEPENDENT
X-RAY ABSORPTION SPECTROSCOPY**

Suranaree University of Technology has approved this thesis submitted in partial fulfillment of the requirements for the Degree of Doctor of Philosophy.

Thesis Examining Committee



(Assoc. Prof. Dr. Panomsak Meemon)

Chairperson



(Assoc. Prof. Dr. Prayoon Songsiriritthigul)

Member



(Assoc. Prof. Dr. Saroj Rujirawat)

Member



(Dr. Pinit Kidkhunthod)

Member



(Prof. Dr. Rattikorn Yimnirun)

Member


(Assoc. Prof. Dr. Chatchai Jothityangkoon)

Vice Rector for Academic Affairs
and Quality Assurance

(Prof. Dr. Santi Maensiri)

Dean of Institute of Science

ฉันทน์ เอกวงษา : การพัฒนาเทคนิคสเปกโทรสโกปีการดูดกลืนด้วยรังสีเอกซ์แบบ *in situ* ที่ขึ้นกับอุณหภูมิ (DEVELOPMENT OF *in situ* TEMPERATURE DEPENDENT X-RAY ABSORPTION SPECTROSCOPY). อาจารย์ที่ปรึกษา : รองศาสตราจารย์ ดร.ประยูร ส่งศิริฤทธิกุล, 129 หน้า

วิทยานิพนธ์นี้มุ่งเน้นการพัฒนาเทคนิคการดูดกลืนรังสีเอกซ์ (XAS) แบบ *in situ* เพื่อตรวจสอบสถานะออกซิเดชันและโครงสร้างเฉพาะบริเวณของอะตอมที่สนใจในวัสดุที่มีการเปลี่ยนแปลงขึ้นกับอุณหภูมิ ณ ระบบลำแสงที่ 5.2 ซึ่งเป็นสถานีร่วมวิจัยของมหาวิทยาลัยเทคโนโลยีสุรนารี ศูนย์นาโนเทคโนโลยีแห่งชาติ และสถาบันวิจัยแสงซินโครตรอน (องค์การมหาชน) ในงานนี้ได้ออกแบบสร้างและทดสอบอุปกรณ์สำหรับการติดตั้งสารตัวอย่างสำหรับการวัดแบบ *in situ* เรียบร้อยแล้ว อุปกรณ์ดังกล่าวสามารถสร้างสภาพแวดล้อมสำหรับตัวอย่างของเทคนิคการดูดกลืนด้วยรังสีเอกซ์ให้อยู่ในบรรยากาศของก๊าซที่ต้องการ และอุณหภูมิ ตั้งแต่อุณหภูมิห้องจนถึง 1000 องศาเซลเซียส ในการทดสอบการใช้งานอุปกรณ์ดังกล่าว ได้มีการเลือกใช้สารตัวอย่างคือ เหล็กออกไซด์ (FeO) ลิเทียมโคบอลต์ออกไซด์ (LiCoO₂) และโคบอลต์เฟอร์ไรต์ (CoFe₂O₄) เนื่องจากมีต้นทุนที่ต่ำ สามารถจัดหาได้ง่าย และที่สำคัญมีการใช้งานในอุตสาหกรรมแบตเตอรี่ และฮาร์ดดิสก์

จากการวิเคราะห์สเปกตรัมการดูดกลืนรังสีเอกซ์ บริเวณใกล้ระดับชั้น K ของอะตอมเหล็ก พบว่ามีการเปลี่ยนแปลงลักษณะสเปกตรัม โดยขอบการดูดกลืนแสงมีการขยับสูงขึ้นตามพลังงานโฟตอนกระตุ้น ซึ่งบ่งชี้ว่ามีการเพิ่มขึ้นของเลขออกซิเดชันของอะตอมเหล็กในวัสดุ การวิเคราะห์เชิงปริมาณเลขออกซิเดชันของเหล็กถูกกำหนดโดยการคำนวณเชิงปริมาณตามการขยับของขอบการดูดกลืนเปรียบเทียบกับตัวอย่างมาตรฐาน (FeO และ Fe₂O₃) พบว่าเลขออกซิเดชันมีค่าเพิ่มขึ้นเป็นเส้นตรงจาก 2.00+ เป็น 2.65+ เมื่ออุณหภูมิเพิ่มขึ้นจากอุณหภูมิห้องเป็น 800 องศาเซลเซียส และคงที่เมื่ออุณหภูมิสูงขึ้น

จากการศึกษาโครงสร้างผลึกของ LiCoO₂ โดยเทคนิคการเลี้ยวเบนรังสีเอกซ์ (XRD) และ XAS ถูก พบว่า มีสัดส่วนของผลึก LiCoO₂ เพิ่มขึ้นตามอุณหภูมิของการเผาที่เพิ่มขึ้น สเปกตรัมของ XANES ที่ขอบการดูดกลืนชั้น K ของอะตอมโคบอลต์แสดงให้เห็นถึงการเลื่อนของขอบพลังงานการดูดกลืนทในทิศทางลดลงของพลังงานในลักษณะเป็นเส้นตรงเมื่ออุณหภูมิ

เพิ่มขึ้น ในงานนี้ได้ทำการศึกษาผลของอุณหภูมิที่มีต่อการโครงสร้างรอบอะตอมของ Co ในผง LiCoO_2 โดยการวิเคราะห์สเปกตรัมบริเวณใกล้ขอบการดูดกลืนและบริเวณที่ห่างจากขอบการดูดกลืนของชั้น K ของอะตอม Co พบว่าสเปกตรัมรอบขอบพลังงานการดูดกลืนมีการเลื่อนในทิศที่มีการลดลงของพลังงานเป็นเส้นตรงเมื่ออุณหภูมิเพิ่มขึ้น ซึ่งเป็นผลจากการลดลงของเลขออกซิเดชันของ Co จาก Co^{3+} ไปเป็น Co^{2+} นอกจากนี้ ผลวิเคราะห์ของสเปกตรัม EXAFS ยังให้หลักฐานที่ชัดเจนเกี่ยวกับความยาวพันธะที่เพิ่มขึ้นเมื่ออุณหภูมิสูงขึ้น

การเกิดเฟสของโคบอลต์เฟอร์ไรท์ได้รับการตรวจสอบโดยเทคนิค XRD และ XAS พบว่า สัดส่วนปริมาณของผลึก CoFe_2O_4 เพิ่มขึ้นตามอุณหภูมิการเผาผนึก สเปกตรัม XANES ที่รอบขอบพลังงานการดูดกลืนของชั้น K ของอะตอม โคบอลต์และเหล็กแสดงการลดลงเชิงเส้นตรงของขอบพลังงานการดูดกลืนเมื่ออุณหภูมิมิค่าเพิ่มขึ้น ซึ่งเป็นผลเนื่องจากการลดลงของเลขออกซิเดชันของโคบอลต์และเหล็ก



สาขาวิชาฟิสิกส์

ปีการศึกษา 2563

ลายมือชื่อนักศึกษา จิรวรรณ เอมองดา

ลายมือชื่ออาจารย์ที่ปรึกษา อภิสิทธิ์

ลายมือชื่ออาจารย์ที่ปรึกษาร่วม กวีสิทธิ์ กวีสิทธิ์

ลายมือชื่ออาจารย์ที่ปรึกษาร่วม นิพนธ์ กวีสิทธิ์

CHINAWAT EKWONGSA : DEVELOPMENT OF *in situ* TEMPERATURE
DEPENDENT X-RAY ABSORPTION SPECTROSCOPY. THESIS ADVISOR
: ASSOC. PROF. PRAYOON SONGSIRIRITTHIGUL, Ph.D. 129 PP.

DEVELOPMENT/LOCAL STRUCTURE/XANES/EXAFS

This thesis focused on the development *in situ* X-ray absorption spectroscopy techniques for determining temperature-dependent oxidation state and local structural of interested atoms in materials at the SUT-NANOTEC-SLRI beamline (BL5.2) at the Synchrotron Light Research Institute. An *in situ* cell for XAS measurements was successfully designed, constructed and tested. The cell provides environments for XAS samples to be in required gas species atmosphere and at any temperature ranging from room temperature to 1000 °C. In commissioning test of this home-developed temperature-dependent XAS set up, Iron oxide (FeO), lithium cobalt oxide (LiCoO₂) and cobalt ferrite (CoFe₂O₄) were used mainly due to its low cost, commercial availability, and more importantly, its applications in batteries and hard disks industries.

Fe K-edge XANES spectra were taken and analyzed. The results showed that there are gradual changes in feature in the XANES and the shift in absorption edge towards higher with increasing excitation photon energy, indicating the increase in the average oxidation state of Fe atoms in the materials. Quantitative analysis of the valence states of Fe was determined performed using the empirical edge-shift calculations making with comparisons to known standard samples (FeO and Fe₂O₃). The oxidation state was found to increase linearly from +2.00 to +2.65 when the temperature increases from room temperature to 800 °C and remains constant at higher temperatures.

X-ray diffraction (XRD) was used, along with X-ray absorption spectroscopy (XAS), to study the crystal structure of LiCoO_2 . The XRD results indicate that the concentration of LiCoO_2 crystals increases with sintering temperature. The XANES spectra at the Co K-edge show a linearly decrease of the absorption edge energy when increasing temperature. Temperature-dependent on local structure of the LiCoO_2 powders was successfully studied *in situ* by the analyses of the *in situ* Co K-edges taken XANES and EXAFS spectra. The XANES spectra at the Co K-edge show a linearly decrease of edge energy when increasing temperature. This is consistent with a reduction in the Co oxidation state from higher Co^{3+} to Co^{2+} . Additionally, the EXAFS data provide the clear evidence of the increasing bond lengths with temperature.

In the cobalt ferrite system, the phase information was investigated by XRD and XAS techniques. It was found that the concentration of CoFe_2O_4 crystals increases with the sintering temperature. The XANES spectra at Co K-edge and Fe K-edge show a linear decrease of edge energy during increasing temperature. This is consistent with a reduction in Co and Fe oxidation state.

School of Physics

Academic Year 2020

Student's signature Chinawat Ekwongsa

Advisor's signature Song Rajirawat

Co-advisor's signature Pimit U.

Co-advisor's signature Pimit U.

ACKNOWLEDGEMENTS

There are many people, to whom I would like to express my sincere words of acknowledgments:

I thank Assoc. Prof. Dr. Prayoon Songsiriritthigul, my thesis advisor, for introducing me to the field of synchrotron x-ray absorption spectroscopy. He supervised this work in all steps, from the very first experiments, new ideas, data processing as well as the final proof reading of the manuscript. Throughout my works, not only his technical competence, but also his optimism and trust, were a wonderful support and inspiration.

I thank Assoc. Prof. Dr. Saroj Rujirawat and Dr. Pinit Kidkhunthod, my thesis co-advisor abroad.

I am grateful to Assoc. Prof. Dr. Rattikorn Yimnirun for his contribution in my work and for accepting me to be a member of his group.

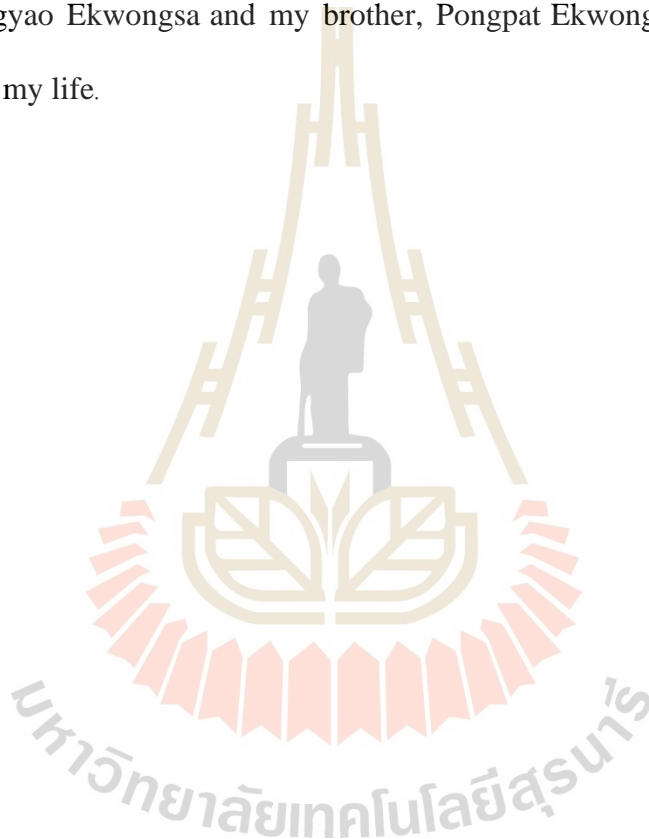
I am grateful to Dr. Pinit Kidkhunthod for his management of beam time in my work at BL-5.2 Synchrotron Light Research Institute. I thank him for his great contribution in bringing up new questions and ideas of X-ray Absorption technique. Special thanks to Mr. Somboonsup Rodporn, Mr. Sujinda Chaiyachad and Dr. Manoon Suttapun for their kind assistance in materials synthesis, XAS measurements, and data analysis and Miss Wilawan Mukdamuang for her love and encouragement.

I am grateful to the Development and Promotion of Science and Technology Talents Project (DPST) from Thai Government for financial support.

It is impossible to list all of my fellow graduate students that were a great support during my Ph.D. study, for all the great times we had together.

Finally, this thesis is dedicated to my parents: my father, Guson Ekwongsa; my mother, Nongyao Ekwongsa and my brother, Pongpat Ekwongsa for their love and everything in my life.

Chinawat Ekwongsa



CONTENTS

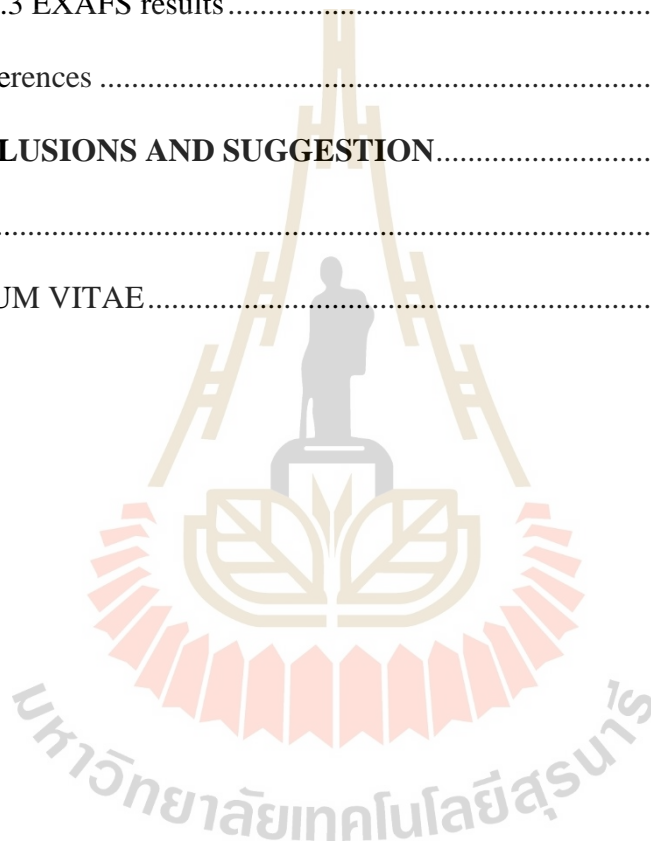
	Page
ABSTRACT IN THAI.....	I
ABSTRACT IN ENGLISH	III
ACKNOWLEDGEMENTS.....	V
CONTENTS.....	VII
LIST OF TABLES	X
LIST OF FIGURES	XI
LIST OF ABBREVIATIONS.....	XV
CHAPTER	
I INTRODUCTION	1
II REVIEW OF LITERATURES	8
2.1 X-ray Absorption Spectroscopy (XAS)	8
2.1.1 X-ray Absorption Near Edge Structure (XANES).....	14
2.1.2 Extended X-ray Absorption Fine Structure (EXAFS)	19
2.2 Lithium cobalt oxide	23
2.3 Cobalt ferrite.....	25
2.4 References	27
III RESEARCH METHODOLOGY	31
3.1 Materials and preparation.....	31
3.1.1 Ferrous oxide.....	31
3.1.2 Lithium cobalt oxide	33

CONTENTS (Continued)

	Page
3.1.3 Cobalt ferrite.....	35
3.2 Materials Characterizations.....	36
3.2.1 X ray diffraction.....	36
3.2.2 Scanning electron microscope.....	41
3.2.3 X-ray Absorption Spectroscopy.....	46
3.3 References.....	52
IV DEVELOPMENT OF <i>in situ</i> XAS HEATING CELL.....	54
4.1 Descriptions of <i>in situ</i> cell.....	54
4.2 Heater and temperature controller.....	60
4.3 Temperature testing of <i>in situ</i> heating cell.....	62
4.4 Installation of <i>in situ</i> heating cell at BL5.2 of SLRI.....	66
4.5 References.....	67
V RESULTS AND DISCUSSION.....	68
5.1 <i>In situ</i> XAS study for temperature dependent of FeO.....	68
5.2 Study of phase information in lithium cobalt oxide.....	71
5.2.1 Structural and morphological characterizations.....	71
5.2.2 XANES studies of phase transition.....	75
5.2.3 EXAFS studies of phase transition.....	77
5.3 Study of phase information in cobalt ferrite.....	82

CONTENTS (Continued)

	Page
5.3.1 X ray diffraction results.....	83
5.3.2 XANES results	84
5.3.3 EXAFS results	88
5.4 References	90
VI CONCLUSIONS AND SUGGESTION.....	92
APPENDIX.....	95
CURRICULUM VITAE.....	129



LIST OF TABLES

Table		Page
4.1	The components of the <i>in situ</i> cell.....	56
4.2	The components of the sample holder.....	58
4.3	The components of the quartz glass	59
5.1	The oxidation states for each temperature calculated by Equation (5.1) ...	70
5.2	EXAFS fitting parameters including interatomic distances (R), coordination numbers (N), Debye–Waller factors (σ) and amplitude reduction (S_0^2)	82

LIST OF FIGURES

Figure	Page
2.1	Transmission mode, a schematic of X-ray absorption measurement is shown.9
2.2	Log-log plot of the (semiempirical) X-ray absorption cross section of platinum ($Z=78$) vs. X-ray energy. The K , L_1 , L_2 , L_3 , and M edges are shown; fine structure is not shown10
2.3	Diagram of the electron transition in inner shells..... 11
2.4	Mechanism of the x-ray absorption (a) X-ray absorption (b) Fluorescent X-ray emission and (c) Auger emission 12
2.5	The absorbance Fe K-edge spectra in compound iron oxide..... 14
2.6	The muffin-tin potential consists of non-overlapping spherical regions 16
2.7	a) Single scattering (left), double scattering from different atoms (middle), and double scattering from the same atom (right). (b) Graphical representation of the T-operator..... 19
2.8	Interference of outgoing and backscattered photoelectron wave responsible for XAFS oscillation. $E = \hbar\omega$ is the incoming photon energy.. 20
2.9	Principle of a rechargeable lithium-ion battery... 24
2.10	Inverse cubic spinel structure..... 26
3.1	FeO pellet sample..... 33
3.2	Schematic representation of X-ray diffraction from parallel planes. 37

LIST OF FIGURES (Continued)

Figure	Page
3.3	Schematic drawing of XRD measurement setup..... 38
3.4	X-ray diffraction experiment schematic drawing..... 40
3.5	Schematic representation of X-ray diffractometer Rigaku SmartLab. 40
3.6	Principles schematic illustration of SEM 42
3.7	Schematic diagram of signals in SEM..... 42
3.8	Schematic diagram of an EDS..... 45
3.9	Transmission mode, fluorescence mode, and electron yield are the three modalities of XAS measurement 46
3.10	Schematic illustration of the experimental setup of transmission-mode X-ray absorption spectroscopy 47
3.11	Transmission-mode X-ray absorption spectroscopy experimental setup diagram..... 47
3.12	The excited state (a) x-ray fluorescence and (b) the Auger effect..... 49
3.13	Detail of an atoms.inp input file to generate “feff.inp” for FEFF Calculation..... 50
3.14	Detail of a “feff.inp” input file of LiCoO ₂ with Co as center atom for FEFF Calculation 51
4.1	Schematic drawing of the <i>in situ</i> cell..... 56
4.2	Schematic drawing of the sample holder..... 57
4.3	Schematic of a quartz tube system fixes samples that supply flow gas..... 59

LIST OF FIGURES (Continued)

Figure	Page
4.4 Nichrome resistance heating wire and ceramics insulator.....	61
4.5 Temperature controller and Cooling systems.....	61
4.6 The thermocouples were placed at important positions of the <i>in situ</i> cell....	63
4.7 Schematic diagram showing temperature cycle of the <i>in situ</i> cell.....	63
4.8 Set up for testing the <i>in situ</i> cell with cooling equipment installed.....	64
4.9 Temperature studies diagram for various parts of the heating cell.....	65
4.10 (a) The temperature at different positions of the heating cell (b) sample and control.....	65
4.11 Photo of the <i>in situ</i> heating cell installed at the XAS station at BL5.2 beamline at SLRI.....	67
5.1 Normalized X-ray absorption Fe K-edge spectra of FeO pellet.....	69
5.2 The oxidation number of the Fe K-edge has changed as a result of the calculation.....	71
5.3 XRD patterns of LiCoO ₂ powders with various calcination temperatures...73	73
5.4 SEM images of LiCoO ₂ samples calcined at various calcination temperature: (a) RT, (b) 300 °C, (c) 400 °C, (d) 500 °C, (e) 600 °C and (f) 700 °C	74
5.5 <i>In situ</i> XAS in-house heating cells for transmission mode and Schematic diagram of <i>in situ</i> XAS measurement.....	75
5.6 <i>In situ</i> XANES spectra of Co K edge of LiCoO ₂ samples and standard samples.....	76

LIST OF FIGURES (Continued)

Figure	Page
5.7 Fourier transform at in situ EXAFS spectra at Co K-edge EXAFS (weighted by k^2) from experiment (black line) and fitting (red circle) of LiCoO ₂ at different temperature. Model fits to the experimental filtered EXAFS in the k-space are also shown (insets). Experimental filtered EXAFS in the k-space is also shown (insets).	78
5.8 The local neighboring Co–O (a) and Co–Co (b) distances in LiCoO ₂ structure as a function of temperature.	81
5.9 XRD patterns of CoFe ₂ O ₄ powders with various calcination temperatures.	84
5.10 Schematic diagrams for measure <i>in situ</i> XAS, during the annealing treatment in H ₂	85
5.11 <i>In situ</i> XANES spectra of Fe K-edge (a) and Co K-edge (b).....	87
5.12 Fourier transforms of $k^2\chi(k)$ at probing (a) Fe atom and (b) Co atom	89

LIST OF ABBREVIATIONS

°C	degree Celsius
BL5.2	Beamline 5.2
EXAFS	Extended X-ray Absorption Fine Structure
E_0	Absorption edge
E_B	binding energy
eV	electron-volt
K	Kelvin
h	Plank's constant
I_e	electron current
I_p	photon current
S	spin
SLRI	Synchrotron Light Research Institute
XANES	X-ray Absorption Near Edge Structure
XAS	X-ray Absorption Spectroscopy
SEM	Scanning Electron Microstructure
XRD	X-ray Diffraction
λ	wave length
λ_i	photoelectron mean free path
σ^2	Debye-Waller factor
S_0^2	scale factor

CHAPTER I

INTRODUCTION

Over more than 40 years after the introduction of X-ray absorption fine structure (XAFS) spectroscopy (Stumm von Bordwehr, 1989) as a new advanced characterization technique for material research, X-ray absorption spectroscopy (XAS) has become an essential tool to gather spectroscopic information about atomic energy level structure. XAS has also played an important role in the discovery and systematization of rare-earth elements (Rohler, 1987). The discovery of synchrotron radiation in 1952, and later the availability of broadly tunable synchrotron-based X-ray sources have revitalized this technique since the 1970s. The correct interpretation of the oscillatory structure in the X-ray absorption cross-section above the absorption edge has transformed XAS from a spectroscopic tool to a structural technique (Sayers et al., 1971). Extended X-ray absorption fine structure (EXAFS) yields information about the interatomic distances, near neighbor coordination numbers, and lattice dynamics. An excellent description of the principles and data analysis for EXAFS is given by Teo (Teo, 1986). X-ray absorption near edge structure (XANES) provides information about the valence state, energy bandwidth and bond angles. Today, there are about 60 experimental stations in synchrotron radiation research facilities around the world dedicated to collecting X-ray absorption data from the bulk and surfaces of solids and liquids. A particular strength of the XAS technique is that the penetrating nature of the X-rays makes possible studies of materials under the conditions of their use, including

high temperatures and reactive atmospheres. These same measurements are possible in X-ray diffraction (XRD) but simpler in XAS since, in contrast to XRD, the XAS sample and detectors are stationary (George et al., 1998). In this thesis, advanced principles of XAS are described to explain the information content of essentially two different aspects of the absorption process leading to EXAFS and XANES. The excitation source and sample limitations for XAS measurements are also discussed.

Designing, synthesizing, and manufacturing novel materials with optimum functions necessitates a thorough understanding of the microstructure in the materials. XAS is a useful tool for determining local structure and electrical properties in crystalline compounds, amorphous materials, glasses and liquids (Koningsberger & Prins, 1987). In many cases, structural data can be collected *ex situ*, that is under well-known temperature and atmospheric conditions. For full knowledge of temperature-dependent structures in phase-change materials, *in situ* high-temperature XAS measurements are essential. The high-temperature XAS measurements are essential for understanding temperature-dependent structures in phase-change materials. This technique can also be used to track the growth of nanocrystals and redox reaction dynamics caused by temperature variations (Chen et al., 2008; Kong et al., 2012; Nashner et al., 1998), as well as to reveal the relationship between the structure of a catalyst and its reactivity (Frenkel et al., 2012; Newton et al., 2007; Yamamoto et al., 2007). The *in situ* technique is important for studying and observing materials in real-time depending on temperature changes. This method can be used to track the evolution of local structures in crystalline materials when temperature changes cause phase transitions. For a characterization of materials undergoing unquenchable phase transitions or for following the kinetics of a phase change or reaction, measurements

under *in situ* conditions at elevated temperatures are essential. Moreover, geologically as well as technologically significant transitions from the solid to the liquid state that cannot be studied by the conventional XRD techniques can be studied continuously by XAS, provided a suitable *in situ* high-temperature cell (HTC) is available (Friedrich et al., 1992). Several design techniques for adaptable XAS cells have been published (Bare et al., 2006; Farges et al., 1995; Girardon et al., 2005; Guilera et al., 2009; Huwe & Froba, 2004; Longo et al., 2005; Huwe & Froba, 2004; Longo et al., 2005). Farges et al. (1995), for example, designed a XAS high-temperature cell for the investigation of metal oxide phase transitions using the Mysen–Frantz heating-wire method.

The purpose of this thesis is to develop standardized equipment by investigating and developing *in situ* X-ray absorption spectroscopy techniques for temperature-dependent structural characterization.

This study aims to investigate the temperature depend on local structure of Co and Fe atoms atom in CoFe_2O_4 nanocrystals using the long energy region of *in situ* X-ray absorption spectroscopy (XAS), which called Extended X-ray Absorption fine structure (EXAFS). EXAFS will also be employed to examine the formation of the phase transition in LiCoO_2 and CoFe_2O_4 . Athena and Artemis program will be employed for data analysis and fitting to compare with the experimental results obtained from XAS beamline 5.2 at SLRI, Nakhon Ratchasima Thailand.

Furthermore, the reduction of the oxidation state in the CoFe_2O_4 nanocrystals using the H_2 gas flowed on the heating cell *in situ* XAS will be investigated by the low energy region of X-ray absorption spectroscopy (XAS), which called X-ray Absorption

Near Edge structure (XANES). The FEFF 8.2 algorithm will be used to model the XANES spectra of CoFe_2O_4 .

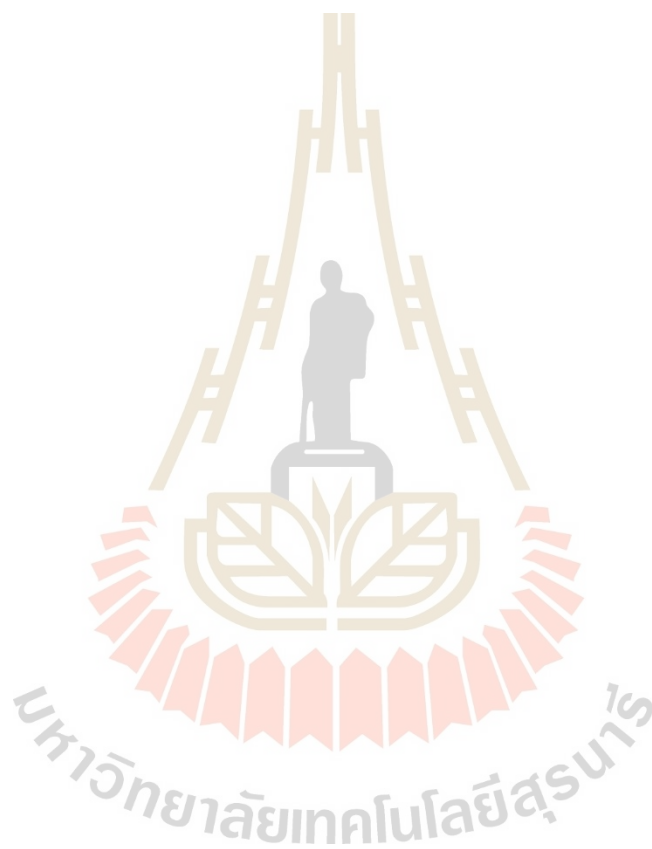
References

- Bare, S. R., Mickelson, G. E., Modica, F. S., Ringwelski, A. Z., & Yang, N. (2006). Simple flow through reaction cells for in situ transmission and fluorescence x-ray-absorption spectroscopy of heterogeneous catalysts. **Review of scientific instruments**, 77(2), 023105.
- Chen, X., Cai, Q., Wang, W., Mo, G., Jiang, L. S., Zhang, K. H., Chen, Z. J., Wu, Z. Y. and Wu, Z. H. (2008). Iron-oxide-supported nanocarbon in lithium-ion batteries, medical, catalytic, and environmental applications. **Chemistry of Materials**. 20, 2757–2762.
- Farges, F., Itié, J. P., Fiquet, G., & Andrault, D. (1995). A new device for XAFS data collection up to 2000 K (or 3700 K under vacuum). Nuclear Instruments and Methods in Physics Research Section B: **Beam Interactions with Materials and Atoms**, 101(4), 493-498.
- Frenkel, A. I., Rodriguez, J. A., & Chen, J. G. (2012). Synchrotron techniques for in situ catalytic studies: capabilities, challenges, and opportunities. **Acs Catalysis**, 2(11), 2269-2280.
- George, M., Simon, R., Deborah, P., Hyung, W. and Daniel, A. F. (1998). An *in situ* X-ray absorption spectroscopic cell for high temperature gas- flow measurements. **Review of scientific instruments**. 69: 2618.
- Girardon, J. S., Khodakov, A. Y., Capron, M., Cristol, S., Dujardin, C., Dhainaut, F., ... & Payen, E. (2005). A new experimental cell for in situ and operando X-ray

- absorption measurements in heterogeneous catalysis. **Journal of synchrotron radiation**, 12(5), 680-684.
- Giri, A. K., Kirkpatrick, E. M., Moongkhamklang, P., Majetich, S. A. and Harris, V. G. (2002). Photomagnetism and structure in cobalt ferrite nanoparticles. **Applied physics letters**. 80: 2341.
- Guilera, G., Gorges, B., Pascarelli, S., Vitoux, H., Newton, M. A., Prestipino, C., ... & Hara, N. (2009). Novel high-temperature reactors for in situ studies of three-way catalysts using turbo-XAS. **Journal of synchrotron radiation**, 16(5), 628-634.
- Huwe, H., & Fröba, M. (2004). A new in situ cell for XAFS investigations. **Journal of synchrotron radiation**, 11(4), 363-365.
- Kong, Q., Baudalet, F., Han, J. et al. Microsecond time-resolved energy-dispersive EXAFS measurement and its application to film the thermolysis of $(\text{NH}_4)_2$. **Scientific Reports**, 1018 (2012).
- Koningsberger, D. C. and Prins, R. (1988). **X-ray Absorption: Principles, Applications, Techniques of EXAFS, SEXAFS, and XANES**. John Wiley and Sons Inc.
- Longo, A., Balerna, A., d'Acapito, F., D'Anca, F., Giannici, F., Liotta, L. F., ... & Martorana, A. (2005). A new cell for the study of in situ chemical reactions using X-ray absorption spectroscopy. **Journal of synchrotron radiation**, 12(4), 499-505.
- Nashner, M. S., Frenkel, A. I., Somerville, D., Hills, C. W., Shapley, J. R., & Nuzzo, R. G. (1998). Core shell inversion during nucleation and growth of bimetallic

- Pt/Ru nanoparticles. **Journal of the American Chemical Society**, 120(32), 8093-8101.
- Newton, M. A., Belver-Coldeira, C., Martínez-Arias, A., & Fernández-García, M. (2007). Dynamic in situ observation of rapid size and shape change of supported Pd nanoparticles during CO/NO cycling. **Nature materials**, 6(7), 528-532.
- Piroux, L., George, J. M., Despres, J. F., Leroy, C., Ferain, E., Legras, R. and Fert, A. (1994). Giant magnetoresistance in magnetic multilayered nanowires. **Applied Physics Letters**. 65: 2484.
- Rohler, J. (1987). X-ray absorption and emission spectra, p. 453-545. In K. A. Gschneider, J., L. Eyring, and S. Hufner (ed.) **Handbook on the Chemistry and Physics of Rare-Earths**. Vol.10.
- Shanthakumar, P. (2008). X-ray study of two complex oxides, each having octahedral oxygen coordination of transition metals. **Doctoral Dissertations**. AAI3314624.
- Stumm von Bordwehr, R. (1989). A History of X-ray absorption fine structure. **Annales de Physique**. 14: 377.
- Teo, B. K. (1986). EXAFS: Basic principles and data analysis. **Springer Verlag**.
- Yamamoto, T., Suzuki, A., Nagai, Y., Tanabe, T., Dong, F., Inada, Y., ... & Iwasawa, Y. (2007). Origin and dynamics of oxygen storage/release in a Pt/ordered CeO₂-ZrO₂ catalyst studied by time-resolved XAFS analysis. **Angewandte Chemie International Edition**, 46(48), 9253-9256.

Zi, Z., Sun, Y., Zhu, X., Yang, Z., Dai, J. and Song, W. (2009). Synthesis and magnetic properties of CoFe_2O_4 ferrite nanoparticles. **Journal of Magnetism and Magnetic Materials**. 321: 1251.



CHAPTER II

REVIEW OF LITERATURES

This chapter consists of two parts. The first section describes the XAS theory, covering XANES (X-ray absorption near edge structure) and EXAFS (extended X-ray absorption fine structure) measurement techniques. The second part provides the background information of advanced materials used for commissioning test of the in situ heating cell development in this thesis work.

2.1 X-ray Absorption Spectroscopy (XAS)

Absorption of X-rays spectroscopy is a useful technique for determining an element's local structure, formal oxidation state, and neighboring atoms, as well as investigating the electronic structure of materials. Normally, the XAS experiment is carried out at a synchrotron radiation facility, where the energy of X-ray photons may be changed and adjusted (Shanthakumar, 2008). Furthermore, the synchrotron radiation facility contains light sources with a high intensity.

The Lambert-beer law explains the absorption equation, which states that the intensity of the beam after passing through the sample drops exponentially with the strength of the entering X-ray beam, as

$$I = I_0 e^{-\mu x} \quad (2.1)$$

where I_0 is the entering X-ray beam's intensity, I is the beam's intensity after passing through the sample, x is the sample's thickness, μ is the absorption coefficient and the absorption was determined by μx

$$\ln \left(\frac{I_0}{I} \right) = \mu x \quad (2.2)$$

The absorption cross-section σ_a and the linear absorption coefficient are related by

$$\mu = \sigma_a \rho_a = \frac{\sigma_a \rho_m N_A}{A} \quad (2.3)$$

where A , ρ_a , ρ_m and N_A are the atomic mass number, the atomic density, the mass density and Avogadro's number, respectively.

The photon energy has a strong influence on the absorption cross section. Figure 2.2 shows the element platinum. The double-logarithmic figure shows that the absorption cross section is roughly proportional to $1/E^3$ below and above discontinuities.

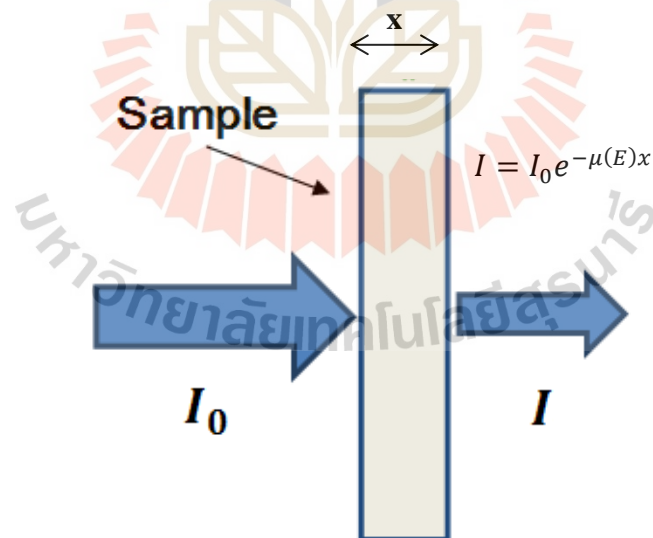


Figure 2.1 Transmission mode, a schematic of X-ray absorption measurement is shown.

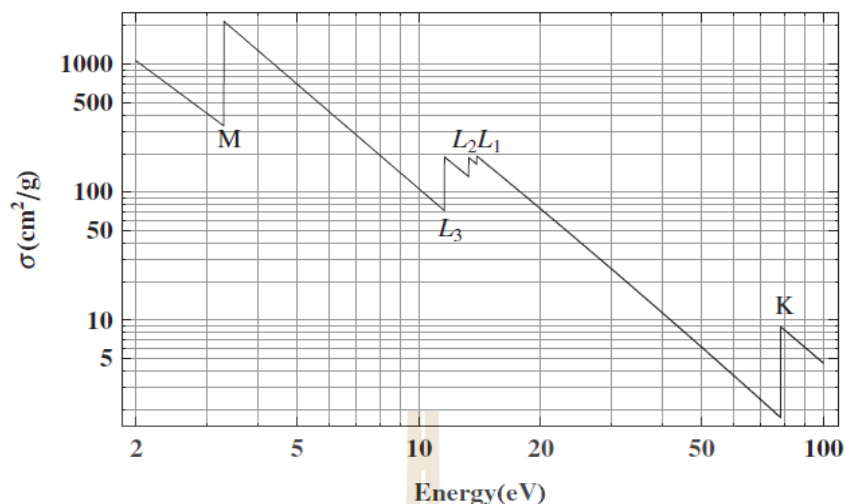


Figure 2.2 Log-log plot of the (semiempirical) X-ray absorption cross section of platinum ($Z=78$) vs. X-ray energy. The K , L_1 , L_2 , L_3 , and M edges are shown; fine structure is not shown. (Bunker, 2010).

The latter, which well known as the absorption edges, occur at characteristic energies for which the X-ray has enough energy to expel an electron from an atomic core level giving rise to a sudden increase of the absorption cross section.

In case the electrons transition is followed by the selection rules. The Selection Rules governing transitions between electronic energy levels of transition metal complexes are

1. $\Delta S = 0$; The Spin Rule, the electron's spin must be unchanged from core shell state to excited state.

2. $\Delta l = \pm 1$; The Orbital Rule, the difference of electron's orbital angular momentum must be equal -1 or 1 only.

The total angular momentum was defined as $J = l + S$ or have value $|l - s| \geq J \geq l + s$, where $l = 0, 1, 2, \dots, n - 1$ and $S = -\frac{1}{2}, \frac{1}{2}$. Therefore, the spin rule can be considered by $\Delta J = \pm 1$. In addition, the new symbol for electron each shell were

defined for the electron transition. Figure 2.3 shows the electron transition in inner shell.

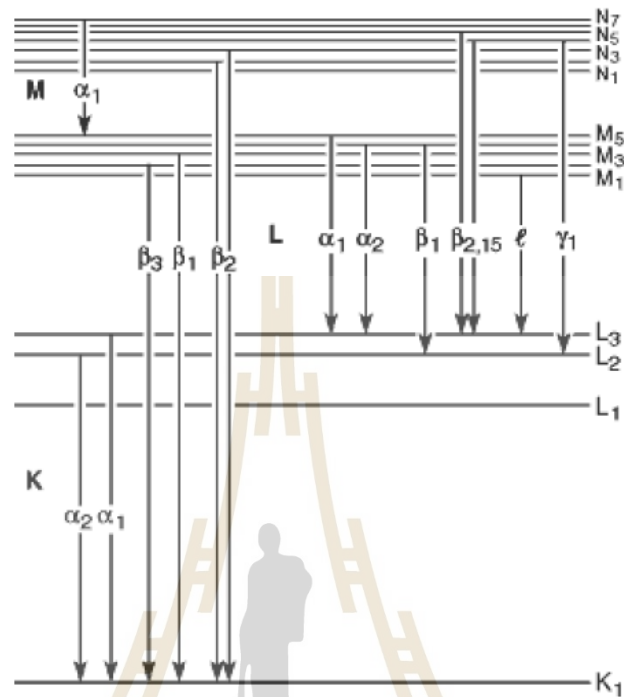


Figure 2.3 Diagram of the electron transition in inner shells. (Thompson et al., 2001).

When the X-ray energy is incident through the binding energy of a core shell, there exhibits a sudden increase in absorption cross-section. This spectrum is called absorption edge, with each edge representing a different core-electron binding energy. The name of edges is identified by the principle quantum number: *K* for $n=1$, *L* for $n=2$, *M* for $n=3$, etc. In the X-ray absorption process, a photon energy was absorbed by atom, affect to electron in inner shells: *K*, *L* or *M* shell which is transition to unoccupied valance band above the Fermi level. However, when electron is excited, energy state will not be stable. Therefore, electron in next state will be transition to replace excited electron and fluorescence emission occurs, shown in Figure 2.4. Although, core energy

state is stabilized but the next state will not be stable. Therefore, another electron in next state will transit to conduction band and it is called Auger electron.

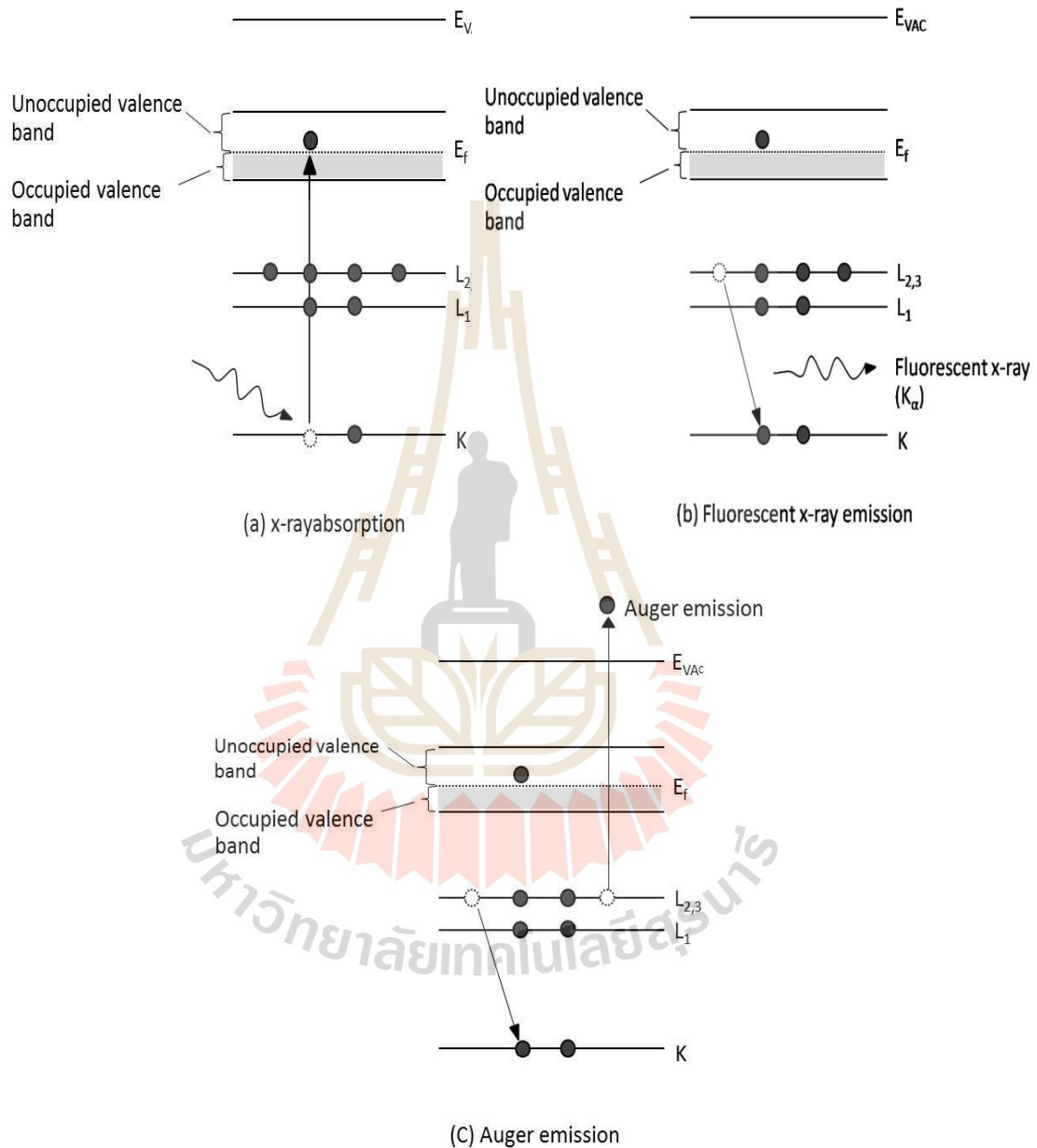


Figure 2.4 Mechanism of the X-ray absorption (a) X-ray absorption (b) Fluorescent X-ray emission and (c) Auger emission. (Adapt from Klysubun, 2006).

The X-ray absorption spectroscopy (XAS), sometime called X-ray absorption fine structure (XAFS), is an absorption spectroscopy technique that refers to a modulation of the absorption coefficient as a function of the incident photon, typically by a few presents, around and above the absorption edge. This fine structure is unique signature of a given material due to it depends on the detailed local structure and electronic structure of the material. For example, Fe *K*-edge refers to transition that excited electron from 1s to 3d orbital but according to the selection rule that is forbidden. However, in the case of compound FeO, the effect of Fe-O bonding affects d-orbital spitting as t_{2g} and e_g , after then occur the mixing d-p orbital from ligand field theory. Therefore, a forbidden transition is partially allowed due to mixing of ligand p-character. While the first line on the main edge is due to the allowed 1s to 4p bound-state transition. The post edge relates to unoccupied state in conduction band and full multiple scattering of spherical wave electron with neighbor atom. XAS is further divided into two types: X-ray Absorption Near Edge Structure (XANES), which terminates approximately 80-100 eV above the edge, and Extended X-ray Absorption

Fine Structure (EXAFS), which begins around 50 eV above the edge., as shown in Figure .

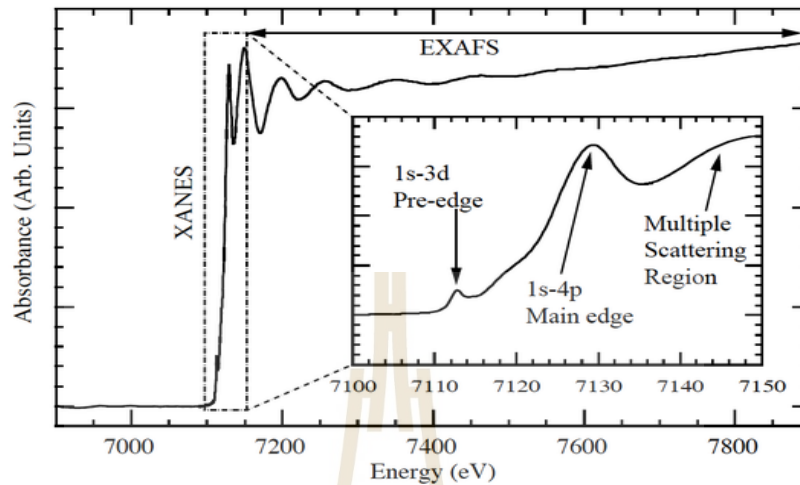


Figure 2.5 The absorbance Fe K-edge spectra in compound iron oxide. (Larsen et al., 2014).

2.1.1 X-ray Absorption Near Edge Structure (XANES)

The XANES area (including the pre-edge region) gives information on the absorbing atom's local geometry. The edge position also contains information about the charge (oxidation state) on the absorber. According to the overlapping contributions of many electronic and structure effects and the approximations necessary for its theoretical description, the XANES is frequently only qualitatively interpretable.

The total absorption cross-section can be calculated by using the Fermi's Golden rule of one electron approximation (Gaussian unit) (Koningsberger and Prins, 1988; Kodre, 2002; Stern et al., 1983; Als-Nielsen and McMorow, 2001; Newville, 2004; Ravel, 1997; Shanthakumar, 2008),

$$\mu(\omega) = \frac{4c\pi^2 e^2}{\omega} \sum_{i,f} \left| \langle f | \vec{r} \cdot \hat{\epsilon} e^{i\vec{k} \cdot \vec{r}} | i \rangle \right|^2 \delta(E_i - E_f + \hbar\omega) \quad (2.4)$$

where $|i\rangle$, $|f\rangle$, E_i and E_f denote the initial and final states and their energies; k is wave vector, $\hat{\epsilon}$ is unit polarization, ω is frequency of photon energy, c is light velocity, e is electron charge and $\delta(E_i)$ is the Dirac delta function. Generally, this equation can be written in form the Dipole operator (D) as

$$\mu(\omega) = \frac{4c\pi^2 e^2}{\omega} \sum_{i,f} |\langle f | \bar{D} | i \rangle|^2 \delta(E_i - E_f + \hbar\omega) \quad (2.5)$$

which can easily understand for electron transition from $|i\rangle$, to next $|f\rangle$ state corresponding to the photon energy incident in the Dirac delta function and amplitude relate dipole transition in inner atom. However, when electron was excited by photon energy greater than binding energy, the electron will be transit to unoccupied valance band after then the photon energy is higher which carry out from inner atom and exhibit the propagation of spherical electron wave.

In this case we calculate the spherical electron wave scattering from the muffin-tin approximation. We discuss scattering from muffin-tin potential which is several atoms or ions, each of which makes a non-zero contribution only within a spherically non-overlapping scattering region of finite radius.

$$V = \sum_i v^i \quad (2.6)$$

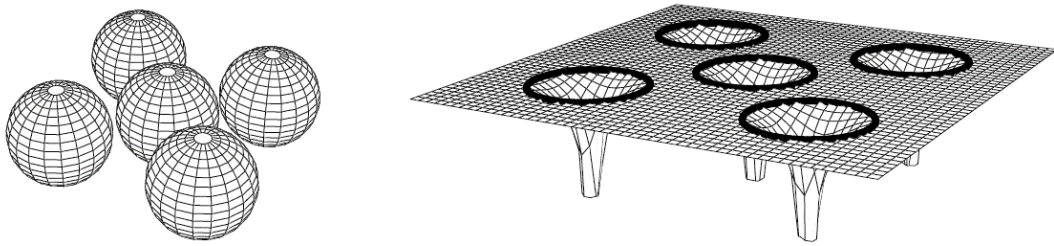


Figure 2.6 The muffin-tin potential consists of non-overlapping spherical regions. (Kodre, 2002).

Figure 2.6, shows the muffin-tin potential, which outside the spherical regions or interstitial region, the potential is set to zero. The scattering parameters, consisting of the scattering amplitude and phase shifts, are determined separately for each scatterer and are therefore pure atomic quantities. Propagation of spherical electron wave in such muffin-tin potential V is described by the Hamiltonian

$$H = H_0 + V \quad (2.7)$$

where H_0 is the kinetic-energy operator. According to Schrodinger's equation is

$$H|\varphi\rangle = E|\varphi\rangle \quad (2.8)$$

$$(E - H_0)|\varphi\rangle = V|\varphi\rangle \quad (2.9)$$

However, we cannot solve to exact solution. Therefore, we can consider to separated terms. The term of $(E - H_0)|\varphi\rangle$ is free-electron wave function and if $\langle \vec{r} | \phi \rangle$ is the solution of the “homogeneous” part of free-electron wave function

$$(E - H_0)\langle \vec{r} | \phi \rangle = 0 \quad (2.10)$$

And the free-electron Green's function G_0 is defined with relation

$$(E - H_0)G_0(\vec{r}, \vec{r}'; E) \equiv (\nabla^2 + k^2)G_0(\vec{r}, \vec{r}'; E) = \delta(\vec{r} - \vec{r}') \quad (2.11)$$

Therefore, the general solution of Eq. (2.10) can be written as a sum of the solution of the “homogeneous” part and the Green’s function for the muffin-tin potential part

$$\langle \vec{r} | \varphi \rangle = \langle \vec{r} | \emptyset \rangle + \int d^3 r' G_0(\vec{r}, \vec{r}'; E) \langle \vec{r}' | V \varphi \rangle \quad (2.12)$$

It is easily understood, if the spherical electron wave is only weakly scattered by the potential V , the solution $\langle \vec{r} | \varphi \rangle$ is close to the free-electron solution $\langle \vec{r} | \emptyset \rangle$. Generally, the Green’s function can be written in form

$$G_0^\pm(\vec{r}, \vec{r}'; E) = \langle \vec{r} | G_0^\pm | \vec{r}' \rangle = -\frac{1}{4\pi} \frac{e^{\pm ik|\vec{r}-\vec{r}'|}}{|\vec{r}-\vec{r}'|} = \left\langle \vec{r} \left| \frac{1}{E - H_0 \pm i\eta} \right| \vec{r}' \right\rangle \quad (2.13)$$

Because of its singularity, an imaginary term is modified in the operator $\frac{1}{E-H_0}$ by $\pm i\eta$, where η is infinitesimally small for identify direction of spherical wave electron, G_0^+ and G_0^- describe how outing and coming spherical waves propagate in free space, respectively. Therefore, the formal solution of the operator Eq (2.12). is given by the Lippman-Schwinger equation

$$\langle \vec{r} | \varphi \rangle = \langle \vec{r} | \emptyset \rangle + \frac{1}{E - H_0 \pm i\eta} V | \varphi \rangle \quad (2.14)$$

To solve Eq. (2.14), one needs to define transition operator (T) are

$$V | \varphi \rangle = T | \varphi \rangle \quad (2.15)$$

If we define the propagation G of this system as

$$G(E) = \frac{1}{E - H_0 - V + i\eta} = ([G_0]^{-1} - V)^{-1} = G_0(1 - VG_0)^{-1} \quad (2.16)$$

According to the Taylor series expression

$$G(E) = G_0 + G_0VG_0 + G_0VG_0VG_0 + \dots = G_0 + G_0VG \quad (2.17)$$

The following important relationships from Eq. (2.15),

$$G_0T = GV;$$

$$T = G_0^{-1}GV = V + VG_0V + VG_0VG_0V + \dots = V + VG_0T \quad (2.18)$$

and then

$$G = G_0 + G_0TG_0; T = V + VGV \quad (2.19)$$

according to the muffin-tin potentials from Eq. (2.6), we can write the transition operators of individual atoms as

$$t^i = v^i + t^i v^i G_0 \quad (2.20)$$

However, the operator T and t^i is not obvious in the physical meaning, but we are able to explain in the weak-scattering expansions by substituting Eq. (2.20) into (2.18) and (2.19) respectively, we obtain

$$\begin{aligned} G &= G_0 + \sum_i G_0 v^i G_0 + \sum_{i, i_1} G_0 v^i G_0 v^{i_1} G_0 + \dots \\ &= G_0 + \sum_i G_0 t^i G_0 + \sum_i \sum_{i_1 \neq i} G_0 t^{i_1} G_0 t^i G_0 + \dots \end{aligned} \quad (2.21)$$

$$T = \sum_i t^i + \sum_i \sum_{i_1 \neq i} t^{i_1} G_0 t^i + \sum_i \sum_{i_1 \neq i} \sum_{i_2 \neq i} t^{i_2} G_0 t^{i_1} G_0 t^i + \dots \quad (2.22)$$

$$t^i = v^i + v^i G_0 v^i + v^i G_0 v^i + v^i G_0 v^i G_0 v^i + \dots \quad (2.23)$$

Their series equations are called Dyson's expansion and Eq. (2.22) can explain the order of scattering process of the spherical electron wave. The first term is an unscattered wave propagation. The second term is single scattering by free propagation

G_0 to the i th atom where the wave is scattered once with potential v^i and then heads forward again as shown in Figure 2.7 (a)-left. Similarly, the third term “scatter” describes the incident wave two times as shown in Figure 2.7 (a)-middle and right.

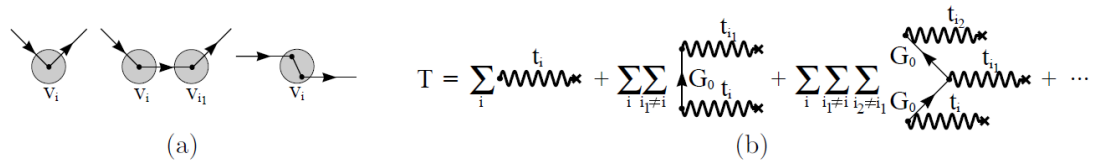


Figure 2.7 (a) Single scattering (left), double scattering from different atoms (middle), and double scattering from the same atom (right). (b) Graphical representation of the T-operator. (Kodre, 2002).

2.1.2 Extended X-ray Absorption Fine Structure (EXAFS)

The EXAFS refers to the oscillating part of the X-ray absorption spectrum starting at approximately 80 eV above the absorption edge and extending up to about 1,000 eV. Above the absorption edge, the energy of X-ray photon is used to excite an electron into the continuum and any remaining energy is given to photoelectron in the form of kinetic energy. The photoelectron can be described as spherical waves propagating from the absorber atoms. If the other atoms are located in the vicinity of the absorber atoms, the photoelectron is scattered by the neighboring atoms and then return to the absorber atoms contribute to the EXAFS signal (Groot et al., 1994; Hench and West, 1990). The incoming and the scattered waves may interfere, as indicated in Figure 2.8. Each atom at the same radial distance from the absorber contributes to the same component of the EXAFS signal. This group of the atoms is called a shell. The distance between the absorber and the backscattering atom affects the phase of the EXAFS signal, which changes with the wavelength of the photoelectron. The type of

atom that backscatters determine the change in backscattering strength as a function of photoelectron energy. As a result, EXAFS provides data on the atomic surrounds of the central atom. In the EXAFS measurement, above a certain absorption edge, the oscillatory portion of the X-ray absorption spectrum is studied. Therefore, an experimental EXAFS function can be defined by

$$\chi(E) = [\mu(E) - \mu_0(E)]/\Delta\mu_0(E) \quad (2.24)$$

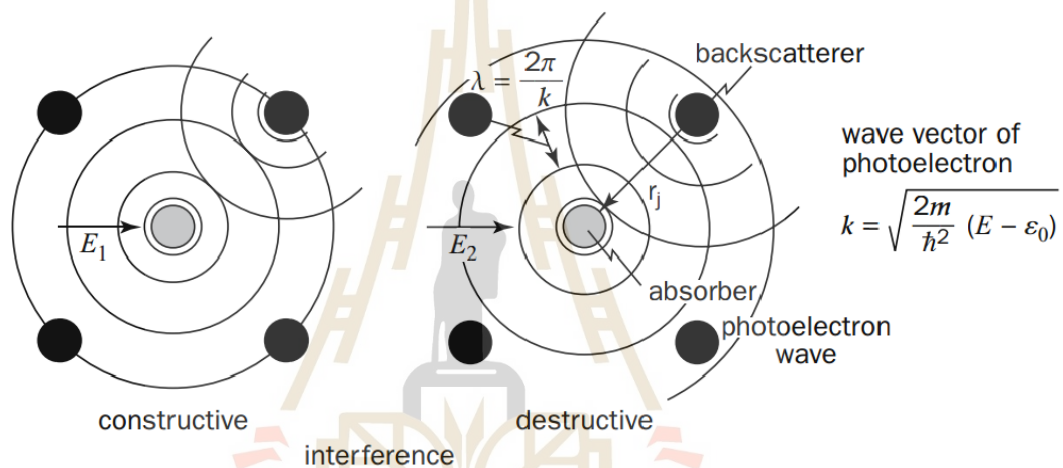


Figure 2.8 Interference of outgoing and backscattered photoelectron wave responsible for XAFS oscillation. $E = \hbar\omega$ is the incoming photon energy. (Hippert et al., 2006).

where μ_0 is the background absorption coefficient, $\Delta\mu_0(E)$ is the absorption edge jump, and k is the photoelectron wave number, given by $k = \sqrt{2m_e(E - E_0)}/\hbar$ with m_e is the electron mass and E_0 is the edge energy. After that, $\chi(k)$ is obtained from the measured absorption coefficient $\mu(E)$. Also, the E_0 is the energy at the first maximum of the derivative of $\mu(E)$ at the Ti K-edge (G. Bunker, 2010). According to Fermi-Golden rule Eq. (2.4), the final state will be affected by the neighboring atom because the photo-electron will be able to see it. If we separate $|f\rangle$

into two state, one that is the “bare atom” portion ($|f_0\rangle$), and one that is the effect of the neighboring atom ($|\Delta f\rangle$) as

$$|f\rangle = |f_0\rangle + |\Delta f\rangle \quad (2.25)$$

Therefore

$$\mu(E) \propto |i\langle\hat{\epsilon}\rangle f_0|^2 [1 + \langle i\langle\hat{\epsilon}\rangle\Delta f \rangle \frac{\langle f|\langle\hat{\epsilon}i\rangle\rangle^*}{|i\langle\hat{\epsilon}\rangle\Delta f|^2} + C.C] \quad (2.26)$$

where C.C. means complex conjugate. Comparison Eq. (2.25) and (2.26), we can now assign $\mu(E_0) = |i\langle\hat{\epsilon}\rangle f_0|^2$ as the “bare atom absorption”, which depends on the absorbing atom only. Therefore, the signal of EXAFS will be proportion as

$$\chi(E) \propto \langle i\langle\hat{\epsilon}\rangle\Delta f \rangle \quad (2.27)$$

We can consider (at least roughly) an integral equation easily (at least roughly). The interaction term H is probably the most complicate part, which represents the process of changing between two energy, momentum states. In quantum radiation theory, the interaction term needed is the $p \cdot \mathbf{A}$ term, where \mathbf{A} is the quantized vector potential (the $\mathbf{A} \cdot \mathbf{A}$ term, but this does not contribute to absorption). Therefore, it can be reduced to a term that is proportional to $e^{-i\mathbf{k} \cdot \mathbf{r}}$. The initial state is a tightly bound core-level, which we can be approximated by delta function. Finally, the change in final state is the wave-function of the scattered photo-electron, $\varphi_{scatt}(r)$.

$$\chi(E) \propto \int dr \delta(r) e^{i\mathbf{k} \cdot \mathbf{r}} \varphi_{scatt}(r) \quad (2.28)$$

However, $r = 0$

$$\chi(E) \propto \varphi_{scatt}(0) \quad (2.29)$$

The wave-function of the scattered photo-electron can consider from the spherical wave electron move out from absorber atoms and expression as

$$\varphi_{backscatt}(k, r) = (f_i^{eff}(k)e^{ik|R_i-r|}e^{i(\delta_i(k)-\frac{\pi}{2})})(|R_i - r|)^{-1} \quad (2.30)$$

where $f_i^{eff}(k)$ is the scattering amplitude and the term $\delta_i(k) - \frac{\pi}{2}$ is phase shift of photoelectron after scattering from neighbor atoms. Therefore, the total photoelectron wave scattering obtains by

$$\begin{aligned} \varphi_{scatt}(k, r) &= \varphi_0(k, r) \cdot \varphi_{backscatt}(k, r) \\ &= f_i^{eff}(k)e^{2ik|R_i-r|+(\delta_i(k)-\frac{\pi}{2})} \cdot (|R_i - r|)^{-2} \end{aligned} \quad (2.31)$$

The scattering at absorber atom $r = 0$, the real part of Eq. (2.31) is

$$\varphi_{scatt}(k, r) = f_i^{eff}(k)\sin[skR + \delta_i(k)]R^{-2} \quad (2.32)$$

However, we neglect the effect of the thermal and static disorder in the bond distances will give a range of distances that will affect the XAFS is $e^{-2k^2\sigma^2}$, where is the Debye-Waller (DW) factor which is caused by thermal vibration in subject of the heat capacity, is written as

$$\sigma_i^2(T) = \frac{\hbar^2}{2k_B M_R \theta_E} \coth\left(\frac{\theta_E}{2T}\right) \quad (2.33)$$

Where k_B is the Boltzmann constant, is reduce mass of scattering atoms and is the Einstein temperature.

Moreover, we still neglect the effect of the lifetime of excited photoelectron and core hole. Because in order for backscattering wave to interfere with outgoing wave the two must be coherent as

$$e^{\frac{-R_i}{\lambda(k)}} \quad (2.34)$$

However, real systems usually have more than one type of neighboring atom around a particular absorbing atom. This is easily accommodated in the XAFS formalism, as the measured XAFS will simply be a sum of the contributions from each scattering atom type (or coordination shell, as it is often called – the terms coordination sphere and scattering path are also used), In general $\chi(k)$, can be expressed by summation of all path, EXAFS equation is

$$\chi(k) = \sum_f \frac{S_0^2 N_j}{k R_j^2} |f_j^{eff}(k, R_j)| \sin[2kR_j + \varphi_j(k)] e^{-2\sigma_j^2 k^2} e^{-R_j/\lambda(k)} \quad (2.35)$$

where N_j is the degeneracy of path j . Note that Eq. (2.107) includes both single scattering (SS) and multiple scattering (MS) processes. For a SS path, N_j is simply the number of chemically identical atoms situated at a given distance R_j from the central atom. However, $\chi(k)$ can be a Fourier transform (FT) in R-space and expressed by

$$\chi(R) = \frac{\int_0^\infty k^2 \chi(k) w(k) e^{2ikR}}{2\pi} dk \quad (2.36)$$

To process and enhance the EXAFS with the high k region, the plot $k^2\chi(k)$ is considered and windowed using a Hanning window $w(k)$.

2.2 Lithium cobalt oxide

The most viable candidates as a sustainable energy conversion and storage systems are the rechargeable lithium-ion battery (LIB), which was commercialized by Sony in the early 1990s. (Jeong, 2011; Nagura, 1990). The LIB is based on a cathode and an anode, which has the property of reversible insertion and extraction of lithium ions. Transfer of lithium ions is enabled by the addition of an organic liquid electrolyte

and a mechanical separator between the anode (negative electrode) and the cathode (positive electrode). When the lithium ion is inserted and extracted in the cathode and the anode, electrical energy is generated by electrochemical oxidation and reduction as shown in Figure 1.1.

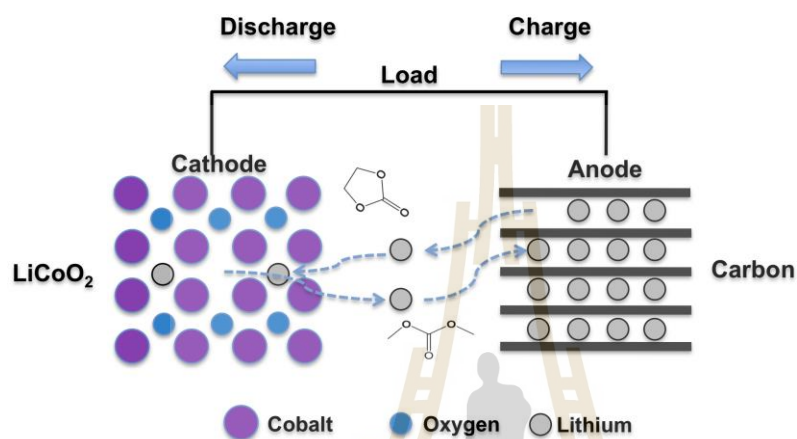


Figure 2.9 Principle of a rechargeable lithium-ion battery. (adapt from Jeong, 2011).

Generally, many researchers prepared LiCoO_2 by solid-state reaction. However, owing to insufficient mixing and the low reactivity of the starting materials, calcination at $850\text{--}900\text{ }^\circ\text{C}$ for several hours is required to successfully synthesize LiCoO_2 . LiCoO_2 exhibits two forms, a hexagonal structure and a cubic structure, regarding the two types of LiCoO_2 as low temperature (LT- LiCoO_2), the cubic form, and high temperature (HT- LiCoO_2), the hexagonal form, lithium cobalt oxide is not appropriate, considering that HT- LiCoO_2 is obtained also at very low temperatures. The hexagonal and cubic structures are based on the same oxide sublattice, and are distinguished by the spatial arrangement of cations (Antolini, 2004). It has a hexagonal structure in which the Li^{+1} and Co^{3+} ions are ordered on the alternate (1 1 1) planes of octahedral sites in a nearly cubic close packed oxygen lattice (Orman, 1984; Dahe'ron, 2008). For these reasons, to study formation of crystallized LiCoO_2 powders with several temperatures, efforts

have been learned to investigate solid state reaction and co-precipitation method. The crystal structure of the complex oxides of the LiCoO_2 was reviewed by Kellerman (Kellermann, 2001). The present work deals on the formation, structure and transport properties of lithium cobalt oxide.

2.3 Cobalt ferrite

Magnetic nanoparticles have attracted much attention in the past decades because of their potential applications in high density magnetic recording, magnetic fluids, data storage, solar cells, sensors, and catalysis. Among the magnetic nanoparticles, cobalt ferrite (CoFe_2O_4) has been widely studied due to high electromagnetic performance (Yin, 2004; El-Sayed, 2004), excellent chemical stability, mechanical hardness, and high cubic magnetocrystalline anisotropy. These properties make it a promising candidate form any applications in commercial electronics such as video, audiotapes, high-density digital recording media (Piroux et al., 1994; Giri, 2002), and magnetic fluids.

The cubic-spinel-structured CoFe_2O_4 ferrite represents a well-known and important class of iron oxide materials. The O^{2-} ions form fcc close packing, and the Co^{2+} and Fe^{3+} occupy either tetrahedral or octahedral interstitial sites. These two antiparallel sublattices, which are coupled by superexchange interactions through the O^{2-} ions, form the ferrimagnetic structure. The ferrite spinel structure is based on a closed-packed oxygen lattice, in which tetrahedral (called A sites) and octahedral (called B sites) interstices are occupied by the cations. Spinels with only divalentions in tetrahedral sites are called normal, while compounds with the divalentions in the octahedral sites are called inverse. In the inverse spinel structure, all the Co^{2+} ions

occupy the octahedral sites of lattice structure, half of the Fe^{3+} ions also occupy the same sites and the rest of the Fe^{3+} ions stay in tetrahedral sites (Goldman, 2006).

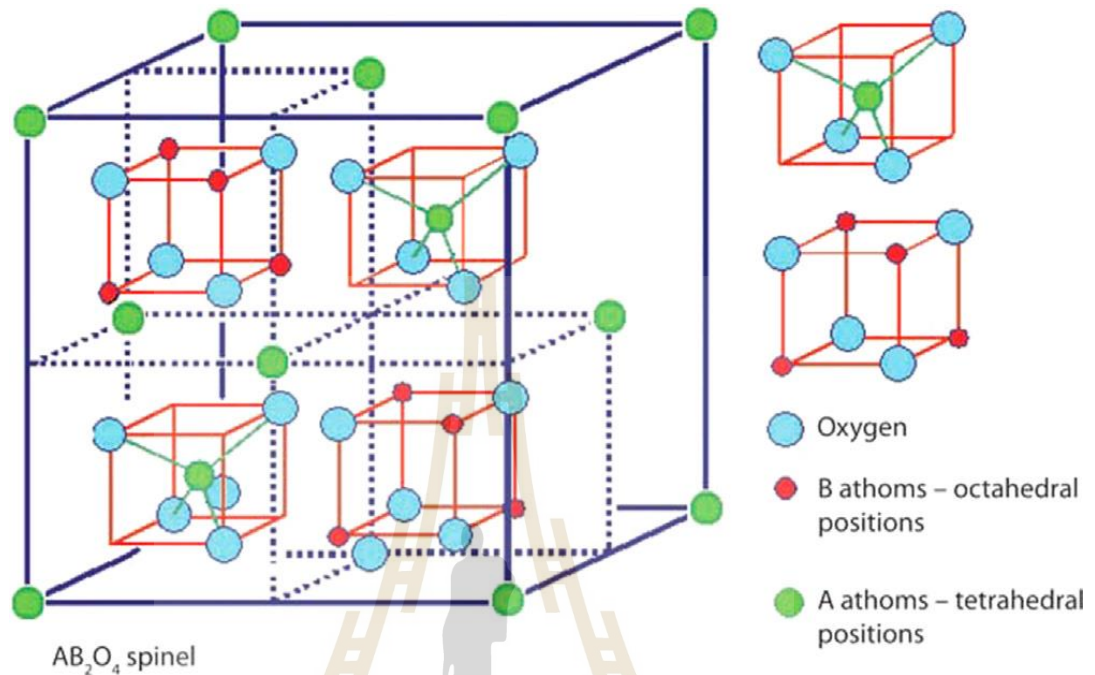


Figure 2.10 Inverse cubic spinel structure. (Houshiar, 2014).

Most of the magnetic properties of CoFe_2O_4 ferrite strongly depend on the size and shape of the nanoparticles, which are closely related to the method of preparation. Several routes have been used to prepare cobalt ferrite, including the sol–gel method (Cheng et al., 1996), microemulsion with oil in water micelles, reverse micelles method, chemical coprecipitation method, combustion reaction method, and forced hydrolysis in a polyol medium. However, most of these methods cannot be economically applied on a large scale because they require expensive and often toxic reagents, complicated synthetic steps, high reaction temperatures, and long reaction times. This not only results in waste of energy but also harms our environment. As is well known, the chemical coprecipitation method is usually used to synthesize magnetic oxides due to its simplicity and good control of grain size. However, in previous reports it was always

observed that there exist some undesirable intermediate phases, which led to poor magnetic properties and irregular shape for the derived CoFe_2O_4 ferrite particles. Single-phase highly monodisperse CoFe_2O_4 ferrite nanoparticles with relatively homogeneous size can be prepared by means of a modified chemical coprecipitation method (Zhenfa, 2009).

Recently, researchers have found that CoFe_2O_4 have been studied as oxygen carriers for the Chemical Loop Reforming (CLR) of ethanol. By using in X-ray absorption spectroscopy followed in real time the chemical and structural changes that take place on the materials as a function of temperature and reactive atmosphere (i.e., ethanol/ water streams). The cations in tetrahedral sites of the spinel structure show a higher reducibility with the respect of octahedral ones, independently from their chemical nature. The reduction of the spinel structure leads to the formation of a wüstite phase and of FeCo metal alloys. Conversely, considering the ratio between reduced phases (wüstite and metal alloy), the chemical nature of the cation plays an important role. However, the mechanism has not yet been clarified and, moreover, the temperature dependent local structure and the activation energy are left an open question. Thus, an investigation of the exact local structure of CoFe_2O_4 has been extensively studies.

2.4 References

- Als-Nielsen, J. and McMorrow, D. (2001). **Elements of Modern X-ray Physics**. John Wiley and Sons.
- Antolini, E. (2004). LiCoO_2 : Formation, structure, lithium and oxygen nonstoichiometry, electrochemical behaviour and transport properties. **Solid State Ionics**. 170: 159.

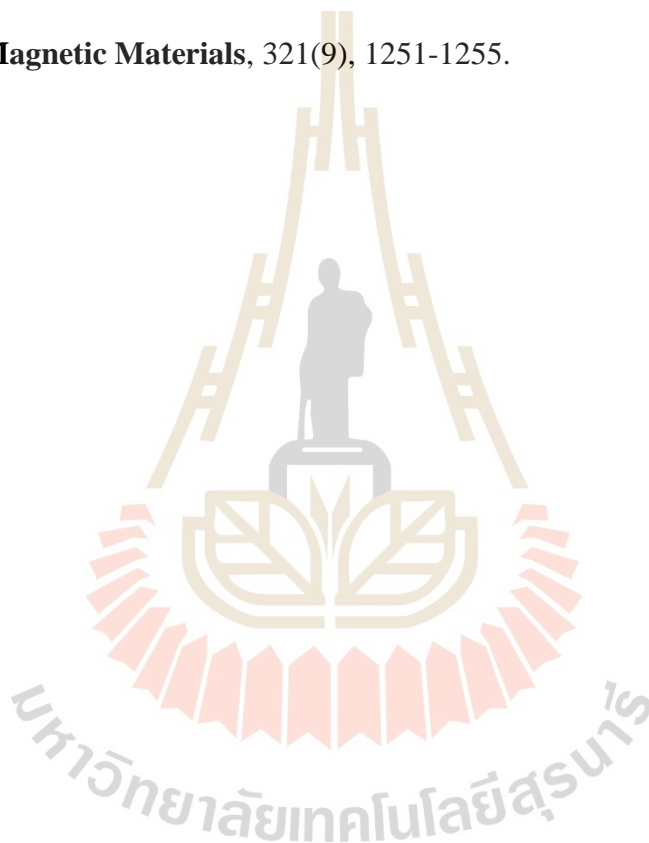
- Bunker, G. (2010). Introduction to XAFS: A practical Guide to X-ray Absorption Fine Structure Spectroscopy. **Cambridge**: Cambridge University press.
- Cheng, F., Peng, Z., Liao, C., Xu, Z., Gao, S., Yan, C. and Wang, J. (1998). Chemical synthesis and magnetic study of nanocrystalline thin films of cobalt spinel ferrites. **Solid State Communications**. 107: 471.
- Dahéron, L., Dedryvere, R., Martinez, H., Ménétrier, M., Denage, C., Delmas, C. and Gonbeau, D. (2007). Electron transfer mechanisms upon lithium deintercalation from LiCoO_2 to CoO_2 investigated by XPS. **Chemistry of Materials**. 20: 583.
- El-Sayed, M. A. (2004). Small is different: shape-, size-, and composition-dependent properties of some colloidal semiconductor nanocrystals. **Accounts of chemical research**. 37: 326.
- Goldman, A. (2006). Modern ferrite technology. **Springer Science & Business Media**.
- Groot, D., F., F. M., Hu, Z. W., Lopez, M. F., Kaindl, G., Guillot, F. and Tronc, M. (1994). Differences between L3 and L2 x-ray absorption spectra of transition metal compounds. **Journal of Chemical Physics**. 101: 6570.
- Hench, L. L. and West, J. K. (1990). **Principles of electronic ceramics**. Wiley.
- Hippert, F., Geissler, E., Hodeau, J. L., Lelièvre-Berna, E. and Regnard, J. R. (2006). **Neutron and X-ray Spectroscopy**. Netherlands: Springer.
- Jeong, G., Kim, Y. U., Kim, H., Kim, Y. J. and Sohn, H. J. (2011). Prospective materials and applications for Li secondary batteries. **Energy & Environmental Science**. 4: 1986.
- Kellermann, D. G. (2001). Magnetic properties of complex oxides LiMO_2 ($M = \text{Sc-Ni}$) with different types of cationic ordering. **Russ. Chemical Reviews**. 70(9): 777.

- Klysubun, W. (2006). X- ray Absorption Spectroscopy Technique. **Nakhon Ratchasima Synchrotron Light Research Institute.**
- Kodre, A. (2002). XANES spectroscopy (online). Available: <http://www.ung.si/~arcon/xas/xanes/xanes-theory.pdf>.
- Koningsberger, D. C. and Prins, R. (1988). **X- ray Absorption: Principles, Applications, Techniques of EXAFS, SEXAFS, and XANES.** John Wiley and Sons Inc.
- Larsen, D. (2014). **XANES** : Application. Available: <http://chemwiki.ucdavis.edu.htm>.
- Nagura, T. and Tazawa, K. (1990). Lithium- Ion Rechargeable Battery. **Progress Batteries Solar Cells.** 9: 20.
- Newville, M. (2004). **Consortium for Advanced Radiation Sources.** Chicago.
- Orman, H. J. and Wiseman, P. J. (1984). Cobalt (III) lithium oxide, CoLiO₂: structure refinement by powder neutron diffraction. **Acta Crystallographica Section C: Crystal Structure Communications.** 40: 12.
- Ravel, B. D. (1997). **Ferroelectric Phase Transition in Oxide Perovskites Studied by XAFS.** Ph.D. Dissertation, University of Washington, Washington.
- Shanthakumar, P. (2008). **X- ray study of two complex oxides, each having octahedral oxygen co-ordination of transition metals.** Ph.D. Dissertation, University of Connecticut. Connecticut.
- Stern, E. A., Heald, S. M. and Koch, E. E. (1983). **Synchrotron Radiation.** North-Holland.
- Thompson, A. C., Attwood, D. T., Gullikson, E. M., Howells, M. R., Jeffrey B. Kortright, Robinson, A. L., Underwood, J. H., Kim, K.-J., Kirz, J., Lindau, I.,

Pianetta, P., Winick, H., Williams, G. P. and Scofield, J. H. (2001). X-RAY DATA BOOKLET. Berkeley: **Lawrence Berkeley Laboratory**.

Yin, Y. and Alivisatos, A. P. (2004). Colloidal nanocrystal synthesis and the organic–inorganic interface. **Nature**. 437: 664.

Zhenfa, Z., Sun, Y., Zhu, X., Yang, Z., Dai, J., & Song, W. (2009). Synthesis and magnetic properties of CoFe_2O_4 ferrite nanoparticles. **Journal of Magnetism and Magnetic Materials**, 321(9), 1251-1255.



CHAPTER III

RESEARCH METHODOLOGY

This chapter describes the methodology for conducting experiments during the course of this thesis work. Materials preparations and principle of materials characterizations will be explained. However, the development of an in situ cell for XAS measurements, which is one of the main parts of this work, is given in the next separated chapter.

3.1 Materials preparation

3.1.1 Ferrous oxide

Iron oxide (FeO) is the material employed in this study for the commissioning test of the in-house developed in situ cell for temperature-dependent experiments. This is due to the fact that Fe could co-exist in different oxidation states and it is easily accessible with low-cost. Moreover, iron oxide has been used in many different applications, e.g. iron oxide pigments are frequently used in paints, coatings, construction materials, plastics, paper, glass, ceramics, and rubber goods to offer color, concealing power, and/or reinforcement. Iron oxides are also employed as a source of micronutrient iron in animal feeds and fertilizers, as well as catalysts in chemical processing. Ferrites (ceramic magnets) are made from specialized iron oxides with high purity and regulated homogeneity, which are used in computer memory cores, hi-fi speakers, color TV, and other electrical and electronic devices. Audio and video tapes and cassettes, as well as

magnetic printing inks, contain magnetic iron oxide pigments. Magnetic and electronic applications for iron oxide pigments are the fastest growing uses.

In this work, FeO pellets were synthesized by mixing FeO powder with Boron Nitride (BN). This is necessary for absorption measurement in a transmission. The mixed pellets have lower density and, thus, lower X-ray absorption allowing transmission of X-ray measurements possible. The FeO powder were weighed to the BN with FeO 50 mg and BN 150 mg shown as Figure 3.1. The pelletizing of the sample allows the measurements of the elements of interest more efficiently as a sample preparation for *in situ* heating cells. The dosage to be used for sample preparation is determined by the concentration of the substance. If the chemical is high concentrated, Cellulose, Boron Nitride, and SiO₂ can be mixed together to dilute it. Due to its low melting point, Cellulose cannot be combined with samples for *in situ* heating. The mixing ratio should be made in varied ratios depending on the concentration of the sample. A decent value for the sample to check the edge jump should be close to 1.00. For substances with low concentrations of trace elements it is not necessary to dilute the pellets of different weights to determine the best value for the edge jump. Different

pressures and compression times are used for different samples and dilutions; for mixed samples, Boron Nitride is applied at a pressure of 0.2 ton for 20 seconds.

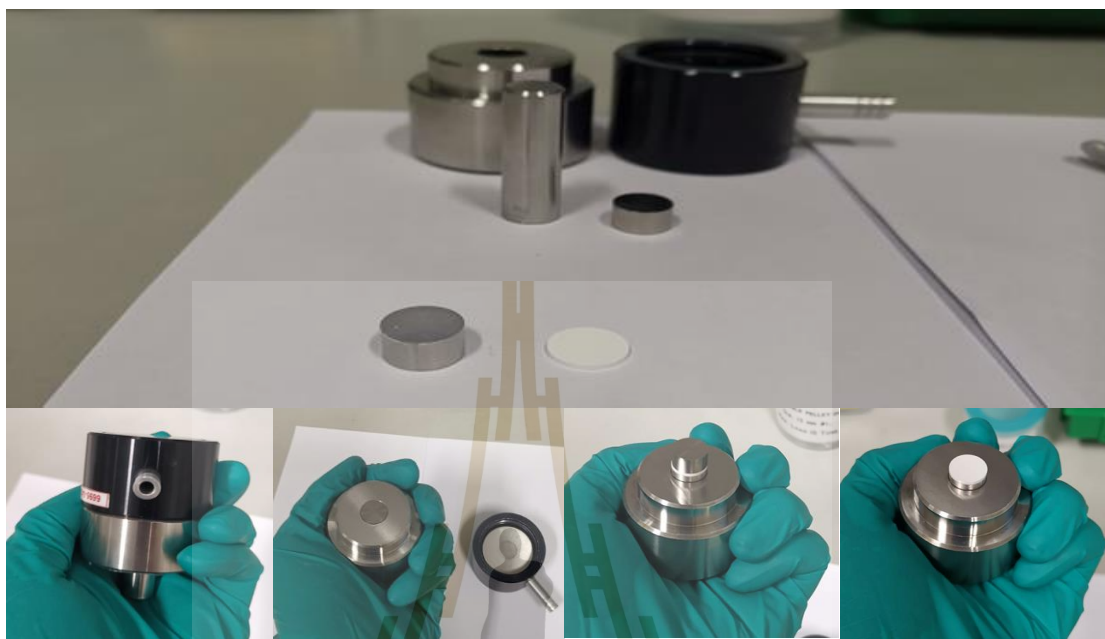


Figure 3.1 FeO pellet sample.

3.1.2 Lithium cobalt oxide

Due to its high specific capacity, minimal self-discharge, and excellent cycle life, lithium cobalt oxide (LiCoO_2) has attracted a lot of attention and interest as a cathode material in lithium-ion batteries (Plichta et al., 1989; Gibbard, 1989; Nagura and Tazawa, 1990; Kang et al., 1999; Patridge et al., 2013). This material's crystalline structure, average particle size, and particle size dispersion are critical for high-performance rechargeable lithium batteries. Many researchers used a solid-state process to make LiCoO_2 . However, to effectively synthesize LiCoO_2 , calcination at 850–900°C for many hours is necessary due to inadequate mixing and the poor reactivity of the starting components. Typically, LiCoO_2 exhibits two forms, a cubic phase and a hexagonal phase at low temperature (LT- LiCoO_2) and high temperature (HT- LiCoO_2),

respectively. The cubic and hexagonal structures are based on the same oxide sublattice, and are distinguished by the spatial arrangement of cations (Antolini, 2004). It has a hexagonal structure in which the Li^{+1} and Co^{3+} ions are ordered in the alternate (1 1 1) planes of octahedral sites, nearly cubic close packed oxygen lattice (Orman and Wiseman, 1984; Dahéron et al., 2008).

In this work, LiCoO_2 powder was synthesized by using the Co-precipitation method in ethanol solution with continuous magnetic stirring. Reagent-grade metal nitrate, $\text{LiNO}_3 \cdot 6\text{H}_2\text{O}$ (99.0%, Fluka) and $\text{Co}(\text{NO}_3)_2 \cdot 6\text{H}_2\text{O}$ (99.90%, Sigma-Aldrich) powders were used as raw materials. $\text{LiNO}_3 \cdot 6\text{H}_2\text{O}$ and $\text{Co}(\text{NO}_3)_2 \cdot 6\text{H}_2\text{O}$ were dissolved in ethanol with mole ratio of 1:1:1. The total mole concentration is 2.1 M and this solution was referred to as solution A. The 3 M of KOH was dissolved ethanol solution, which is referred as solution B. 100 mL of solution A was added slowly to 500 mL of solution B with continuous magnetic stirring at room temperature for 1 h. Finally, the dark precipitation of precursor was obtained. A solution was separated by centrifugal separator of 7000 rpm for 10 min and then washed powder with ethanol until free from nitrate, potassium and hydroxide ions and dried in air.

Several researches have been investigated these materials utilizing solid-state reaction and co-precipitation as synthesis techniques to understand the production of crystalline LiCoO_2 powders as a function of temperature. The crystal structure of the complex oxides of the LiCoO_2 was reviewed by Kellerman (Kellermann, 2001) where the formation, structure and transport properties of lithium cobalt oxide were studied carefully. In this research work, LiCoO_2 powders will be studied with both structural and physical studies by X-ray diffraction (XRD) and scanning electron microscopy (SEM). These LiCoO_2 powders were made using a fairly simple synthesis method using

solid state reaction and co-precipitation. In addition, synchrotron-based X-ray absorption spectroscopy (XAS) techniques such as *in situ* X-ray absorption near edge structure (*in situ* XANES) and *in situ* extended X-ray absorption fine structure (*in situ* EXAFS) were used to investigate the existence of cobalt oxidation states and local structural information around cobalt atoms.

3.1.2 Cobalt ferrite

Investigating the formation of local structure on magnetic properties of temperature has recently gained a great deal of attention. In this regard, it is usually not possible to maintain magnetic properties upon increasing temperature within high temperature. The vast application of nano ferrites in; permanent magnets, ferrofluids, storage devices, targeted drug delivery and other uses, has attracted much attention in their way of synthesizing these nano materials. CoFe_2O_4 is a well-known hard magnetic material with high coercivity (H_c) and moderate magnetization (M_s). The properties, along with their great physical and chemical stability, make CoFe_2O_4 nanoparticles suitable for magnetic recording applications such as audio and videotape, high density digital recording disks, etc. The ferrite spinel structure is based on a closed-packed oxygen lattice, in which tetrahedral (called A sites) and octahedral (called B sites) interstices are occupied by the cations. Spinel with only divalent ions in tetrahedral sites are called normal, while compounds with the divalent ions in the octahedral sites are called inverse. In the inverse spinel structure, all the Co^{2+} ions occupy the octahedral sites of lattice structure, half of the Fe^{3+} ions also occupy the same sites and the rest of the Fe^{3+} ions stay in tetrahedral sites.

In this work, the synthesis of cobalt ferrite was done with readily accessible chemicals. Sigma Aldrich provided all of the ingredients, including the metal salts

$\text{CoCl}_2 \cdot 6\text{H}_2\text{O}$ and $\text{FeCl}_3 \cdot 6\text{H}_2\text{O}$, starch, and ethanol. All of the chemicals purchased were analytical grade, and they were utilized just as they were received, with no additional purification. Using stoichiometric ratios of metal chlorides as precursors, water as a solvent, and potato starch as a surfactant, CoFe_2O_4 was produced via co-precipitation. In a typical synthesis, 10 mmol of $\text{CoCl}_2 \cdot 6\text{H}_2\text{O}$, 20 mmol of $\text{FeCl}_3 \cdot 6\text{H}_2\text{O}$ and 1.0 g of potato starch were dissolved in 150 ml of de-ionized water and magnetically stirred for 1 h about at 600 rpm at room temperature. The precipitating agent, 50 ml of 3M NaOH aqueous solution, was then added drop by drop until the pH rose above 11, at which point the metal hydroxides began to precipitate. The mixture was heated to 90°C , then refluxed for 2 hours at this temperature with continuous magnetic stirring (about 500 rpm). The reaction mixture was allowed to cool to room temperature naturally before being transferred to a 30mL centrifuge tube with de-ionized water. To isolate the supernatant liquid, the de-emulsified mixture was centrifuged at about 5500 rpm for 20 minutes. To remove the salt content, the precipitate was washed four times with de-ionized water and twice with ethanol, centrifuged, and then dried at 90°C for 12 hours in a hot air oven to remove the surplus ethanol and water. Further, the obtained co-precipitation product was annealed different; 400°C , 600°C , 800°C , and 800°C for 6 h in air.

3.2 Materials Characterizations

3.2.1 X ray diffraction

X-ray diffraction technique is a non-destructive sample used to analyze the phases of the crystal structure, the arrangement of atoms in the molecules of various

compounds, and the composition of the elements which can identify the crystals structure and crystalline size of material. However, amorphous materials cannot be measured using X-ray diffraction since the fundamental concept of X-ray diffraction considers X-ray reflection on each crystal plan. As illustrated in Figure 3.2. The X-ray beam's wave nature produces reflection and a route difference between two plans equal to the wavelength of the X-ray beam. The Bragg's law determines the relationship between d-spacing, the angle of the X-ray beam, and the wavelength of the X-ray, as

$$d_{hkl} = \frac{n\lambda}{2\sin\theta} \quad (3.1)$$

where d stands for the distance between consecutive atomic plans, also known as "d-spacing", θ is the X-ray beam's angle, n stands for the diffracted beam's order and the wavelength of the incident X-ray beam is represented by λ .

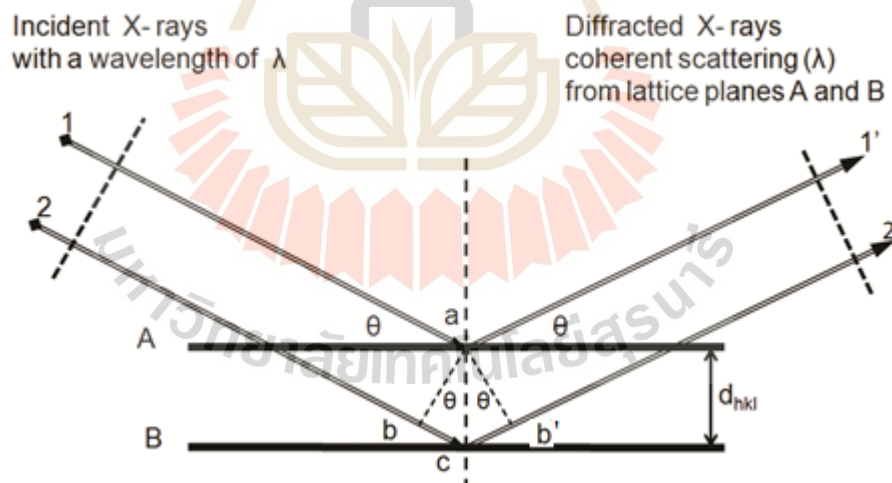


Figure 3.2 Schematic representation of X-ray diffraction from parallel planes.

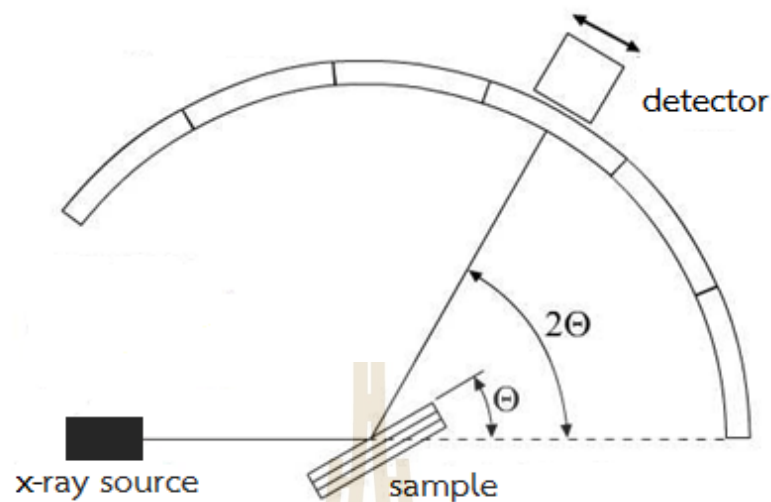


Figure 3.3 Schematic drawing of XRD measurement setup.

In this technique, the sample material is rotated by an angle θ , while the X-ray detector is moved by an angle of 2θ to achieve diffraction in accordance with Bragg's law as shown in Figure 3.3. The Bragg condition can be satisfied for any set of planes whose spacing is greater than half the wavelength of the X-ray used (if $d < \lambda/2$, then $\sin(\theta) > 1$, which is impossible). This condition sets a limit on how many orders of diffracted waves can be obtained from a given crystal using an X-ray beam of a given wavelength. Since the crystal pattern repeats in three dimensions, forming a three-dimensional diffraction grating, three integers, denoted $(h\ k\ l)$ are required to describe the order of the diffracted waves. The Miller indices, which are used in crystallography to represent the orientation of the reflecting sheets with respect to the unit cell and the path difference in units of wavelength between identical reflecting sheets, are defined as these three integers.

An X-ray diffractometer is used to perform the X-ray diffraction method. The following are the key elements of an X-ray diffractometer (Fultz and Howe, 2008):

- An X-ray source X-ray, usually a sealed X-ray tube
- A goniometer, which provides precise mechanical motions of the sample and detector
- Specimen and detector
- An X-ray detector
- Electronics for counting detector pulses in synchronization with the positions of the goniometer

The Debye-Scherrer Method, Laue Method, Rotating Crystal Method, and θ - 2θ diffractometer Method are four practical techniques for observing diffractions and producing diffraction measurements. All of this is done to ensure that Bragg's law is followed. The schematic diagram of θ - 2θ X-ray diffractometer used in this work (Rigaku SmartLab equipped with Cu K_{α} sealed tube, wave length 1.5418 Å) is shown in Figures 3.4 and 3.5. The θ - 2θ diffractometer is used for diffraction measurements of unfixed horizontal sample. For this purpose, sample will be rotated to θ and X-ray detector moved to 2θ . The diffraction angle follows the Bragg's equation (3.1)). In this thesis work, room temperature XRD data was collected in the 2θ scan range of 10–60° with step size of 0.02° and scanning rate of 2.5° per minute.

3.2.2 Scanning electron microscope

The scanning electron microscope (SEM) is an important electron microscope that generates a variety of signals at the surface of solid objects using a concentrated beam of high-energy electrons. The signals produced by the interaction of a focused beam of high-energy electrons with the atoms of the target sample reveal information about the sample's external morphology (texture), chemical composition, and crystalline structure and orientation of the materials that make up the sample, among other things (Brandon and Kaplan, 1999).

Figure 3.6 shows a schematic representation of a scanning electron microscope. In an electron column above the sample chamber, the SEM creates a stream of incoming electrons. A thermal emission source, such as a heated tungsten filament, or a field emission cathode create the electrons. Depending on the evaluation objectives, the incident electrons' energy can range from 100 eV to 30 keV. A set of electromagnetic lenses in the SEM column concentrate the electrons into a narrow beam. The concentrated beam is directed and positioned onto the sample surface by scanning coils towards the end of the column. For imaging, the electron beam is scanned in a raster pattern across the surface. For X-ray analysis, the beam can be concentrated at a single spot or scanned along a line. The beam may be focused down to a probe diameter of roughly 10 microns. A huge number of signals are created when the electron beam impacts a specimen. Secondary electrons, backscattered electrons, characteristic X-ray, cathodoluminescence, and transmitted electrons are all examples of these signals, as illustrated in Figure 3.8.

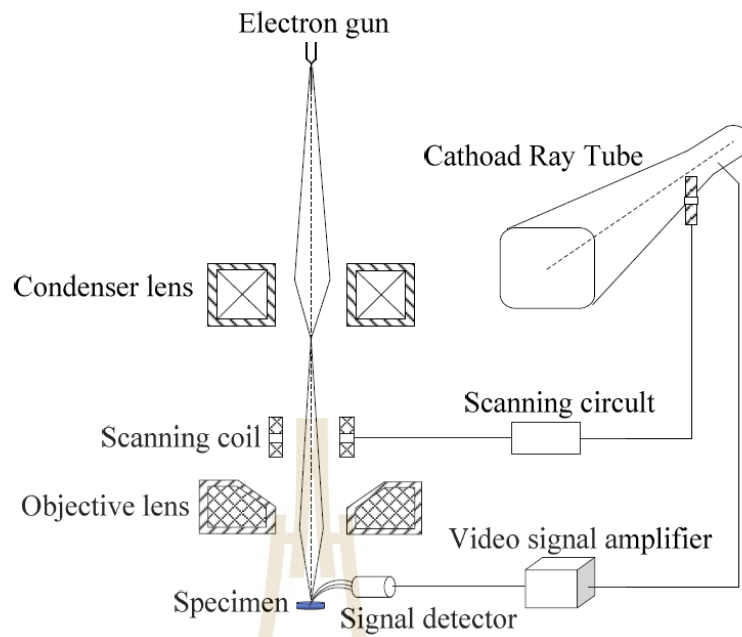


Figure 3.6 Principles schematic illustration of SEM. (JEOL, Ltd., 1989).

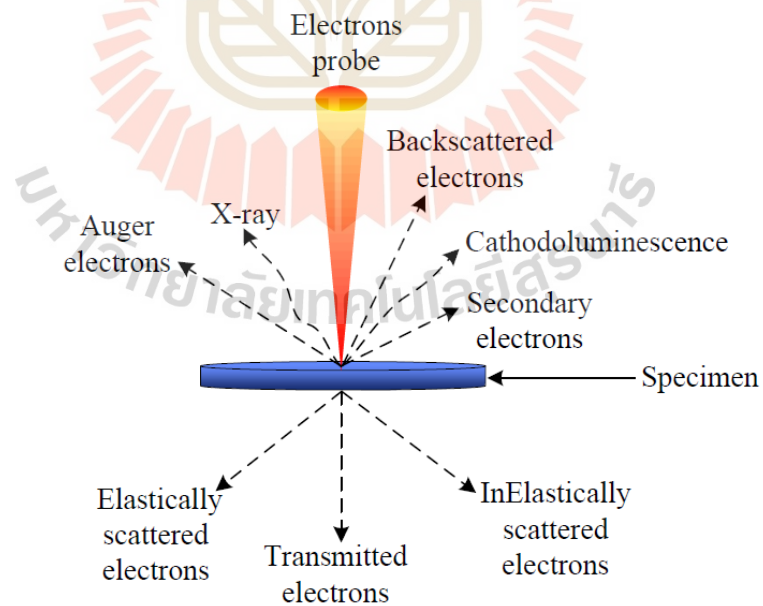


Figure 3.7 Schematic diagram of signals in SEM.

In SEM, there are four major signals to employ:

1) Secondary electrons (SE) are expelled lower-energy electrons that can be produced by inelastic collisions with the nucleus that result in significant energy loss or by the ejection of loosely bound electrons from sample atoms. Secondary electrons have an energy of 50 eV or less. The number of electrons that reach the secondary electron detector from any location on the scanned surface is influenced by the topography of surface characteristics. The visual contrast that shows the surface morphology is created by this local change in electron intensity. For a tungsten-filament electron source SEM, the secondary electron image resolution for an ideal sample is around 3.5 nm, or 1.5 nm for field emission SE.

2) Backscattered electrons are high-energy electrons that are expelled when an incoming electron collides with the nucleus of a sample atom in an elastic collision. Surface topography is not as precisely resolved as secondary electron imaging because high-energy electrons can escape from far deeper than secondary electrons. Backscattered electron generation efficiency is related to the mean atomic number of the sample material, resulting in picture contrast as a function of composition, with greater atomic number material appearing brighter than lower atomic number material in a backscattered electron image. Backscattered electron imaging has a resolution of around 5.5 nm.

3) When the electron beam interacts with the inner shell electrons of the specimen atoms by inelastic scattering with enough energy to excite inner shell electrons to outer shell orbitals, leaving inner-shell vacancies, characteristic X-rays are produced. As outer-shell electrons fall into different inner-shell orbitals, different quantities of energy are produced depending on the target element and the kind of

orbital decay. These distinct X-rays are utilized to identify the component and count the numerous components present in the sample.

4) Cathodoluminescence (CL), the emission of light when atoms excited by high-energy electrons come back to their ground state. In the SEM, CL detectors either collect all light emitted by the specimen, or can analyze the wavelengths emitted by the specimen and display an emission spectrum or an image of the distribution of cathodoluminescence emitted by the specimen in real colour.

To create an SEM image, the incident electron beam is scanned in a raster pattern across the sample's surface. The emitted electrons are detected for each position in the scanned area by an electron detector. The intensity of the emitted electron signal is displayed as brightness on a cathode ray tube (CRT). By synchronizing the CRT scan to that of the scan of the incident electron beam, the CRT display represents the morphology of the sample surface area scanned by the beam. Magnification of the CRT image is the ratio of the image display size to the sample area scanned by the electron beam. Two electron detector types are predominantly used for SEM imaging. Scintillator type detectors (Everhart-Thornley) are used for secondary electron imaging. This detector is charged with a positive voltage to attract electrons to the detector for improved signal to noise ratio. Detectors for backscattered electrons can be scintillator types or a solid-state detector. The SEM column and sample chamber are at a moderate vacuum to allow the electrons to travel freely from the electron beam source to the sample and then to the detectors. High-resolution imaging is done with the chamber at higher vacuum, typically from 10^{-5} to 10^{-7} Torr. Imaging of nonconductive, volatile, and vacuum-sensitive samples can be performed at higher pressures.

The analytical technique of energy dispersive X-ray spectroscopy (EDS) is used to detect and quantify elemental compositions in a very tiny sample of material. The scanning electron microscope has EDS as a standard feature. The surface under examination is blasted with an electron beam when a SEM picture is taken. Figure 3.8 shows a schematic of the EDS system. The bombardment of electrons leads atoms to excite, resulting in the release of surplus energy in the form of X-ray. Some electrons are taken from the atoms on the sample surface when the sample surface is blasted by an electron beam. As a result, holes in the electron shell must be supplied by electrons from a higher shell. As a result, to balance the energy difference between the two electrons, an X-ray is produced. The quantity of energy released is dependent on the atoms it excites, creating different peaks in the energy spectrum depending on the material's composition. EDS is a qualitative and quantitative composition diagnostics technique because the intensities or regions of the different peaks of a given spectrum are proportional to the concentration of that specific element.

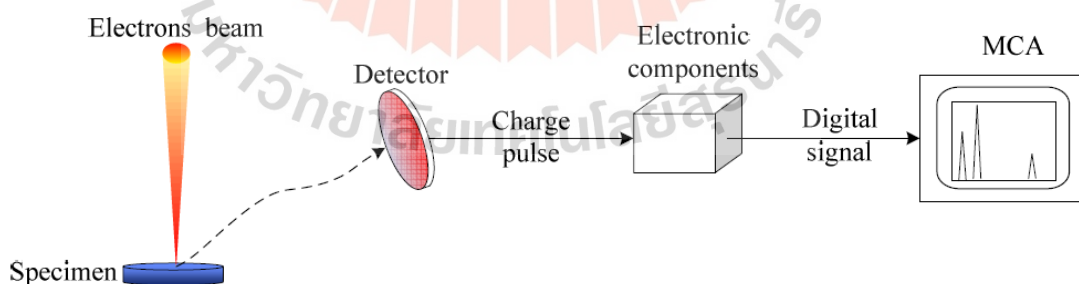


Figure 3.8 Schematic diagram of an EDS.

3.2.3 X-ray Absorption Spectroscopy

3.3.3.1 X-ray Absorption Spectroscopy Experimental setup

Due to the high intensity and energy alterable competence of produced X-ray photons, as well as the ability to acquire a continuous absorption spectra across a wide energy range, X-ray absorption spectroscopy is typically performed at a synchrotron radiation source. As illustrated schematically in Figure 3.9, there are three types of X-ray absorption measurements: transmission-mode XAS, fluorescence-mode XAS, and electron-yield XAS.

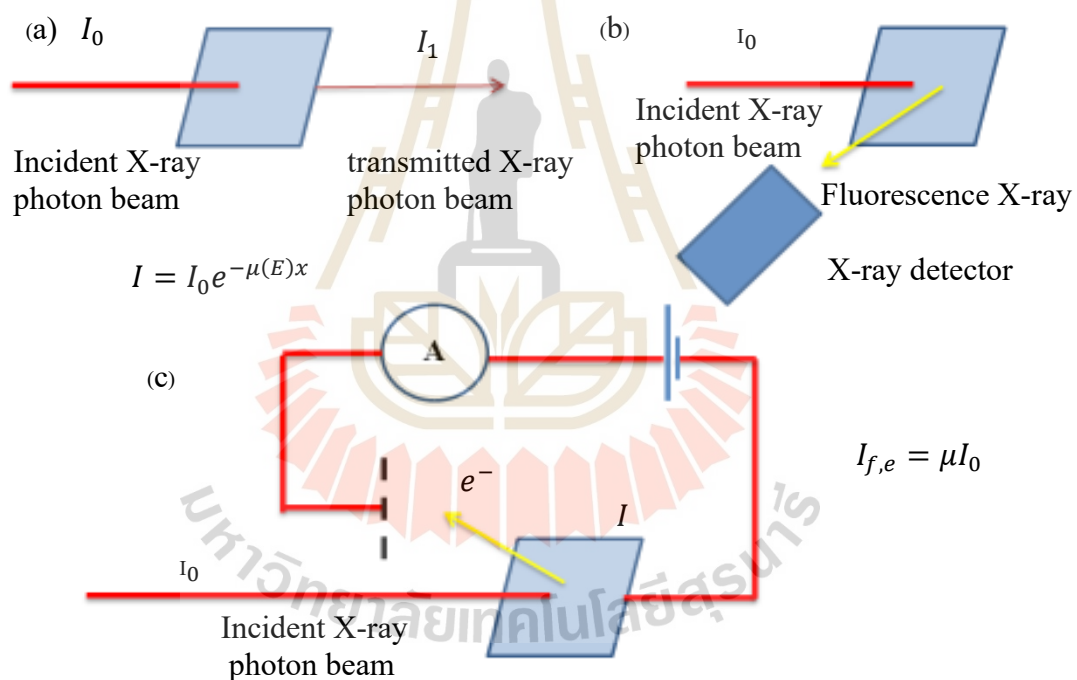


Figure 3.9 Transmission mode, fluorescence mode, and electron yield are the three modalities of XAS measurement. [adapted from (Kawai, 2000).

In transmission mode XAS, the intensities of incident X-ray photon beam (I_0) and transmitted X-ray photon beam (I) are measured by ionization chambers after the energy of X-ray photons is altered by X-ray double crystals monochromator, as

illustrated in Figure 10. We make sure the X-ray photon beam is accurately positioned on the sample in this mode. Figure shows the experimental setup of the XAS experimental station at the XAS beam line, Siam Photon Laboratory, SLRI.

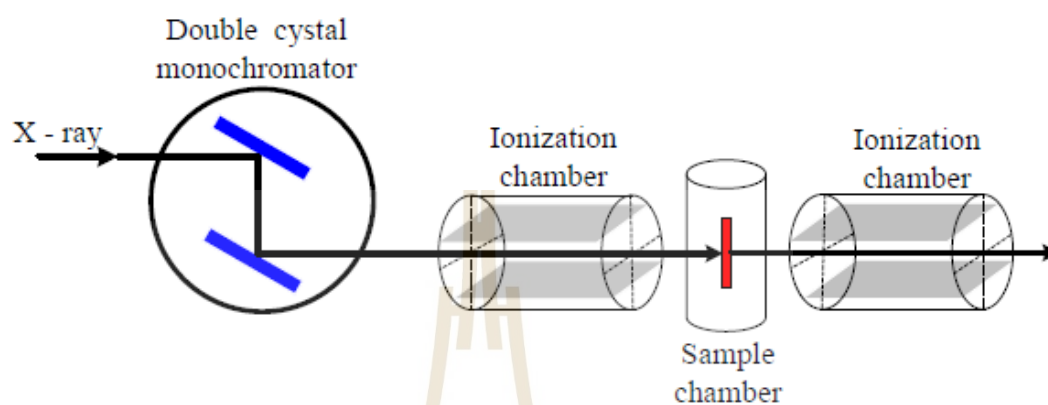


Figure 3.10 Schematic illustration of the experimental setup of transmission-mode X-ray absorption spectroscopy. (Jutimoosik, 2010).

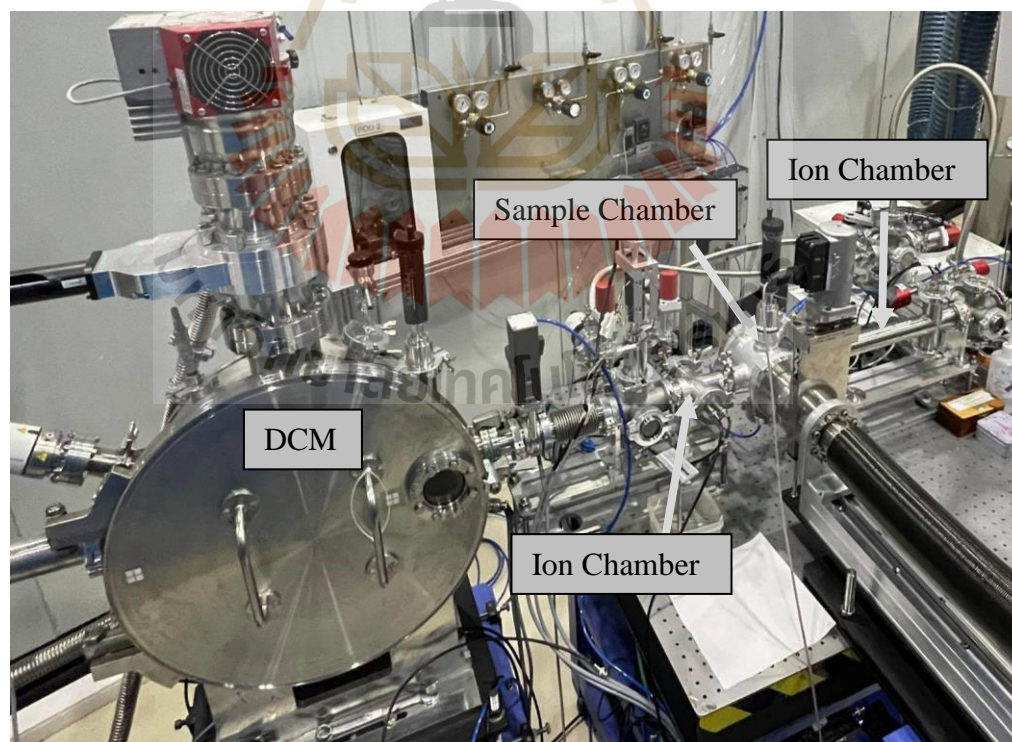


Figure 3.11 Transmission-mode X-ray absorption spectroscopy experimental setup diagram.

The absorption coefficient may also be measured using the fluorescence mode and the electron yield, in addition to the transmission mode. When an X-ray photon knocks out an electron from the inner shell, an electron from a higher energy level cascades down to fill up the hole, discharging energy as radiation. The discharged energy X-ray photon is emitted, as shown in Figure 12(a), and the fluorescence X-ray may be observed. De-excitation can also induce the Auger effect, in which one electron is reduced to a lower energy level, while a second electron is stimulated to the continuum state and perhaps escapes the sample, as illustrated in Figure 12(b), where it can be detected with electron-yield XAS detectors.

We measure the intensities of the incident X-ray photon beam and the fluorescence X-ray that is produced after the X-ray absorption in fluorescence mode. The fluorescence detector is generally positioned in the horizontal plane at 90° to the incident X-ray photon beam, with the sample at an angle (commonly 45°) to the beam. Because fluctuations in the quantity of elastically scattered X-rays are a substantial source of noise in fluorescence XAS, the detector's location is chosen to reduce elastically scattered radiation by utilizing the X-ray beam's polarization. In the instance of electron yield, we count the electrons released from the sample's surface. The method is surface-sensitive due to the short route length (1000 \AA), which might be advantageous if one is interested in near-surface events. It can also help prevent the "self-absorption" phenomenon that happens in fluorescence mode. Both modes, however, are instantaneously identical to the sample's absorption capabilities. As a result, the three approaches may be changed to examine the structure of a material utilizing the sample's absorption ability.

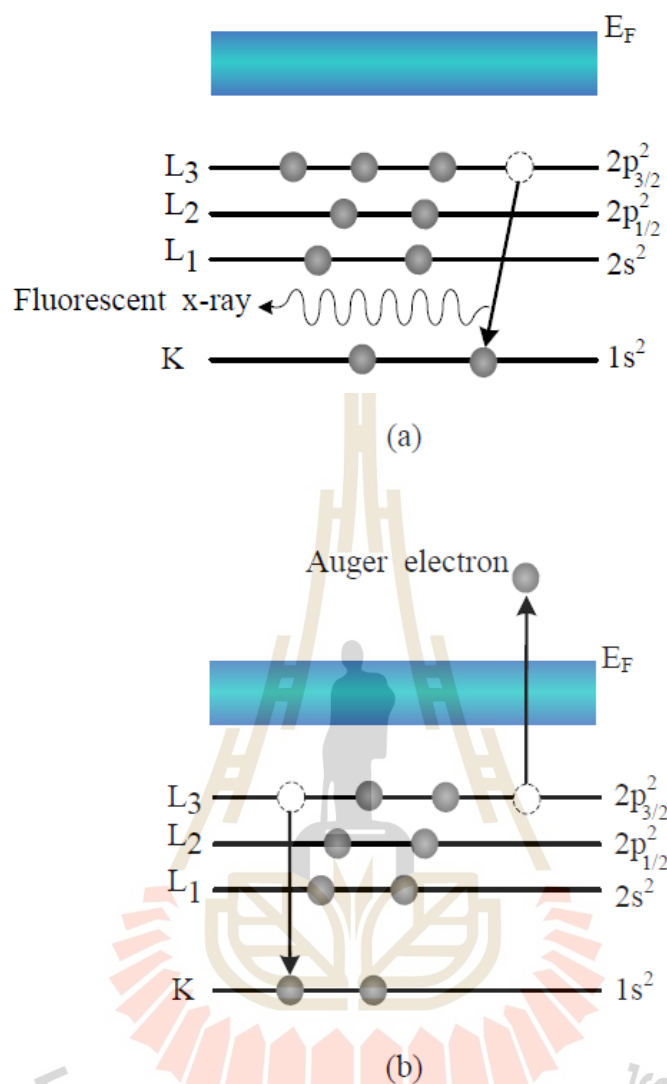


Figure 3.12 The excited state (a) X-ray fluorescence and (b) the Auger effect. [adapted from (Koningsberger and Prins, 1988)].

3.3.3.2 X-ray absorption spectrum calculation

The main theoretical computations in this thesis are performed using the FEFF 8.2 code. The FEFF (feff) project, developed by the Department of Physics at the University of Washington in Seattle, USA, uses this code to compute X-ray absorption. Apart from XAS spectra calculation, FEFF code can also calculate X-ray natural

circular dichroism (XNCD), spin-dependent calculations of X-ray magnetic dichroism (XMCD), nonresonant X-ray emission (XES) and electronic structure including local densities of states (LDOS). FEFF code is written in ANSI FORTRAN 77 with principle investigator John J. Rehr and co-principle investigator Alexei L. Ankudinov (Rehr and Albers, 2000).

FEFF is a self-consistent real-space multiple-scattering (RSMS) algorithm for calculating X-ray absorption spectra and electronic structure simultaneously. As illustrated in Figure 13, the input file “feff.inp” may be generated directly from ATOMS code using “atoms.inp.”

```

File Edit Format View Help
## This Atoms file was generated by Demeter 0.9.26
## Demeter written by and copyright (c) Bruce Ravel, 2006-2018

title = LiCoO2
space = P 1
a   = 2.84290   b   = 2.84290   c   = 14.14562
alpha = 90.00000   beta = 90.00000   gamma = 120.00000
rmax = 4.26435   core = Co3
polarization = 0.0 0.0 0.0
shift = 0.00000 0.00000 0.00000
atoms
# el.   x       y       z       tag
Li   0.00000 0.00000 0.00000 Li0
Li   0.66667 0.33333 0.33333 Li1
Li   0.33333 0.66667 0.66667 Li2
Co   0.33333 0.66667 0.16667 Co3
Co   0.00000 0.00000 0.50000 Co4
Co   0.66667 0.33333 0.83333 Co5
O    0.00000 0.00000 0.23959 O6
O    0.66667 0.33333 0.09375 O7
O    0.66667 0.33333 0.57292 O8
O    0.33333 0.66667 0.42708 O9
O    0.33333 0.66667 0.90625 O10
O    0.00000 0.00000 0.76041 O11

```

Figure 3.13 Detail of an atoms.inp input file to generate “feff.inp” for FEFF calculation.

The input file “feff.inp,” which is displayed in Figure 13, can be modified to specify the appropriate commands, parameters, and atomic locations for FEFF-XAS spectrum computations. This file provides information such as the input file's generator

and the number of atoms included in the cluster. The next sections go through how to allocate the steps of a computation using various cards. In the next section, the types of atomic potentials and specified atomic symbols are discussed, followed by the positions of the generated atoms in the system, with the center atom at (0,0,0) in (x,y,z) coordination.

```

TITLE LiCoO2

HOLE      1  1.0  * FYI: (Co K edge @ 7709 eV, 2nd number is S0^2)
*          mphase,mphase,mfeff,mchi
CONTROL   1  1  1  1
PRINT     1  0  0  0

RMAX      5.0
* POLARIZATION 0.0  0.0  0.0

POTENTIALS
* ipot  Z  tag
  0  27  Co
  1  3   Li
  2  27  Co
  3  8   O

ATOMS
* this list contains 33 atoms
*  x      y      z  ipot tag  distance
  0.00000  0.00000  0.00000  0  Co3  0.00000
  0.82069  1.42142 -1.03150  3  O7.1  1.93855
 -1.64133 -0.00003 -1.03150  3  O7.1  1.93855
 -0.82067  1.42143  1.03150  3  O6.1  1.93855
  1.64136 -0.00001  1.03150  3  O6.1  1.93857
 -0.82067 -1.42146  1.03150  3  O6.1  1.93857
  0.82069 -1.42148 -1.03150  3  O7.1  1.93859
  2.46202  1.42145  0.00000  2  Co3.1  2.84290
 -2.46202  1.42145  0.00000  2  Co3.1  2.84290
  0.00000  2.84290  0.00000  2  Co3.1  2.84290
  2.46202 -1.42145  0.00000  2  Co3.1  2.84290
 -2.46202 -1.42145  0.00000  2  Co3.1  2.84290
  0.00000 -2.84290  0.00000  2  Co3.1  2.84290
  0.82069  1.42142  2.35751  1  Li1.1  2.87260
 -1.64133 -0.00003  2.35751  1  Li1.1  2.87260
  0.82069 -1.42148  2.35751  1  Li1.1  2.87263
 -0.82067  1.42143 -2.35765  1  Li0.1  2.87271
  1.64136 -0.00001 -2.35765  1  Li0.1  2.87273

```

Figure 3.14 Detail of a “feff.inp” input file of LiCoO₂ with Co as center atom for FEFF calculation.

3.4 References

- Antolini, E. (2004). LiCoO₂: formation, structure, lithium and oxygen nonstoichiometry, electrochemical behaviour and transport properties. **Solid State Ionics**. 170(1): 159–171.
- Brandon, D. G. and Kaplan, W. D. (1999). **Microstructural characterization of materials**. Chichester: Wiley.
- Dahéron, L., Dedryvère, R., Martinez, H., Ménétrier, M., Denage, C., Delmas, C. and Gonbeau, D. (2008). Electron transfer mechanisms upon lithium deintercalation from LiCoO₂ to CoO₂ investigated by XPS. **Chemistry of Materials**. 20(2): 583–590.
- Gibbard, H. F. (1989). High temperature, high pulse power lithium batteries. **Journal of Power Sources**. 26(1–2): 81–91.
- Inaba, K. Kobayashi, S. Uehara, K. Okada, Reddy, A. S. and Endo, T. (2013). "High Resolution X-ray Diffraction Analyses of (La,Sr)MnO₃/ZnO/Sapphire (0001) Double Heteroepitaxial Films" . **Advances in Materials Physics and Chemistry**. 1A: 72-89.
- Jutimoosik, J. (2010). **Local Structure of Magnesium Zinc Oxide Nanocrystals**. M.S. thesis, Suranaree University of Technology. Nakorn Ratchasima.
- Kang, S. G., Kang, S. Y., Ryu, K. S. and Chang, S. H. (1999). Electrochemical and structural properties of HT-LiCoO₂ and LT-LiCoO₂ prepared by the citrate sol-gel method. **Solid State Ionics**. 120(1–4): 155–161.
- Kawai, J. (2000). **Absorption techniques in X-ray spectrometry**, **Encyclopedia of analytical chemistry**. New York: Wiley.

- Kellermann, D. G. (2001). Magnetic properties of complex oxides LiMO_2 ($M = \text{Sc-Ni}$) with different types of cationic ordering. *Russ. Chemical Reviews*. 70(9): 777.
- Koningsberger, D. C. and Prins, R. (1988). **X-ray Absorption: Principles Applications, Techniques of EXAFS, SEXAFS, and XANES**. John Wiley and Sons Inc.
- Nagura, T. and Tazawa, K. (1990). Lithium-ion rechargeable battery. *Prog. Batter. Solar Cells*. 9: 209–217.
- Orman, H. J. and Wiseman, P. J. (1984). Cobalt (III) lithium oxide, CoLiO_2 : structure refinement by powder neutron diffraction. *Acta Crystallogr*. C40: 12–14.
- Patridge, C. J., Love, C. T., Swider-Lyons, K. E., Twigg, M. E. and Ramaker, D. E. (2013). *in situ* X-ray absorption spectroscopy analysis of capacity fade in nanoscale LiCoO_2 . *Journal of Solid State Chem*. 203: 134–144.
- Plichta, E., Slane, S., Uchiyama, M., Saloman, M., Chua, D., Ebner, W. and Lin, H. (1989). An improved $\text{Li/Li}_x\text{CoO}_2$ rechargeable cell. *Journal of the Electrochem. Society*. 136(7): 1865–1869.
- Rehr, J. J. and Albers, R. C. (2000). Theoretical approaches to X-ray absorption fine structure. *Reviews of Modern Physics*. 72: 621.

CHAPTER IV

DEVELOPMENT OF *in situ* XAS HEATING CELL

The *in situ* XAS is an advanced technique for real-time investigations of reaction changes at different temperatures to obtain the structure and chemical characteristics of semiconductors, polymer and magnetic materials, as well as to track changes during chemical reactions and interactions (An, 2014). Before this work, simple *in situ* XAS in high-temperature environments experimntscould not be performed at the BL5.2 of SLRI. The existing system was too complicated and, thus, inconvenient to use. More importantly, it took a long time to install and to change samples, preventing the experiments, often, to be completed within the allocated beam time. Therefore, in this work, a simple *in situ* XAS cell was developed to fulfill the above-mentioned missing requirements. This chapter describes the design concepts and detailed technical specifications of the the *in situ* cell developed during the course of this work.

4.1 Descriptions of *in situ* cell

In this work, the *in situ* cell is designed for XAS measurements in a transmission mode of measurement. The cell allows the samples for XAS measurements to be in an ambient atmosphere. The cell was designed for XAS measurements of samples heated up to 1000°C under an inert atmosphere or special gas of interest (H₂, N₂ and O₂) which flow rate range from 1 to 100 ml/min. The temperature can be controlled to be a linear or step changes patterns.

The drawings of the developed *in situ* XAS cell are shown in Figure 4.1. The cell consists of three parts: (1) the stainless steel (AISI304) chamber (2) heater and temperature controller and (3) sample holder. Cylindrical shape of the cell was adopted for an ease of fabrication using existing stainless-steel tube available at SLRI. The diameter of the tube is 260 mm. The total length of the cell, or the length required for the installation in the measurement system, is 421 mm. Both ends of the AIS304 cylindrical chamber is welded with 20-mm stainless-steel tubes ended with KF40DN flanges, acting as the entry and exit port for X-rays, for connecting to the ionization chambers of the XAS measuring set up. Proper window materials, such as polypropylin, are used to isolate the atmosphere in the cell from the ionization chambers. The 20-mm stainless tube of the entry and exit ports are water-cooled to maintain the KF40DN flanges to be at room temperature. The CF70 port on top of the chamber was designed for mounting the sample holder. The chamber is divided into two parts, top and bottom sections. The top section can be opened to access the internal part. The chamber is equipped with adjustable support legs to attach with the supporting table and level with the synchrotron beamline. Table 4.1 provides the information of the positions and materials used in fabricating the *in situ* cells.

In designing the heat shielding system, the reducing the beam path length and cell size was taken into account. Inside the cell, there is a heating area along the beam direction of about 150 mm. Ceramic blocks with thickness of 80 mm were used as heat insulator, installed as shown in Figure 4.1. More detailed information of heating elements and thermocouples used for in this cell is given in the next section.

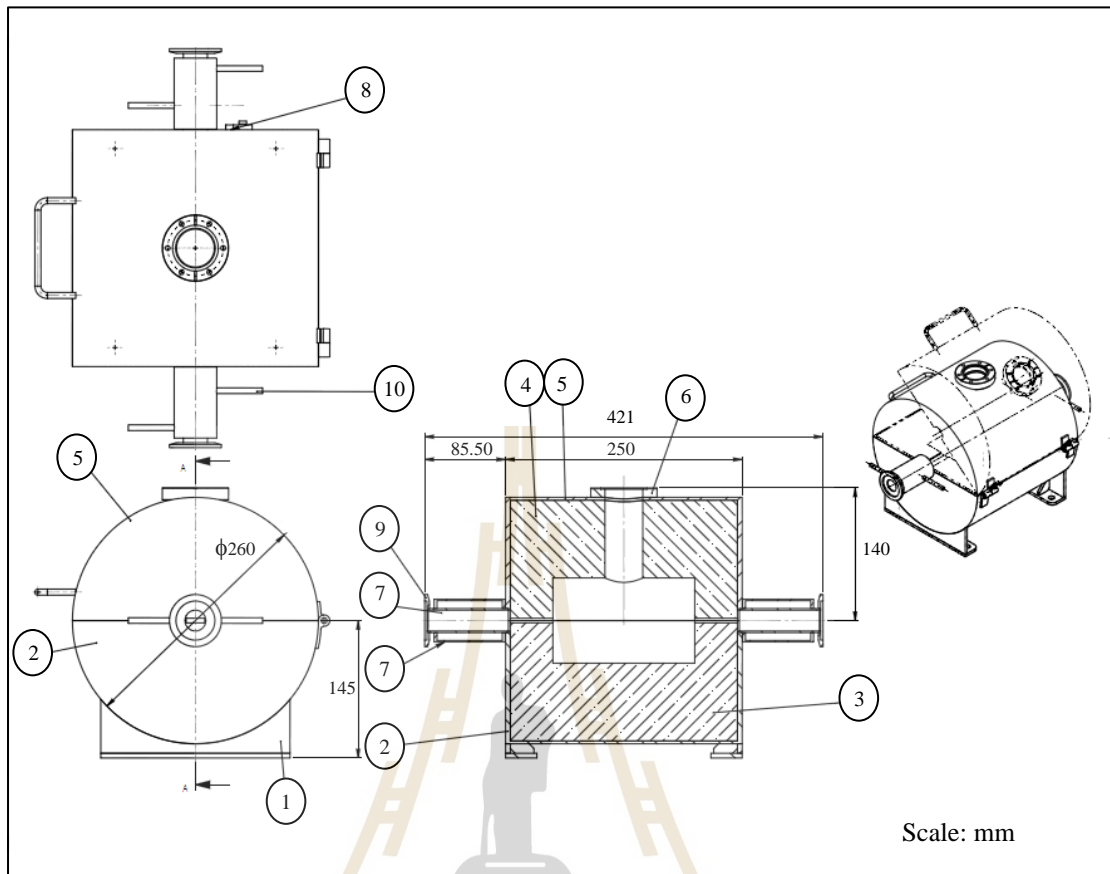


Figure 4.1 Schematic drawing of the *in situ* cell.

Table 4.1 The components of the *in situ* cell.

Position	Description	Material
1	Base	AISI304
2	Side plate	AISI304
3	Lower ceramic	Ceramic
4	Top ceramic	Ceramic
5	Top cover	AISI304
6	CF70 Bored	AISI304
7	Entry-exit tube	AISI304
8	Arm hold	AISI304
9	KF40DN Weld Flange	AISI304
10	Cooling Tube	AISI304

Two different types of sample holder were developed depending XAS measurement requirements. When on gas flow is required, samples could be mount on a simply sample holder, as shown in Figure 4.2, inserting from the top of the cell. This sample holder is attached on one end of the insulating ceramic which welded to the CF70 flange. The sample holder is made of high-temperature-resistant stainless steel with dimensions of $30 \times 42 \times 15 \text{ mm}^3$.

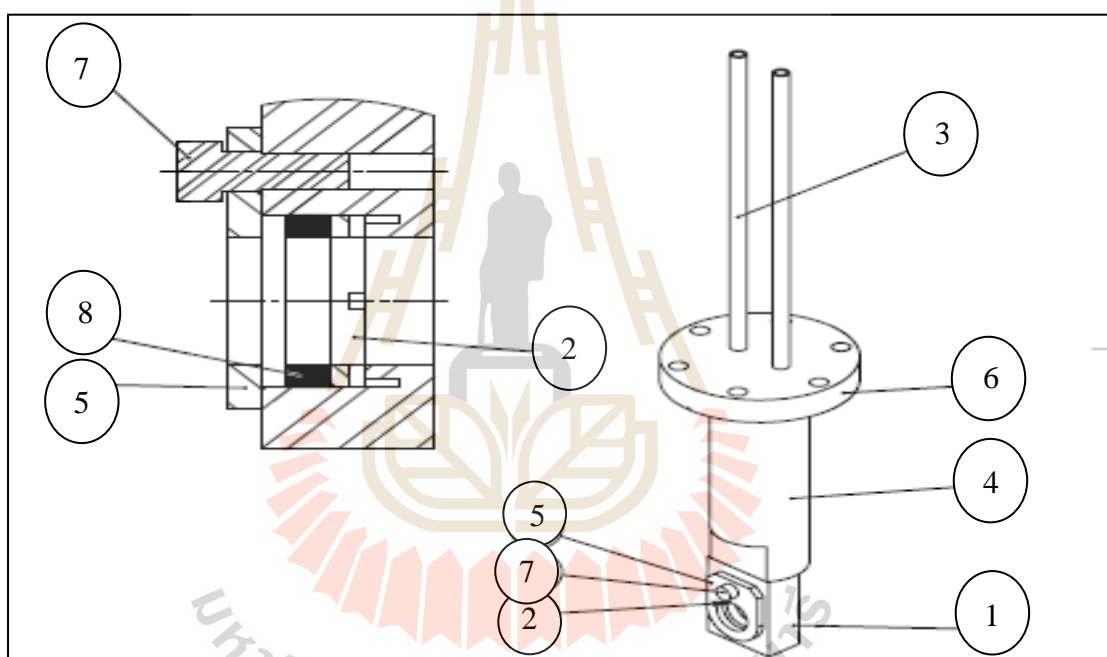


Figure 4.2 The drawing of the sample holder.

Table 4.2 The components of the sample holder.

Position	Description	Material
1	Body	AISI310
2	Gas ring	AISI310
3	Entry-exit gas	AISI304
4	Insulation	Ceramic
5	Lid lock a sample	AISI304
6	CF70 Flange	AISI304
7	Pin	AISI310
8	Washer	AISI310

However, when gas flow is required during XAS measurements, the samples are loaded in a small boat inserting into a special quartz chamber, as shown in Figure 4.3. This sample chamber is made of a quartz tube with diameter of 20 mm. Both ends of the quartz tube are mounted to vacuum fittings made of stainless steel to allow this parts to connect to the XAS measurement system. There are gas-inlet and -outlet ports. The total length of this sample chamber is 550 mm.

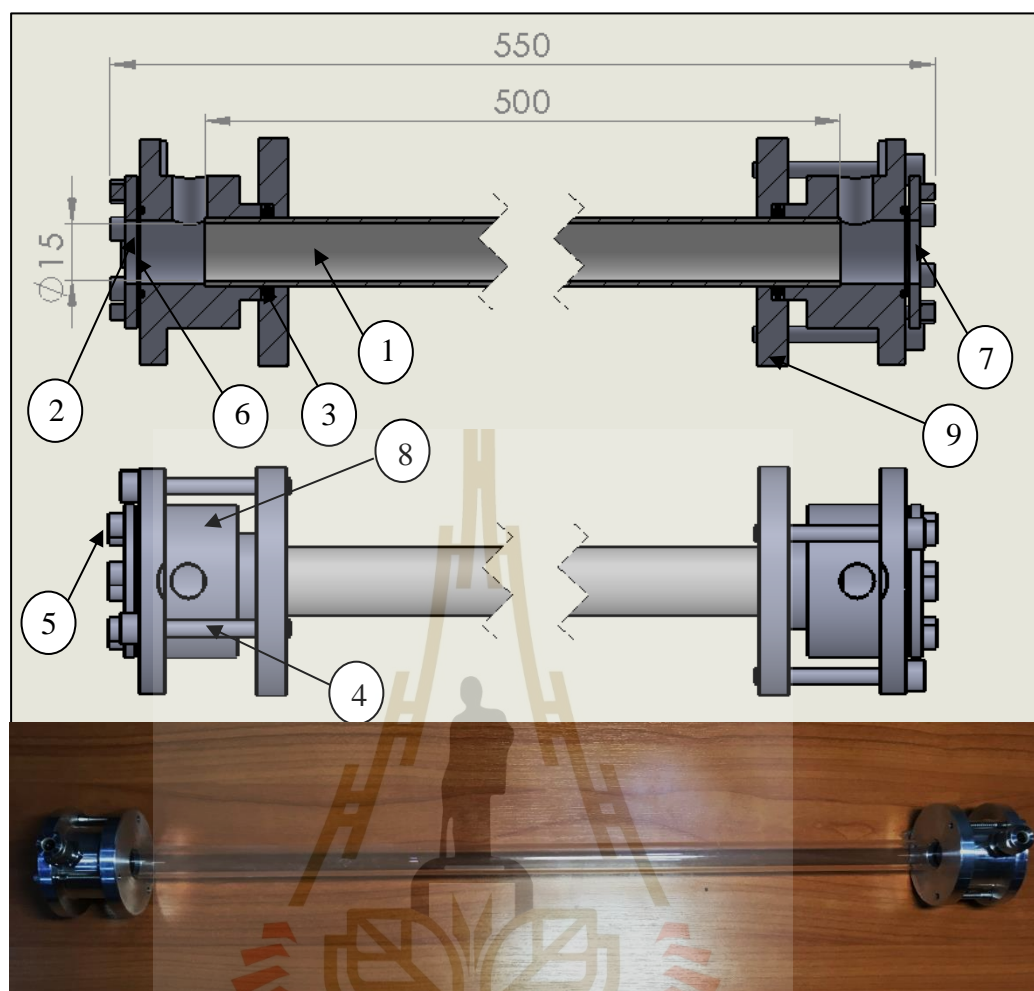


Figure 4.3 Schematic of a quartz tube system fixes samples that supply flow gas.

Table 4.3 The components of the quartz glass.

Position	Description	Material
1	Quartz glass	Quartz
2	O Ring ID: 15 Thickness: 3	Rubber
3	O Ring ID: 18 Thickness: 2	Rubber
4	Nuts and bolts M4	Stainless steel
5	Nuts and bolts M3	Stainless steel
6	Film	PP film
7	Tapped Fixed Bored CF	Al
8	Body	Al
9	Tapped Fixed Bored CF	Al

4.2 Heater and temperature controller

Electric heating materials are chosen based on their inherent resistance to current flow in order to generate heat. It is noted that the copper wire does not create enough heat when carrying electricity due to its low resistance. As a result, to be used as an electric heating element, a of wire, rod, strip or ribbon shall be employed for this application. Thus, the alloy for using as a heating element for this work should have the following characteristics:

- Small cross-sectional area with sufficiently high electric resistance.
- High ductility and strength at the operating temperatures.
- Low-temperature coefficient in electric resistance to avoid large variations in resistance at room temperature up to operating temperature.
- Excellent resistance to oxidation in air while moderate processes.
- The alloy can withstand higher temperatures than our operating temperatures.
- Possibility of being molded into the desired shape and suitable working.

From the above requirement, nichrome resistance heating wire is selected for the heating element of the *in situ* cell. This wire can withstand temperatures of up to 1400°C and has good oxidation resistance, high melting point stability and low elongation when heated. The heater assembly of the cell is shown in Figure 4.4. Ceramic was selected as an insulator that can withstand high temperatures. It is a good thermal insulator. It, does not expand greatly when heated and, more importantly, could be purchased with low price. Inside the cell, there is a heating area of about 150 mm which is covered with 80 mm thick insulating ceramic and covered stainless steel.

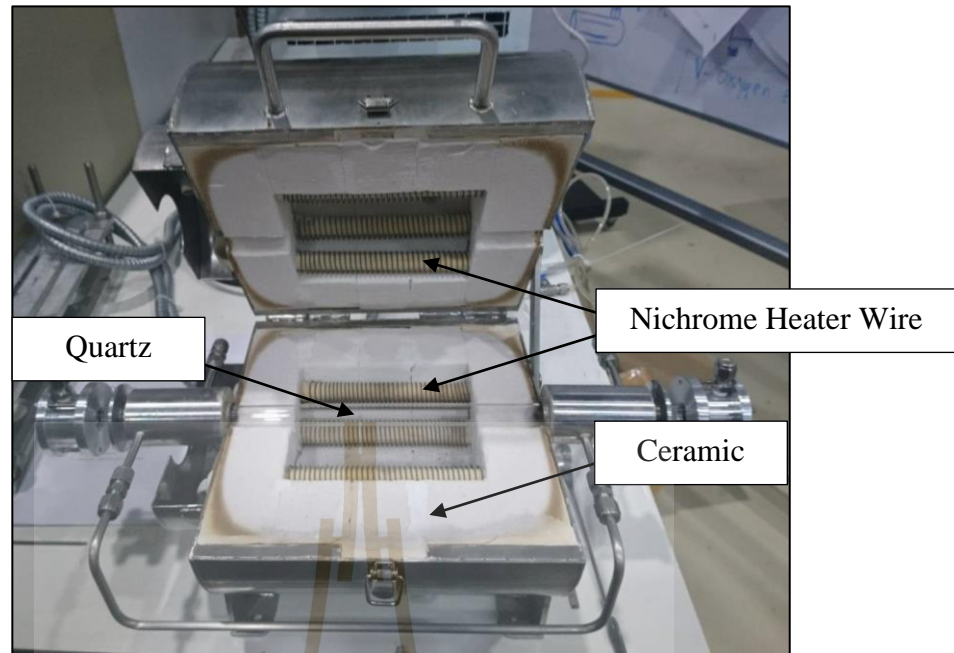


Figure 4.4 Nichrome resistance heating wire and ceramics insulator.

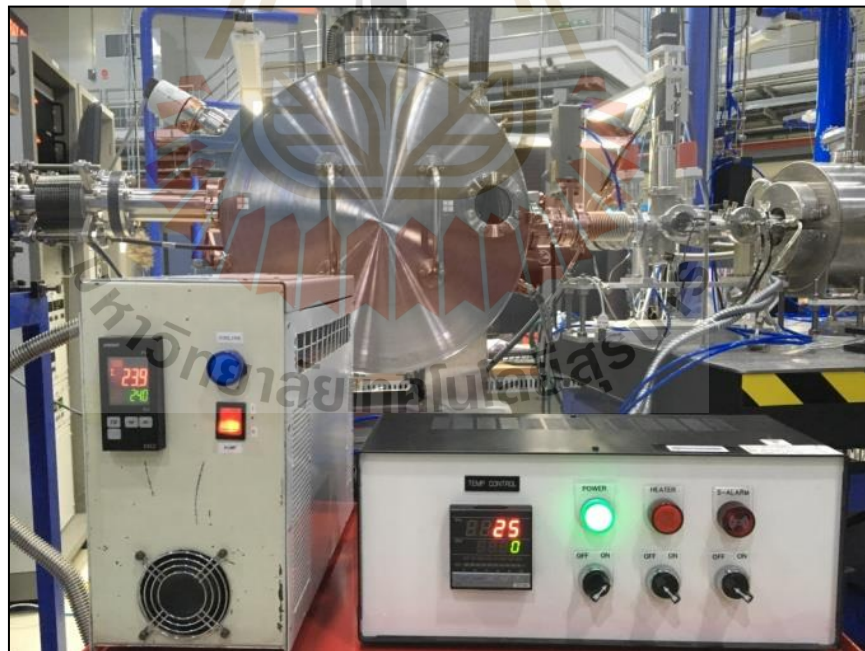


Figure 4.5 Temperature controller and Cooling systems.

Temperature Controllers are microprocessor-based program controllers which store a maximum of 16 patterns and are the ideal instrument for measuring temperature

and logging temperature data. It has an LED display with operating status indicators and a short-circuit alarm. It can supply power for the heater up to 1000°C with a power rate of 1.2kW, with the temperature increasing rate of 1°C/min. The maximum temperature can be obtained within 30 minutes. A type K thermocouple, also referred to as Chromel-Alumel, is used for this work due to the fact that it exhibits high accuracy, fast response, and wide temperature measurement range and, more importantly, is suitable for medium to high-temperature measurement applications.

4.3 Temperature testing of *in situ* heating cell

The most important issue for commissioning of the heating element of the cell is to ensure that the water cooling is sufficient and that the heat causes no harm to the overall XAS measurement system. Temperature checks were conducted at various heating cell positions While maintaining the temperature at 1000 °C for 3 hours. It is noted cooling fans were installed at various parts of the heating cell to remove the heat out from the system. The procedures for testing the heating cell may be summarized as the follows:

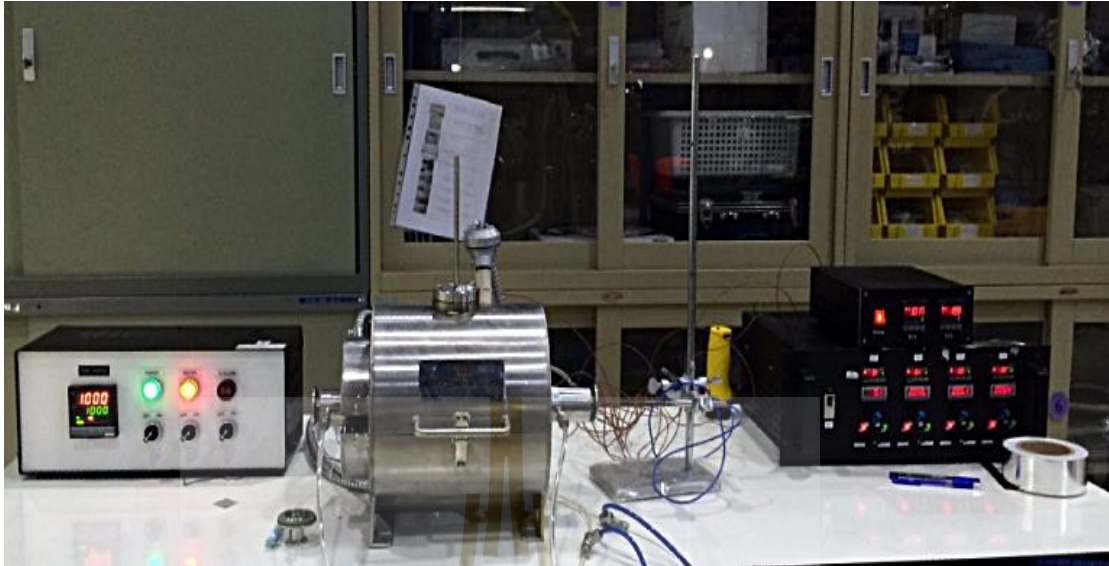


Figure 4.6 The thermocouples were placed at important positions of the *in situ* cell.

At the start, the temperature of the cell was at room temperature (25 °C). The controller was set to increase the temperature up to 1000 °C, which took 30 minutes. The sample was held at 1000 °C for 3 hours, and then the temperature of the sample was lowered to room temperature of 25 °C, as schematically shown as Figure 4.7.

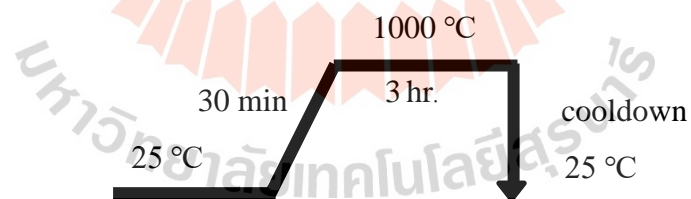


Figure 4.7 Schematic diagram showing temperature cycle of the *in situ* cell.



Figure 4.8 Set up for testing the in situ cell with cooling equipment installed.

During 3-hour maintaining the temperature of the sample at $1000\text{ }^{\circ}\text{C}$, the temperature at various positions of the furnace were recorded every 10 minutes for safety inspection. The data of the temperature at different positions, indicated in Figure 4.9, are plotted in Figure 4.10(a). The temperature at the entry port of the X-ray was found to be below $30\text{ }^{\circ}\text{C}$, and at the exit port of the X-ray is about $60\text{ }^{\circ}\text{C}$. This allows the in situ cell to be connected to the rest of photocurrent measurement chambers, I_0 and I_1 , without difficulties. It is noted that polypropylene (PP) windows are used at both the entry and exit port of the in situ cell. The temperature below $60\text{ }^{\circ}\text{C}$. Will cause no harm to the windows. There is a slight discrepancy of the temperature at the sample holder and at the display of the controller, about $10\text{ }^{\circ}\text{C}$. This difference may be caused by the position of the thermocouple providing the input signal to the controller.

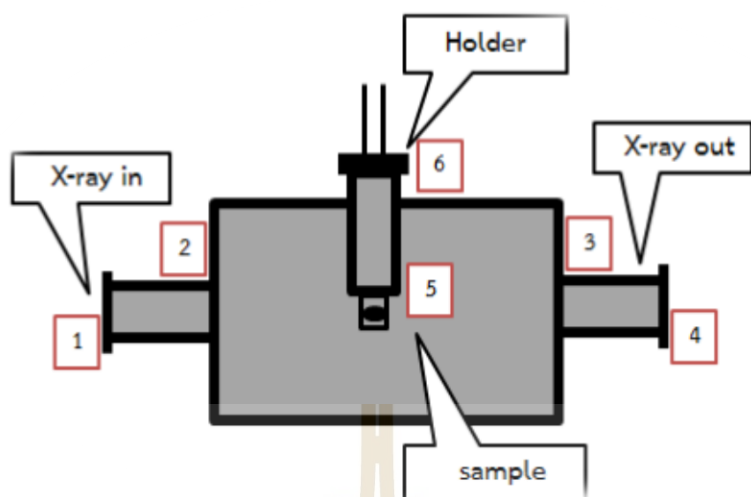


Figure 4.9 Temperature studies diagram for various parts of the heating cell.



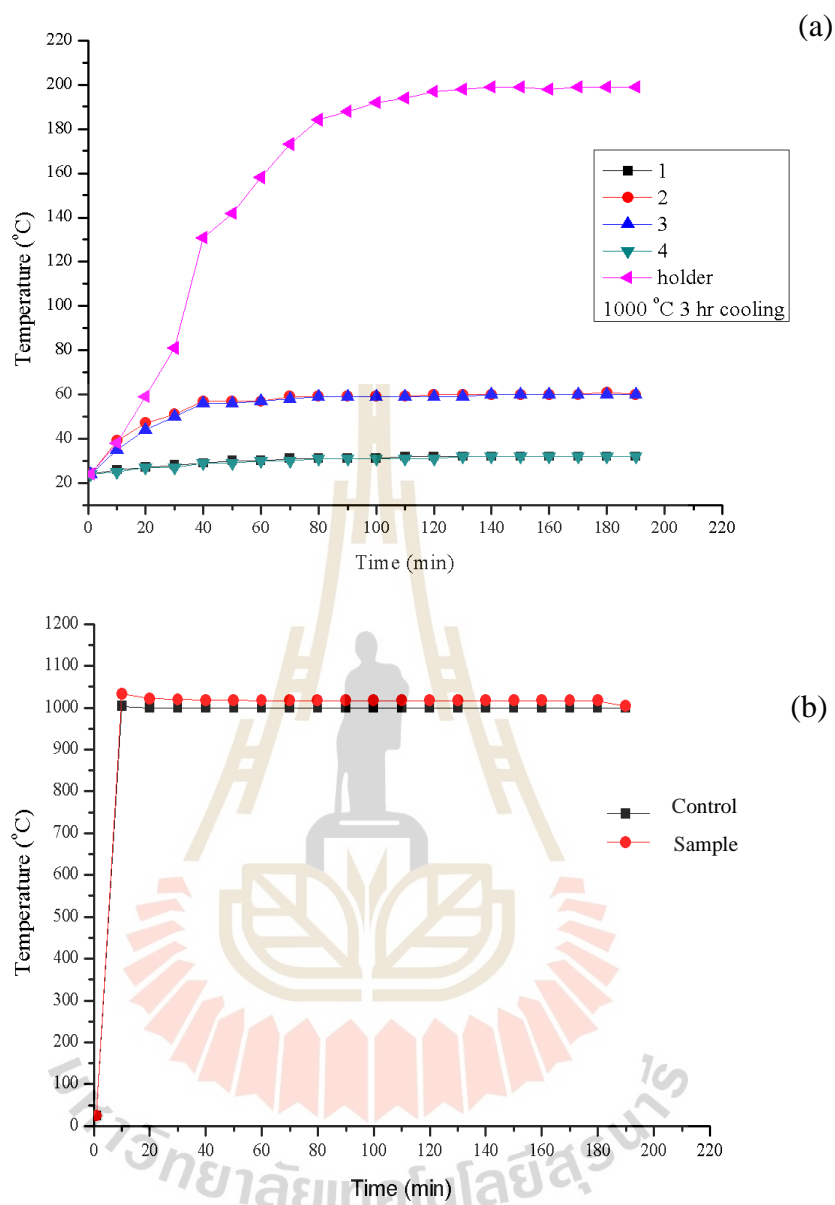


Figure 4.10 (a) The temperature at different positions of the heating cell (b) sample and control.

4.4 Installation of *in situ* heating cell at BL5.2 of SLRI

After verifying that the temperature at the entry- and exit-ports of the *in situ* heating cell was below 60 °C, connecting the cell into the existing XAS measurement

system can be done without concerning the heat that might cause the damage to the polypropylin windows. The alignment of the *in situ* cell can be done with ease. After connecting the cell in between the I_0 and I_1 chambers with polypropylin windows as vacuum isolation, the X-ray beam was checked with by using burning paper at the sample holder and the end of the system (the end flange). The *in situ* cell was successfully installed and tested at BL5.2 beamline at SLRI, as shown in Figure 4.11.



Figure 4.11 Photo of the *in situ* heating cell installed at the XAS station at BL5.2 beamline at SLRI.

4.5 References

An, P., Hong, C., Zhang, J., Xu, W., & Hu, T. (2014). A facile heating cell for *in situ* transmittance and fluorescence X-ray absorption spectroscopy investigations. **Journal of synchrotron radiation**, 21(1), 165-169.

CHAPTER V

RESULTS AND DISCUSSION

The *in situ* cell, developed in during the course of this work, was used for real-time XAS measurements at the BL5.2 at SLRI. FeO pellet and LiCoO₂ powder were the materials for these commissioning test. The temperature-dependent measurement XAS results (XANES and EXAFS spectra), as well as data analyses, are presented in this chapter.

5.1 *In situ* XAS study for temperature dependent of FeO

Iron (Fe) in iron compounds have different oxidation states, and thus different local structures. Thus, it is the element of choice for this temperature dependent XAS experiment. The XAS experiments of FeO were carried out at BL5.2 of SLRI to examine the local structure at temperatures ranging from room temperature to 1000 °C. During XAS measurements, the transitions of electrons from the K level (1s electrons) to allowed energy levels/bands near (below and above) the vacuum level were recorded. The spectra of the transitions were collected with scanning of X-ray photon energy around the K-edge and an energy step of 0.20 eV. The spectra provide the information of the absorption coefficient near the K-edge. This measurement technique is known as X-ray Absorption Near-Edge Structure (XANES) spectroscopic technique. Data reduction of the XANES spectra could be processed by the ATHENA software.

The normalized Fe K-edge XANES spectra of FeO pellet taken at different temperatures are shown in Figure 5.1. The XANES spectrum of Fe₂O₃ was also taken

and shown in the figure for comparison. The XANES spectra taken at room temperature to 400 °C show similar features with a gradual shift in the absorption edge towards higher photon energy. At 500, the changes in the features of the XANES spectrum above the absorption edge becomes obvious. The changes pattern leads to the features of the XANES spectra of FeO taken above 500 °C. These changes reflect the changes in the local structure around absorbing atoms.

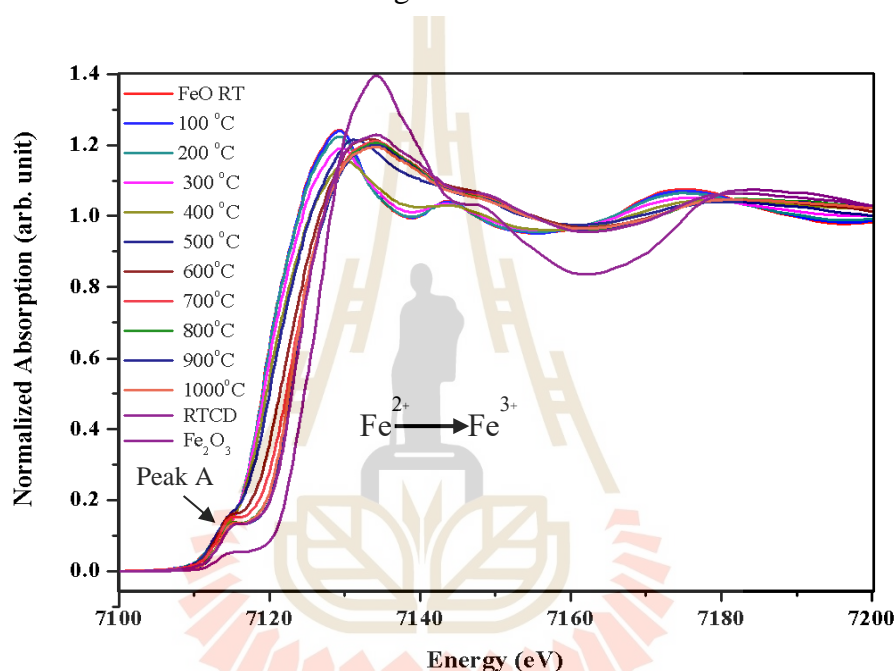


Figure 5.1 Normalized X-ray absorption Fe K-edge spectra of FeO pellet.

The shift of the absorption edge towards higher excitation energy, as shown in Figure 5.1, indicates the change in the oxidation state of the absorbing Fe atoms. This change in the *in situ* XANES of FeO in the Fe K-edge taken at room temperature to 1000 °C shows that the oxidation state of Fe increases 2+ to 3+ with temperature. It is noted that the XANES spectra are averaged over many absorbing Fe atoms. Thus, the gradual shift in the absorption edge is resulted from the gradual increase of Fe³⁺ with increasing temperature. Quantitative analysis of the valence states of Fe was performed

using the empirical edge-shift calculation making comparisons to a known standard samples (FeO and Fe₂O₃). The edge value was calculated from the maximum value of the first derivative of the edge region. The oxidation state of Fe in the sample is calculated from the following Equation. (5.1) (Boonlakhorn1 et al., 2014)

$$= \left[3 \times \frac{\Delta E \text{ of sample}}{\Delta E \text{ of Fe}^{2+} \text{ and Fe}^{3+}} \right] + \left[2 \times \left(1 - \frac{\Delta E \text{ of sample}}{\Delta E \text{ of Fe}^{2+} \text{ and Fe}^{3+}} \right) \right] \quad (5.1)$$

It is noted that ΔE of sample means a difference of edge value of samples compared with Fe²⁺ (FeO) standard. The calculated oxidation state of Fe at various temperatures are given in Table 1 and plotted in Figure 5.2. It is obvious that below 200 °C, only Fe²⁺ was observed. The oxidation state linearly increases to 2.65+ at 800°C and remains constant.

Table 5.1 The oxidation states for each temperature calculated by Equation (5.1).

Sample	Temperture °C	E_0 (eV)	oxidation state	
FeO	25	7119.19	2.00	
	25	7119.36	2.02	
	100	7119.36	2.02	
	200	7119.36	2.02	
	300	7120.01	2.12	
	400	7120.47	2.19	
	FeO + BN	500	7121.38	2.33
		600	7122.68	2.52
		700	7122.90	2.55
		800	7123.53	2.65
900		7123.53	2.65	
	1000	7123.54	2.65	
Fe ₂ O ₃	25	7125.92	3.00	

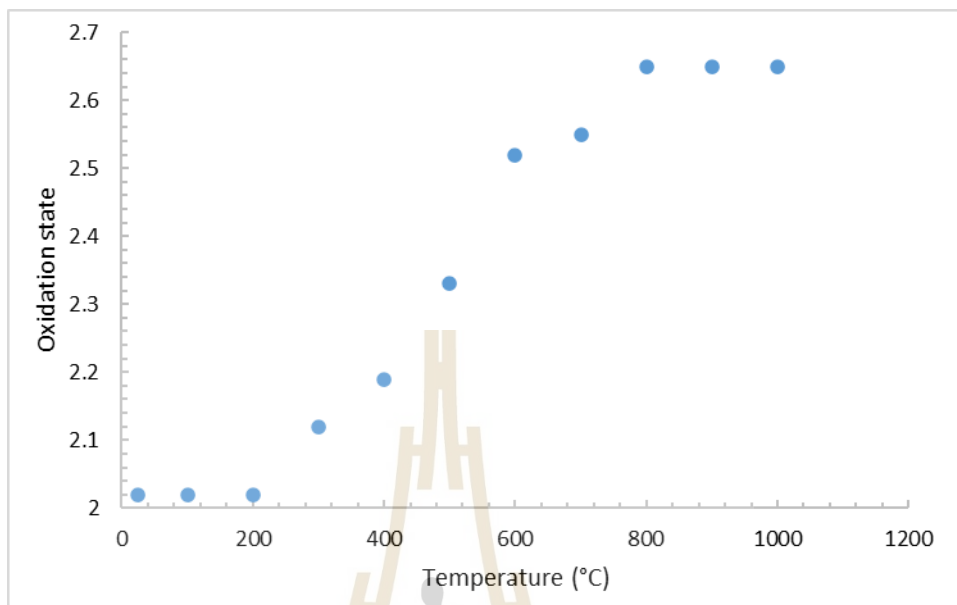


Figure 5.2 The oxidation number of the Fe K-edge has changed as a result of the calculation.

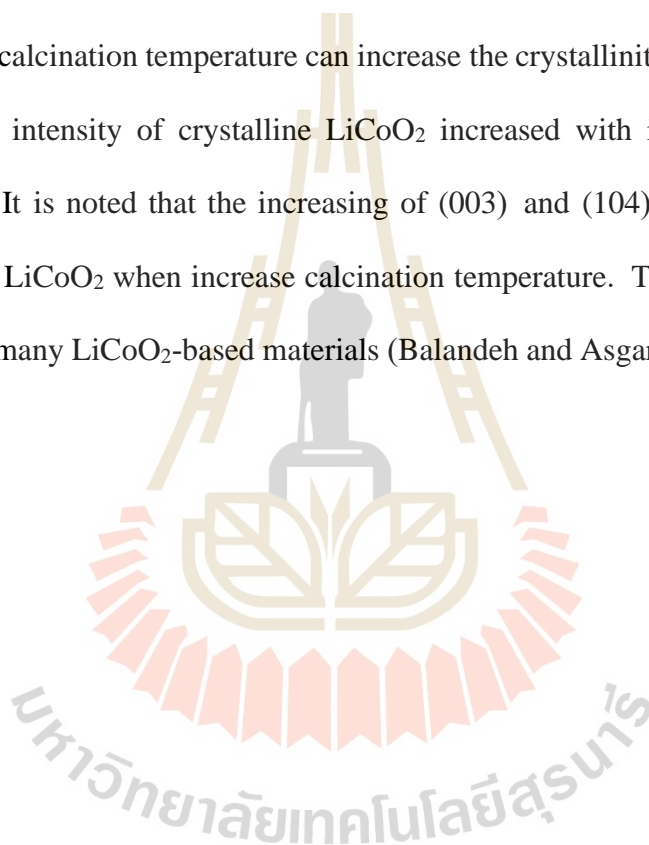
5.2 Study of phase information in lithium cobalt oxide

5.2.1 Structural and morphological characterizations

The crystal structure and phase evolution of LiCoO_2 were studied by using an X-ray diffractometer (XRD; Rigaku SmartLab) with Cu $K\alpha$ radiation ($\lambda = 1.5418 \text{ \AA}$). Room temperature XRD data were collected in the 2θ scan range of $20\text{--}60^\circ$ with step size of 0.02° and scanning rate of 2.5° per minute. Microstructural analyses of the samples were carried out by using the FEI-Quanta 450 SEM.

The XRD patterns of LiCoO_2 powders prepared by co-precipitation method before and after calcination at different temperatures are shown in Figure 5.3. The changes of peak patterns indicate that phase formation and highly crystalline of

powders were transformed by the different calcination temperature conditions. The XRD of all samples can be indexed to Rhombohedral phase LiCoO_2 (space group R-3m) and Orthorhombic phase KNO_3 phase (space group Pmcn) with database file of JCPDS card number 75-0532 and JCPDS card no. 00-005-0377, respectively. It indicates that the prepared powders are two-phase coexistence of LiCoO_2 and by-product KNO_3 , and no evidence detestable starting materials. Meanwhile, the increasing of calcination temperature can increase the crystallinity of LiCoO_2 . It can be seen that the intensity of crystalline LiCoO_2 increased with increasing calcination temperature. It is noted that the increasing of (003) and (104) peaks confirmed the increasing of LiCoO_2 when increase calcination temperature. This behavior has been observed for many LiCoO_2 -based materials (Balandeh and Asgari, 2010; Khatun et al., 2014)



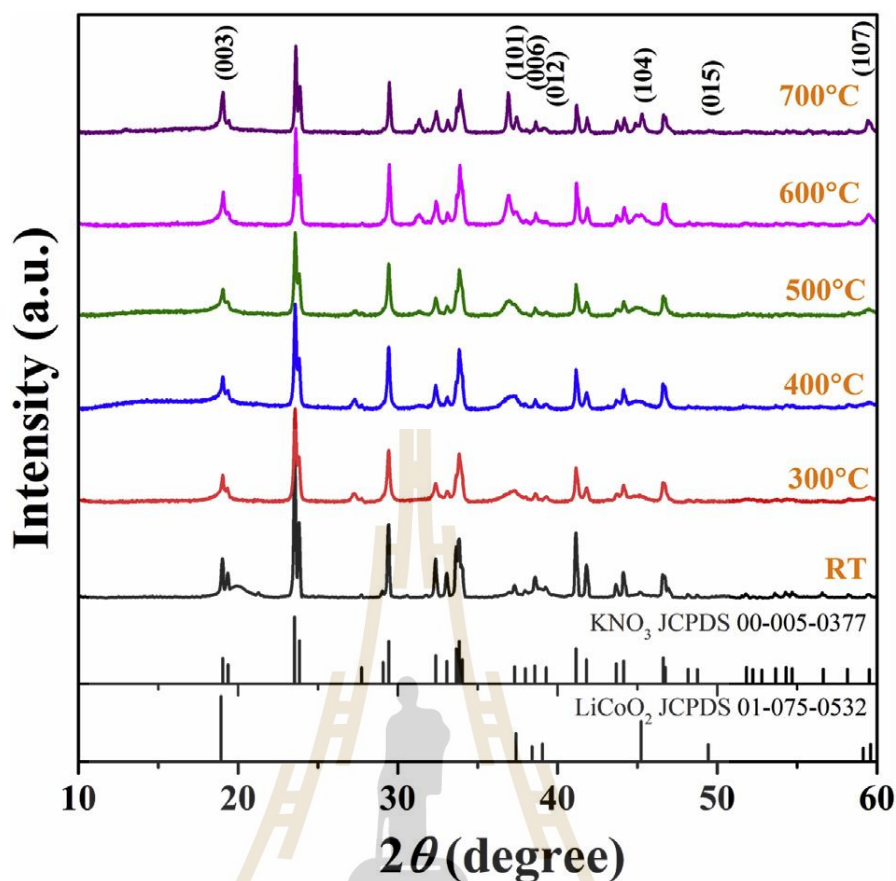


Figure 5.3 XRD patterns of LiCoO₂ powders with various calcination temperatures.

Error! Reference source not found. 4 shows scanning electron microscopy (SEM) and energy-dispersive X-ray (EDS) mapping images for the selected SEM region of produced powders with varied calcination temperatures to further investigate the surface morphology of the powders. All SEM images of the samples show a wide range of particle sizes. Furthermore, powders with lower calcination temperatures have spherical particles. Furthermore, the higher calcination temperature present slightly increase cubic-like shape. The EDS method, which is present in distinct colors dot in EDS mapping, was examined to explain the distribution of each element in the sample and the elemental compositional information. The existence of O, Co, and N elements in the acquired sample is confirmed by EDS elemental mapping pictures, demonstrating

that element atoms were equally distributed. However, because Li is a small atomic number element, the EDS method could not detect it.

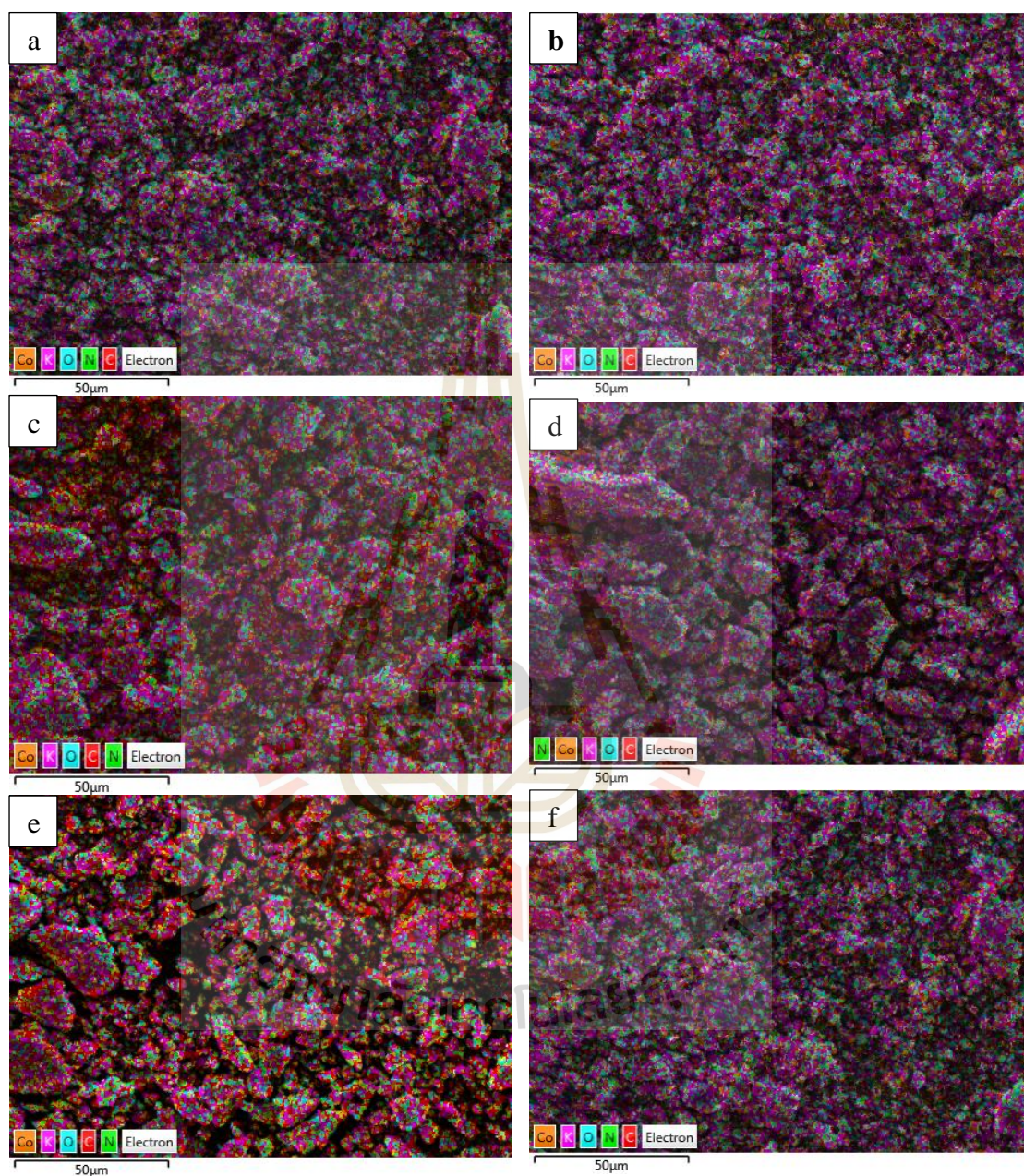


Figure 5.4 SEM images of LiCoO₂ samples calcined at various calcination temperatures; (a) RT, (b) 300 °C, (c) 400 °C, (d) 500 °C, (e) 600 °C and (f) 700 °C.

5.2.2 XANES studies of phase transition

Synchrotron-based XANES and EXAFS spectra were conducted at the SUT-NANOTEC-SLRI XAS Beamline (BL5.2) at the Synchrotron Light Research Institute (Public Organization), Thailand (Kidkhunthod, 2017; Klysubun et al. , 2017). The *in situ* experiment XAS, which included *in situ* XANES and EXAFS spectra at Co K-edge spectra, was collected in transmission modes to describe the valence states and local structural information of Co atoms. Using reference Co metal spectra, the cobalt K-edge absorption measurements were calibrated and aligned, with the maximum value of the first derivative set at 7709 eV. The temperature-dependent XAS experiment was carried out with an optimized pellet form of sample and an in-house heating cell. Furthermore, Figure 5.5 shows XAS in-house heating cells and supported gas systems, as well as a schematic representation of a temperature-dependent XAS research. Synthesized powders were reduced to fine powders and pressed into pellets before the experiment in measuring XAS spectra.

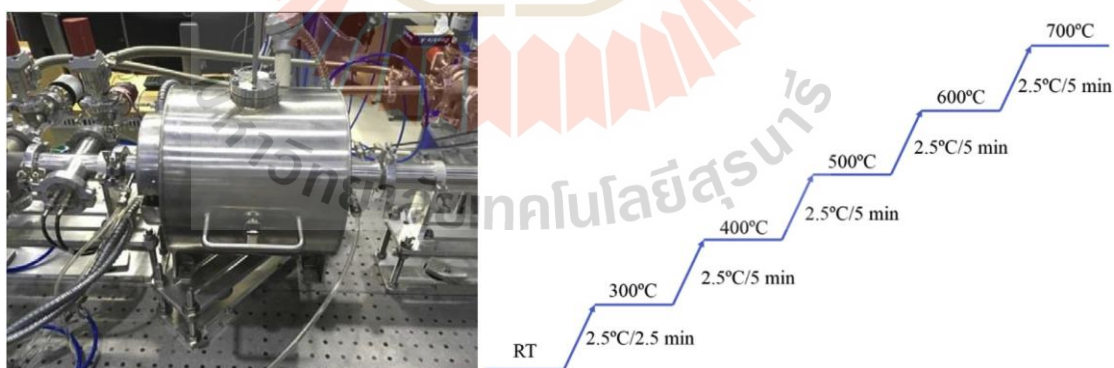


Figure 5.5 *In situ* XAS in-house heating cells for transmission mode and Schematic diagram of *in situ* XAS measurement.

Although LiCoO_2 powders contain a KNO_3 phase, the *in situ* XAS method may be utilized to examine the electronic structure and local structure surrounding Co atoms utilizing a majority LiCoO_2 phase. Figure 5.6 shows normalized XANES spectra at the Co K-edge LiCoO_2 samples at several temperatures: (a) RT, (b) 300 °C, (c) 400 °C, (d) 500 °C, (e) 600 °C, (f) 700 °C, CoO (Co^{2+}) and Co_2O_3 (Co^{3+}) standard samples. The energy required to eject a core electron from a cobalt atom is 7709 eV, which is the characteristic absorption edge of Co. The most intense peak A near 7730 eV arises from the electronic transition $1s \rightarrow 4p$. The magnified inset around 7710 eV (peak B) comes from the $1s \rightarrow 3d$ transition which shows a systematic decrease and small shifting to lower energy during rising temperature. This behavior is similar to previous observe by Patridge (Patridge et al., 2013). Moreover, this is consistent with a changing in Co oxidation from higher Co^{3+} to Co^{2+} .

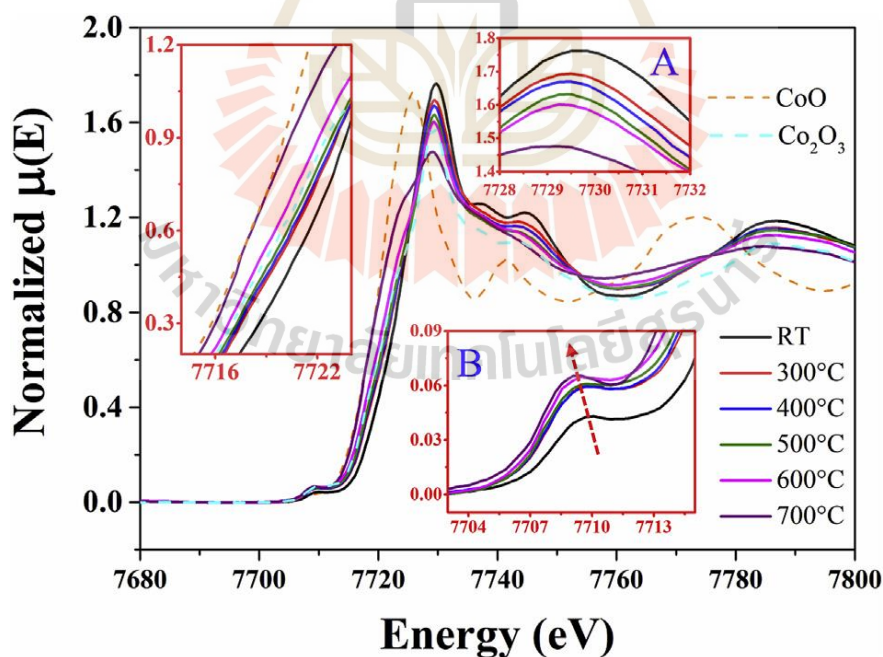
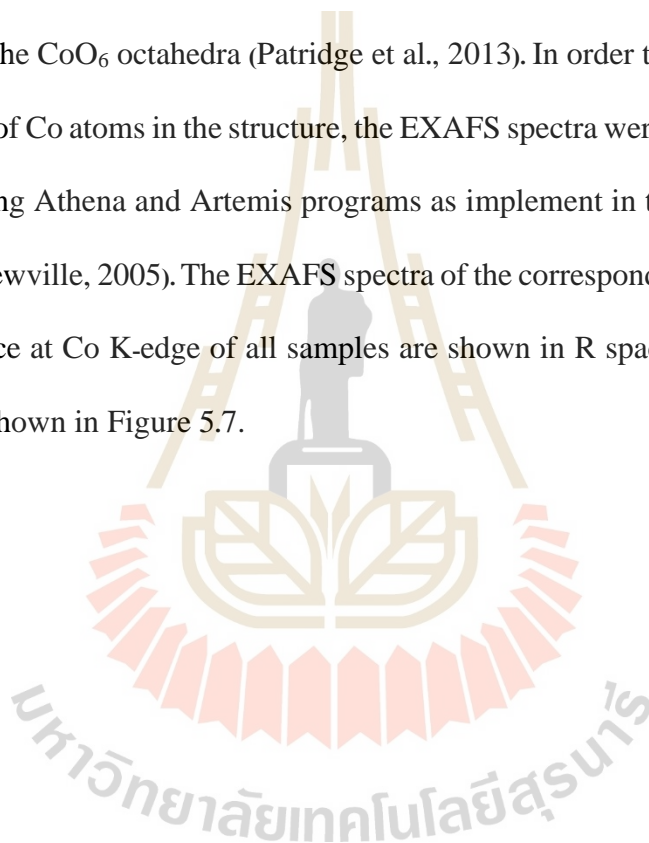


Figure 5.6 *In situ* XANES spectra of Co K edge of LiCoO_2 samples and standard samples.

5.2.3 EXAFS studies of phase transition

As seen in Figure 5.6, a shoulder around 7725 eV is observed only for calcination at 700 °C. This suggests a significant change in Co local structure especially for coordinated oxygen atoms surrounding Co atom. This will be discussed in EXAFS section. In more detail, from RT to 700 °C, the decreased intensity of normalized absorbance is clearly observed indicating more orbital mixing and more increase in distortion of the CoO₆ octahedra (Patridge et al., 2013). In order to understand the local environment of Co atoms in the structure, the EXAFS spectra were intensively analyzed and fitted using Athena and Artemis programs as implement in the IFEFFIT packages (Ravel and Newville, 2005). The EXAFS spectra of the corresponding Fourier transform (FT) in R space at Co K-edge of all samples are shown in R space at Co K-edge of all samples are shown in Figure 5.7.



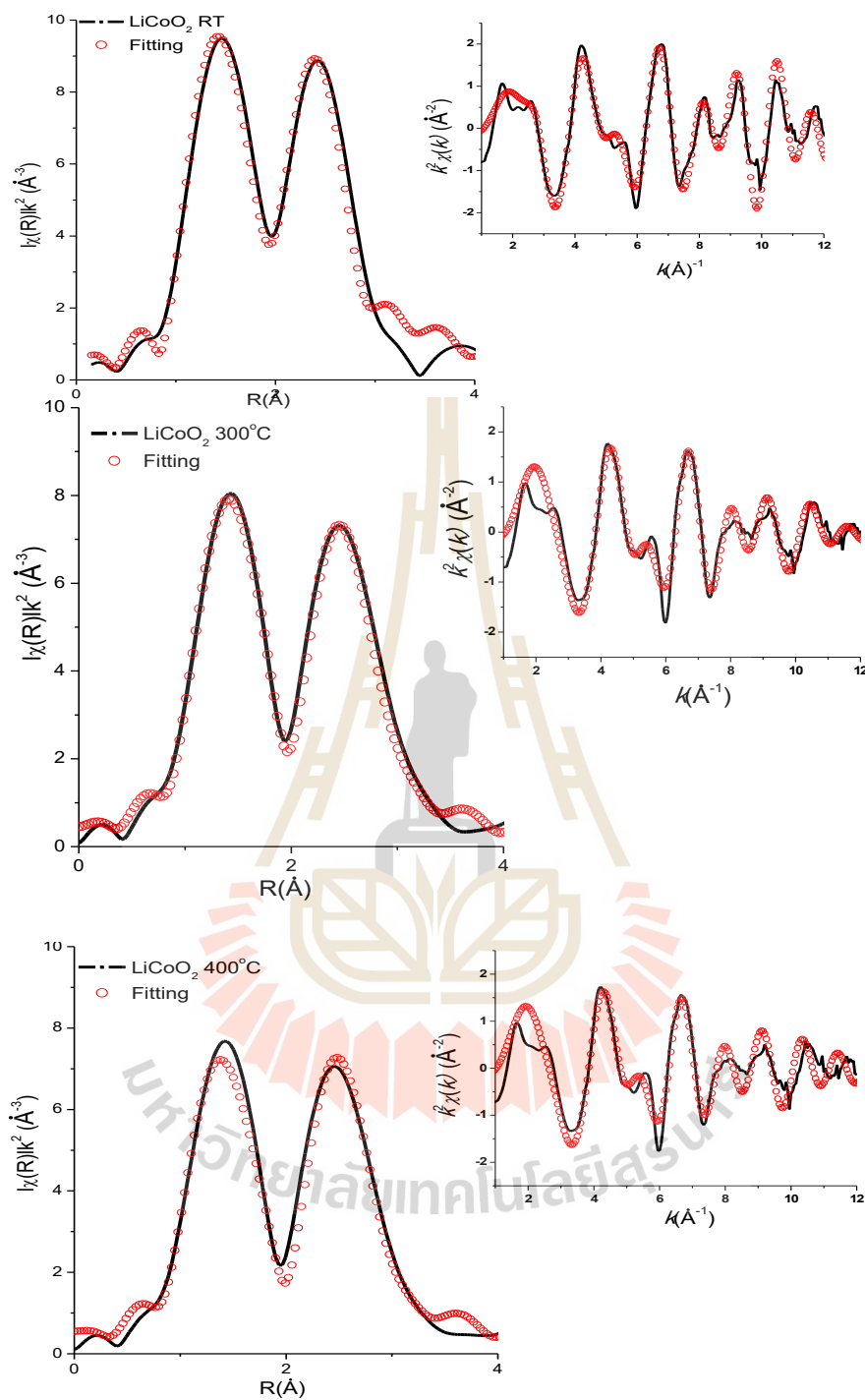


Figure 5.7 Fourier transform at *in situ* EXAFS spectra at Co K-edge EXAFS (weighted by k^2) from experiment (black line) and fitting (red circle) of LiCoO_2 at different temperature. Model fits to the experimental filtered EXAFS in the k -space are also shown (insets). Experimental filtered EXAFS in the k -space is also shown (insets).

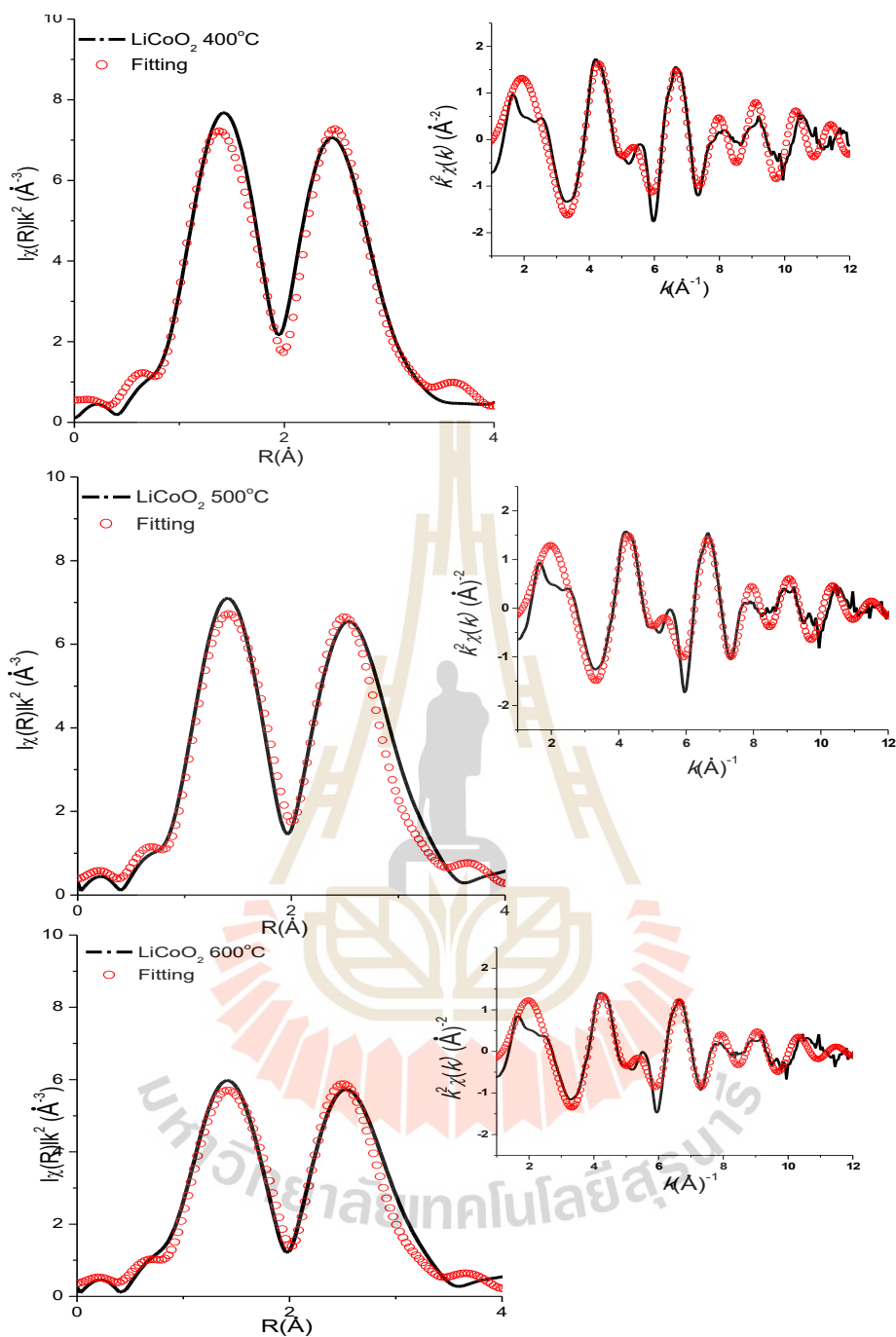


Figure 5.7 Fourier transform at *in situ* EXAFS spectra at Co K-edge EXAFS

(weighted by k^2) from experiment (black line) and fitting (red circle) of LiCoO_2 at different temperature. Model fits to the experimental filtered EXAFS in the k -space are also shown (insets). Experimental filtered EXAFS in the k -space is also shown (insets). (Continued).

It can be seen that the amplitude of Co–O and Co–Co peaks remain almost the same. These patterns can be observed with other systems of Li_xCoO_2 and Li_xNiO_2 (Deb et al., 2007; Rumbler et al., 2010). In addition, FT fitting was used to explore structural characteristics of the immediate environment around the Co atom. Co K-edge k^2 -weighted plots inset Figure 5.7 shows Fourier transform fitting from experiment (black line) and fitting (red line) at various calcination temperatures of LiCoO_2 . In the LiCoO_2 system, The FT provides information on the partial atomic distribution around the Co atoms. The initial scattering contributions from the nearest neighbor O atoms at a distance of approximately 1.92 and the next nearest neighbor Co atoms at a distance of about 2.8. Due to the negligible scattering factor of lithium in comparison to Co, the contribution of the Co–Li distance is barely noticeable. Multiple scattering contributions are responsible for the peaks at longer distances. This implies the local environments around Cobalt atoms are almost identical. The Co–O and Co–Co models were used for the fit. The best parameters of the EXAFS fitting such as interatomic distances (R), Debye Waller factors (σ^2), amplitude reduction (S_0^2) and R-factor were shown Table . In this study, in order to study the influence of temperature to Co local structure in term of Debye–Waller factors (σ^2), the amplitude reduction (S_0^2) is set to be equally 0.75 for all temperatures. Moreover, the mean coordination numbers were obtained to be between 4.8(1) and 5.7(2) for both Co–O and Co–Co, respectively.

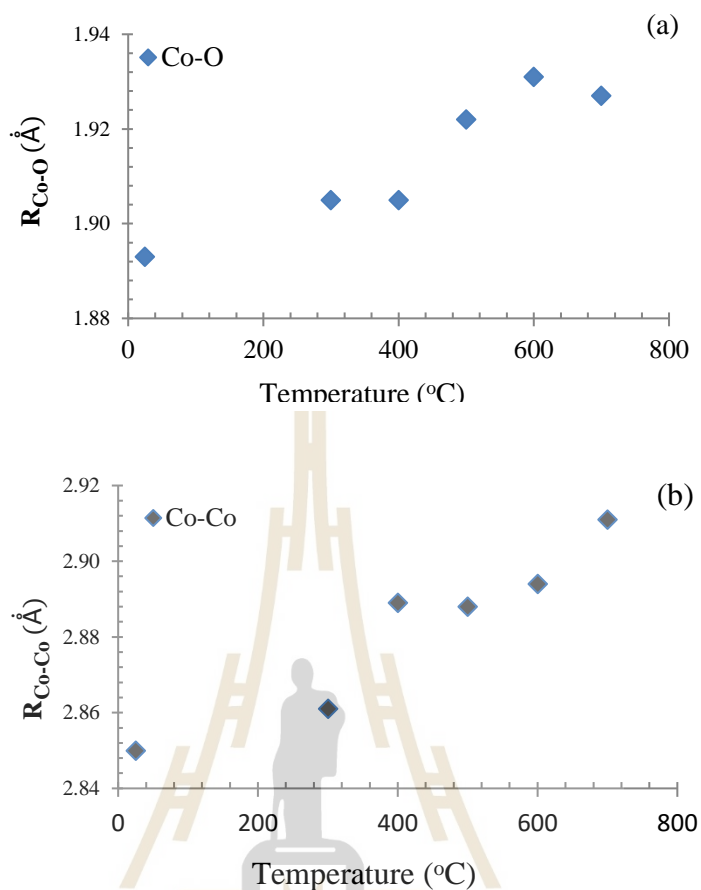


Figure 5.8 The local neighboring Co–O (a) and Co–Co (b) distances in LiCoO₂ structure as a function of temperature.

As can be observed in Table 2, increased temperature leads to an increase in Debye–Waller factors (approximately of 10 percent relative error). This implies and confirms the XANES findings of greater structural deformation around Co atoms in LiCoO₂. More specifically, as shown in Figure 5.8 (less than ± 0.01 of error distance value), local bond lengths of Co-neighboring atoms obtained by Co K-edge EXAFS fitting may be interpreted as a function of temperature. The higher temperature, the larger Co–O/Co–Co bonding distances.

Table 5.2 EXAFS fitting parameters including interatomic distances (R), coordination numbers (N), Debye–Waller factors (σ) and amplitude reduction (S_0^2).

Sample	Shell	σ^2	R(Å)	R-factor	S_0^2
LiCoO ₂ 25 °C	Co-O	0.00030	1.893(2)	1.10%	0.605
	Co-Co	0.00201	2.850(1)		
LiCoO ₂ 300 °C	Co-O	0.06330	1.905(1)	2.18%	0.828
	Co-Co	0.07360	2.861(1)		
LiCoO ₂ 400 °C	Co-O	0.00855	1.905(1)	3.27%	0.895
	Co-Co	0.00855	2.889(2)		
LiCoO ₂ 500 °C	Co-O	0.00824	1.922(1)	3.79%	0.815
	Co-Co	0.00764	2.888(1)		
LiCoO ₂ 600 °C	Co-O	0.00989	1.931(2)	2.96%	0.782
	Co-Co	0.00858	2.894(1)		
LiCoO ₂ 700 °C	Co-O	0.01304	1.927(1)	1.76%	0.602
	Co-Co	0.00192	2.911(1)		

5.3 Study of phase information in cobalt ferrite

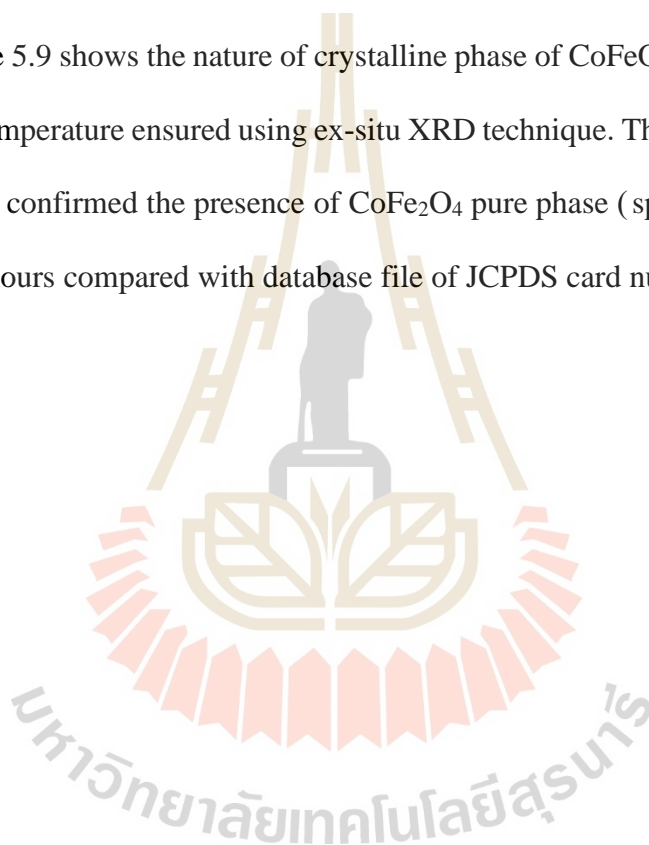
The phase formation behaviour was investigated in details by X-ray diffraction (XRD). Reduction and oxidation processes were investigated using X-ray absorption near edge structure (XANES). A change in local structure was investigated using *in situ* extended X-ray absorption fine structure (*in situ* EXAFS). The temperature in the range of 25 °C to 800 °C has been investigated local structure of *in situ* EXAFS system.

Synchrotron-based XANES and EXAFS spectra were conducted at the SUT-NANOTECH-SLRI XAS Beamline (BL5.2) at the Synchrotron Light Research Institute (Public Organization), Thailand (Kidkhunthod., 2017; Klysubun et al., 2017).

5.3.1 X ray diffraction results

The crystal structure and phase evolution of the powders were characterized using an X-ray diffractometer (XRD; Rigaku SmartLab) obtained by using Cu K α radiation with $\lambda = 1.5418 \text{ \AA}$. Room temperature XRD data was collected in the 2θ scan range of $20\text{--}80^\circ$ with step size of 0.02° and scanning rate of 2.5° per minute. The Microstructural observation was performed by using SEM (FEI-Quanta 450).

Figure 5.9 shows the nature of crystalline phase of CoFeO₄ powders at different calcination temperature ensured using ex-situ XRD technique. The XRD patterns of the samples were confirmed the presence of CoFe₂O₄ pure phase (space group Fd-3m) at 800°C for 6 hours compared with database file of JCPDS card number 022-1086.



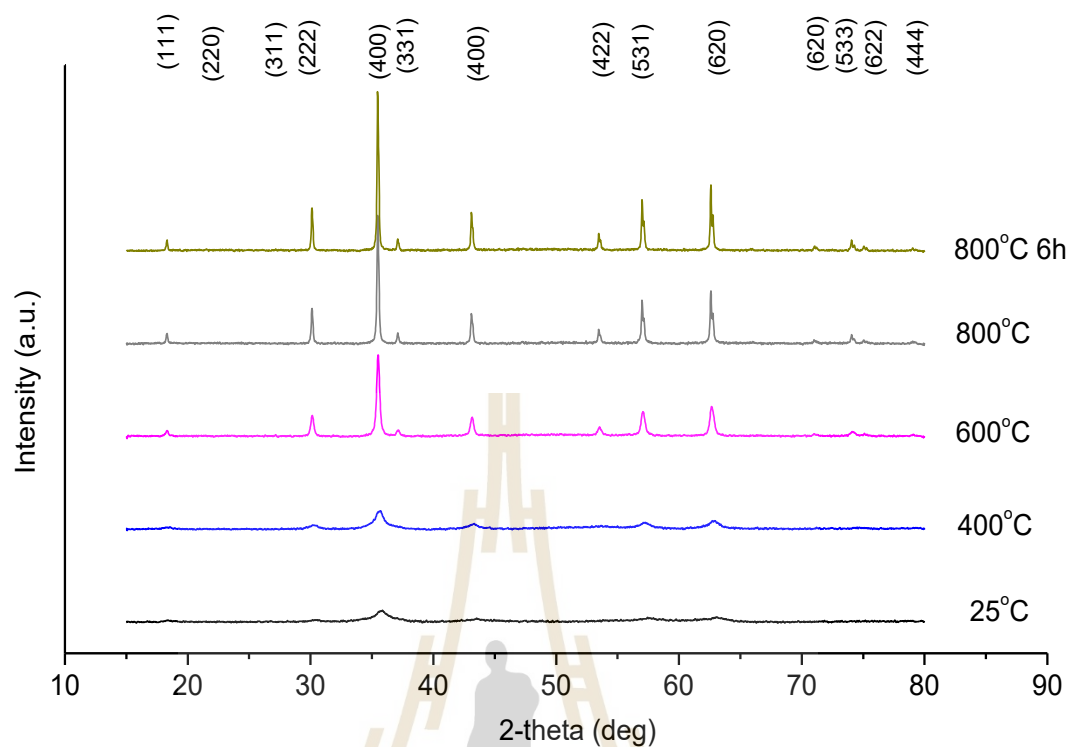


Figure 5.9 XRD patterns of CoFe_2O_4 powders with various calcination temperatures.

5.3.2 XANES results

By measuring the excitation of electrons K -edge to unoccupied bound states, XANES is used to gather information on the local arrangement of atoms around the absorbing atoms and the density of states of unoccupied states.

To characterize the valence states and local structural information of Co atoms, the *in situ* experiment XAS including *in situ* XANES and EXAFS spectra at Co and Fe K -edge spectra were collected in the transmission modes. Co and Fe K -edge absorption data were all calibrated and aligned using reference Co and Fe metals spectra with the maximum value of the first derivative set to 7709 eV and 7112 eV, respectively. The temperature dependent XAS experiment was performed following a schematic diagram as in Figure 5.10.

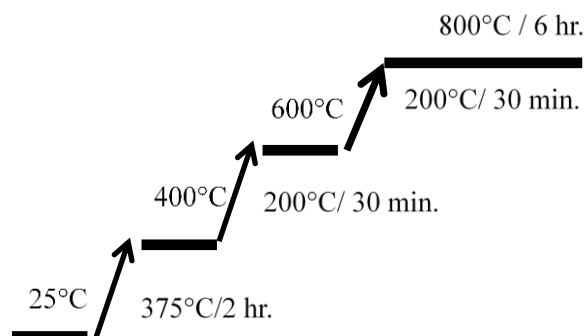


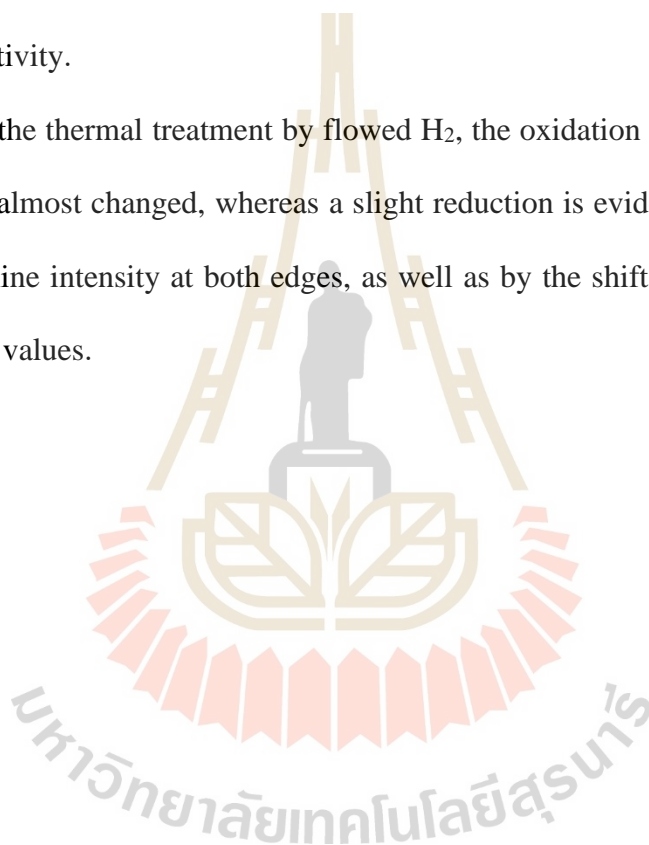
Figure 5.10 Schematic diagrams for measure *in situ* XAS. during the annealing treatment in H_2 .

The oxidation state and site occupancy of the metal species in the spinel structure were determined by XAS (Carta, 2009; Krishnan, 2007; Nilsen, 2007). In transition metals *K*- edges, XANES transitions involve the excitation of a 1s photoelectron into a mainly 4p derived continuum of states. In general, when the valence of the absorbing metal atom is increased a shift of the absorption edge toward higher energy is observed. XANES spectra for the Co-Fe spinels are shown as Figure 5.11 *in situ* XANES spectra of Fe *K*-edge (a) and Co *K*-edge (b).

Comparing the energy position of the absorption edge in the XANES spectra with that of the reference samples, it is possible to determine with great accuracy the oxidation state of each element in the spinel structure. In $CoFe_2O_4$, the oxidation state of Fe and Co is close to +3 and +2, respectively. Moreover, the fine structure of the pre-edge can provide further information about the structure of spinels. At *K*-edges in fact, pre-edge peaks, which correspond to $1s \rightarrow 3d$ transitions (with 3d-4p mixing), may occur at about 15-20 eV before the white line. An increase of the intensity of these features corresponds to the removal of the inversion symmetry in the environment of

the absorbing atom. Therefore, the pre-edge feature can provide a direct indication whether a metal center is located in a tetrahedral or octahedral site. At the Fe K-edge, the pre-edge peak intensity of ferrite is higher than that of cobaltite, indicating that the ferrite contains a higher amount of tetrahedrally coordinated Fe ions. The cation distribution was determined by EXAFS data of the starting materials. XAS spectra acquired during the following reduction confirm that the spinels exhibit a rather different reactivity.

After the thermal treatment by flowed H_2 , the oxidation states of Fe and Co in $CoFe_2O_4$ are almost changed, whereas a slight reduction is evidenced by the decrease of the white line intensity at both edges, as well as by the shift of Fe K-edge energy toward lower values.



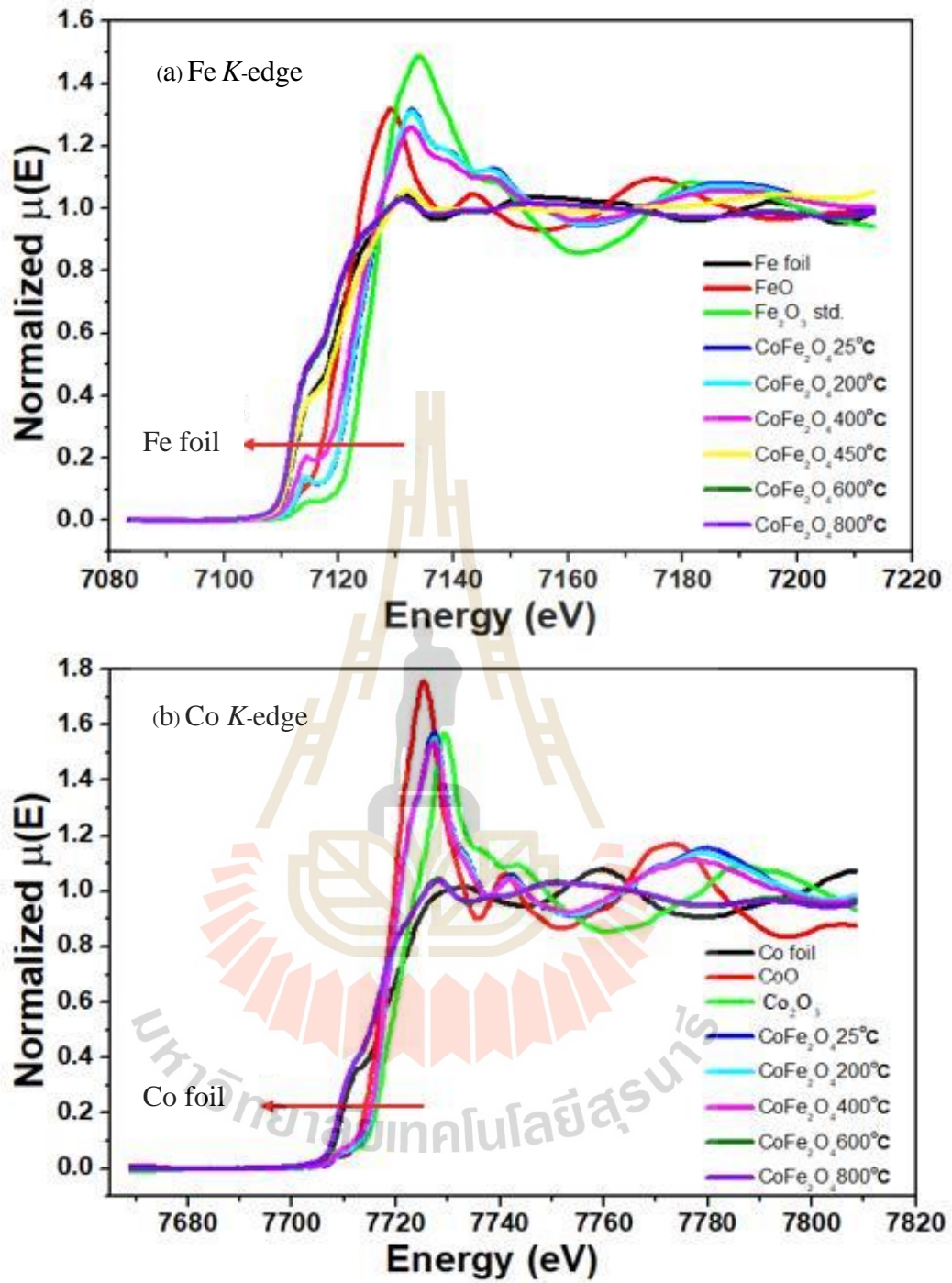


Figure 5.11 *in situ* XANES spectra of Fe K-edge (a) and Co K-edge (b).

5.3.3 EXAFS results

The Fourier transform show the phase transition corresponding with XANES results at room temperature to 800 °C, as shown in Figure 5.11. To process and enhance the EXAFS with the high k region, the plot $k^2\chi(k)$ is considered and windowed using a Hanning window $W(k)$. The EXAFS spectra were processed, information on local structure of Fe and Co atom. In this work, the Fe *K* edge EXAFS spectra can be obtained up to photon energy of 11k eV above the absorption edge, due to the presence of Co *K*-edge. Therefore, the range of Fourier transform of k space was limited to about $k = 7.0$. The Fourier transform in R space showed that the features change suddenly around 500 °C.

In situ XAS spectra of Fe *K* edge and Co *K* edge acquired during the following reduction shown as Figure 5.12 the oxidation state of Fe reduced to Fe metal about 500°C, similarly the Co *K*-edge that the oxidation state of Co reduced to Co metal. After the first reduction cycle in H₂, CoFe₂O₄ is almost completely reduced: both the Fe and Co *K*-edges XANES, and the corresponding EXAFS (Figure 5.12) data confirm the formation of metal phases. The peak corresponding to M-O bonds disappears, whereas that corresponding to M-M in the metal phase appears. This phase, however, has only a transient existence due to the fast reduction to the metal phase. The formation of metal Fe and Co starts as soon as some mixed wüstite phase is formed. FT data confirm the formation of metal phases at 600 °C of Fe *K* edge and Co *K* edge at 500 °C.

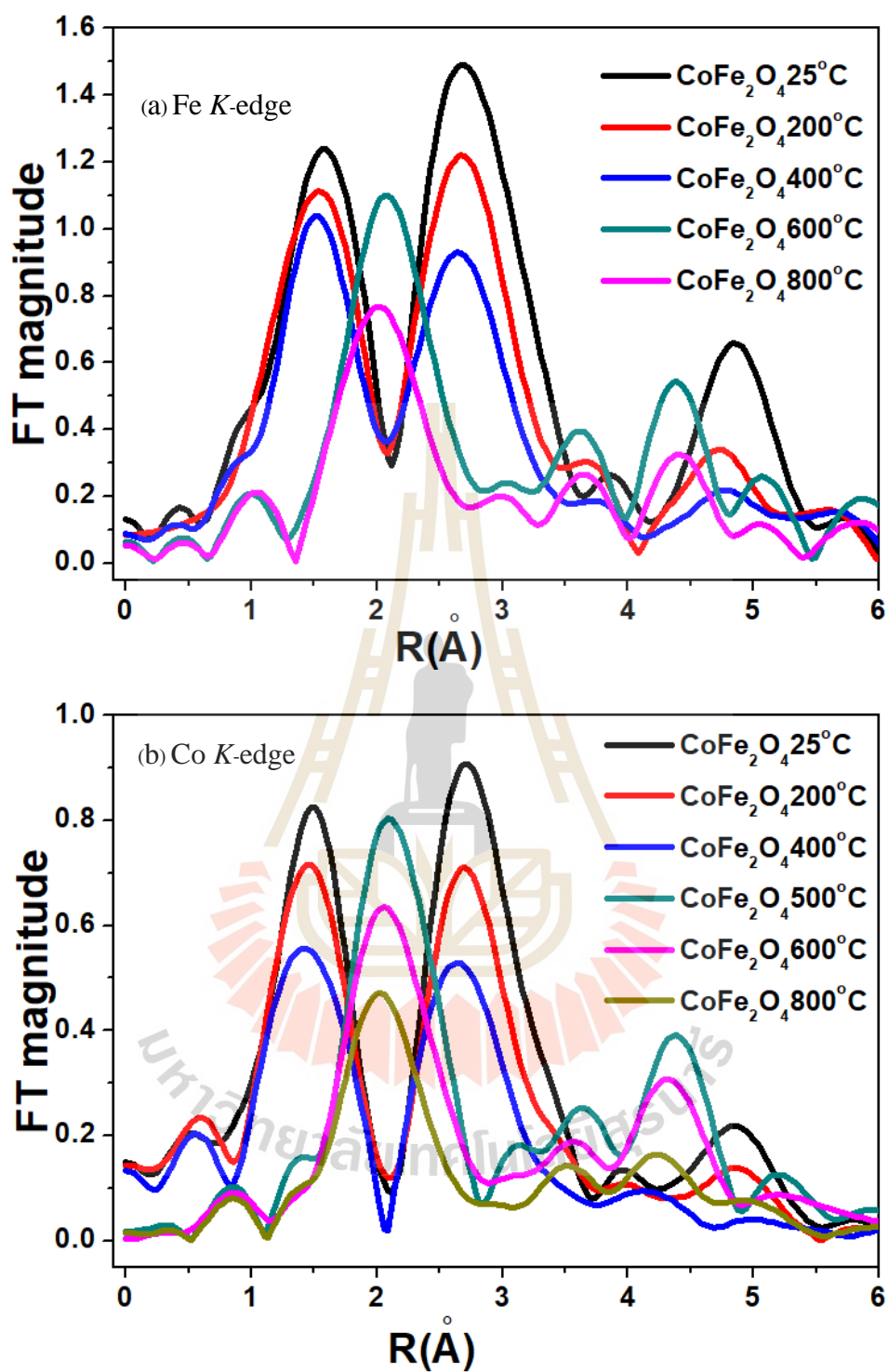


Figure 5.12 Fourier transforms of $k^2\chi(k)$ at probing (a) Fe atom and (b) Co atom.

5.4 References

- Balandeh, M. and Asgari, S. (2010). Synthesis and characterization of LiNiO_2 nanopowder with various chelating agents. **Journal of Nanomaterials**. 695083.
- Boonlakhorn, J., Kidkhunthod, P., Putasaeng, B., Yamwong, T., Thongbai, P. and Maensiri, S. (2015). Giant dielectric behavior and electrical properties of $\text{Ca}_{1-3x/2}\text{Lu}_x\text{Cu}_3\text{Ti}_4\text{O}$ ceramics. **Applied Physics A**. 120(1): 89–95.
- Carta, D., Casula, M. F., Falqui, A., Loche, D., Mountjoy, G., Sangregorio, C. and Corrias, A. (2009). A structural and magnetic investigation of the inversion degree in ferrite nanocrystals MFe_2O_4 (M= Mn, Co, Ni). **The Journal of Physical Chemistry C**. 113(20): 8606-8615.
- Deb, A., Bergmann, U., Bergmann, U., Cramer, S. P. and Cairns, E. J. (2007). In situ X-ray absorption spectroscopic study of $\text{Li}_{1.05}\text{Ni}_{0.35}\text{Co}_{0.25}\text{Mn}_{0.4}\text{O}_2$ Cathode Material Coated with LiCoO_2 . **Journal of the Electrochem. Society**. 154(6): A534–A541.
- Khatun, F., Gafur, M. A., Ali, M. S., Islam, M. S. and Serker, M. A. R. (2014). Impact of lithium composition on structural, electronic and optical properties of lithium cobaltite prepared by solid-state reaction. **Journal of Scientific Research**. 6(2): 217–231.
- Kidkhunthod, P. (2017). Structural studies of advanced functional materials by synchrotron-based X-ray absorption spectroscopy: BL5.2 at SLRI, Thailand. **Adv. Nat. Sci. Nanosci. Nanotechnology**. 8(3): 035007.
- Klysubun, W., Kidkhunthod, P., Tarawarakarn, P., Sombunchoo, P., Kongmark, C., Limpijumngong, S., Rujirawat, S., Yimnirun, R., Tumcharern, G. and

- Faungnawakij, K. (2017). SUT- NANOTEC- SLRI beamline for X- ray absorption spectroscopy. **Journal of Synchrotron Radiation**. 24: 707–716.
- Krishnan, V., Selvan, R. K., Augustin, C. O., Gedanken, A. and Bertagnolli, H. (2007). EXAFS and XANES investigations of CuFe_2O_4 nanoparticles and $\text{CuFe}_2\text{O}_4\text{-MO}_2$ (M= Sn, Ce) nanocomposites. **The Journal of Physical Chemistry C**. 111(45): 16724-16733.
- Nilsen, M. H., Nordhei, C., Ramstad, A. L., Nicholson, D. G., Poliakoff, M. and Cabañas, A. (2007). XAS (XANES and EXAFS) investigations of nanoparticulate ferrites synthesized continuously in near critical and supercritical water. **The Journal of Physical Chemistry C**. 111(17): 6252-6262.
- Ravel, B. And Newville, M. (2005a). ATHENA, ARTEMIS, HEPHAESTUS: data analysis for X- ray absorption spectroscopy using IFEFFIT. **Journal of Synchrotron Radiation**. 12(4): 537–541.
- Ravel, B. and Newville, M. (2005b). ATHENA and ARTEMIS: interactive graphical data analysis using IFEFFIT. **Physica Scripta**. 115(22): 1007–1010.
- Rumble, C., Conry, T. E., Doeff, M., Cairns, E. J., Penner-Hahn, J. E., Deb, A. (2010). Structural and electrochemical investigation of $\text{Li}(\text{Ni}_{0.4}\text{Co}_{0.15}\text{Al}_{0.05}\text{Mn}_{0.4}\text{O}_2)$ cathode. Material. **Journal of the Electrochem. Society**. 157(12): A1317–A1322.

CHAPTER VI

CONCLUSIONS AND SUGGESTION

In this work, the *in situ* cell was developed for XAS station at BL5.2 beamline at SLRI measurements in a transmission mode of measurement. The *in situ* cell allows the samples for XAS measurements to be in an ambient atmosphere. The *in situ* cell was designed for XAS measurements of samples heated up to 1000 °C under an inert atmosphere or special gas of interest (H₂, N₂ and O₂) which flow rate range from 1 to 100 ml/min. A nichrome resistance heating wire was selected for the heating element of the *in situ* cell. A type K thermocouple, also referred to as Chromel-Alumel, is used for this work. The temperature can be controlled to be a linear or step changes patterns. The temperature at the entry- and exit-ports of the *in situ* heating cell was below 60 °C, connecting the cell into the existing XAS measurement system can be done without concerning the heat that might cause the damage to the polypropylin windows. The alignment of the *in situ* cell can be done by connecting the cell in between the I_0 and I_1 chambers with polypropylin windows as vacuum isolation. The X-ray beam was checked by using burning paper at the sample holder and the end flange. The *in situ* cell was successfully installed and tested at BL5.2 beamline at SLRI. The cell was successfully tested for XAS measurements for determining the local structure of the absorbing atoms.

In the commissioning tests of the temperature-dependent XAS experiments using the home-made *in situ* cell, FeO was chosen due to its variation in oxidation states

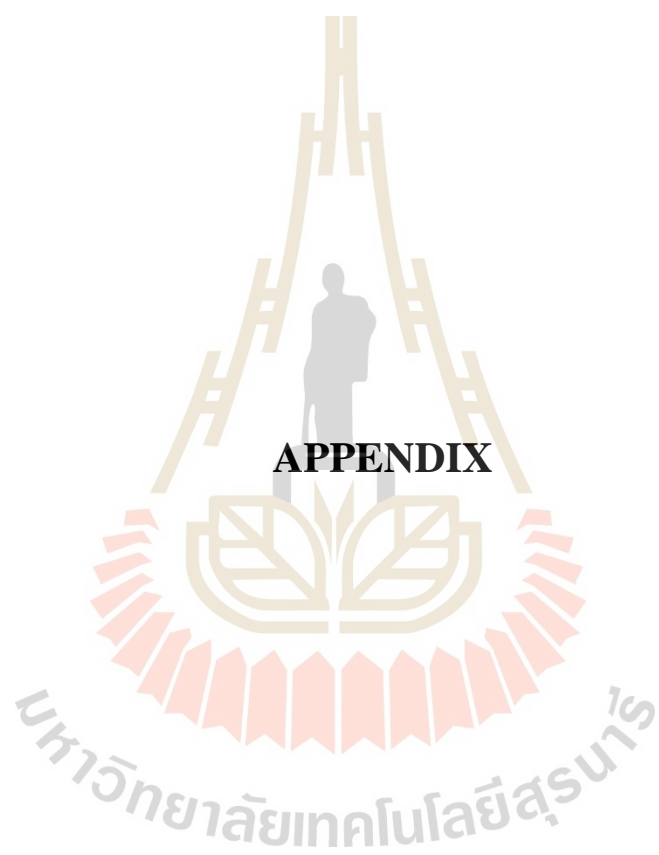
depending on temperature. Fe K-edge XANES spectra were taken. The results showed that there are gradual changes in feature in the XANES and the shift in absorption edge towards higher with increasing excitation photon energy, indicating the increase in the average oxidation state of Fe atoms in the materials. The gradual increase of the oxidation state is, in fact, due to the increase of the percentage of Fe³⁺ with temperature. Quantitative analysis of the valence states of Fe was performed using the empirical edge-shift calculations with comparisons to known standard samples (FeO and Fe₂O₃). The oxidation state was found to increase linearly from 2.00+ to 2.65+ when the temperature increases from room temperature to 800 °C and remains constant at higher temperatures.

More detailed temperature-dependent XAS experiments were performed on LiCoO₂, where *in situ* Co K-edges XANES and EXAFS spectra were taken and analyzed for determining the local structure around Co at different temperatures. The absorption edge energy of the Co K-edge in the XANES spectra decreases linearly with increasing temperature. This corresponds to a decrease in Co oxidation state, indicating the transformation from the higher Co³⁺ to lower Co²⁺ increases with temperature. Furthermore, the results from EXAFS analysis show a strong correlation between rising the link lengths and temperature. More specifically, the local bond lengths of Co-neighbor atoms obtained by Co K-edge EXAFS fitting may be interpreted as a function of temperature. The higher temperature, the larger Co–O/Co–Co bonding distances.

In the CoFe₂O₄ system, the experimental XANES spectra showed that the oxidation state of Fe and Co atom decreases with increasing temperature. In addition, the EXAFS analyzed data provide a clear evidence of the formation of metal phases.

This is deduced from disappearance of Metal atom-Oxygen bond peak and the emerging Metal-Metal atoms bond peak when increasing temperature.

It is remarked that the home-developed *in situ* cell can be used for the temperature-dependent XAS experiment for determining oxidation state and local structural of interested atoms in various materials. As the equipment developed from this thesis work is available for all users of the SUT-NANOTEC-SLRI XAS beamline (BL5.2), the opportunities are opened for all qualified users to access to temperature-dependent XAS technique. The *in situ* XAS is an advanced technique for real-time investigations of reaction changes at different temperatures to obtain the structure and chemical characteristics of semiconductors, polymer and magnetic materials, as well as to track changes during chemical reactions and interactions. It is suggested that a combination of the *in situ* XAS and other conventional techniques should also provide a powerful characterization measurement for several advanced materials for improving fabrication processes or investigating their functions at required operating temperatures.



APPENDIX

APPENDIX

Conference and Presentations

Chinawat Ekwongsa, Naratip Vittayakorn, Manoon Suttapun, Rattikorn Yimnirun, Pinit Kidkhunthod. “Temperature dependent local structure of LiCoO_2 determined by *in situ* Co K-edge X-ray absorption fine structure (EXAFS)” The International Meeting on Ferroelectricity 2017, San Antonio, USA

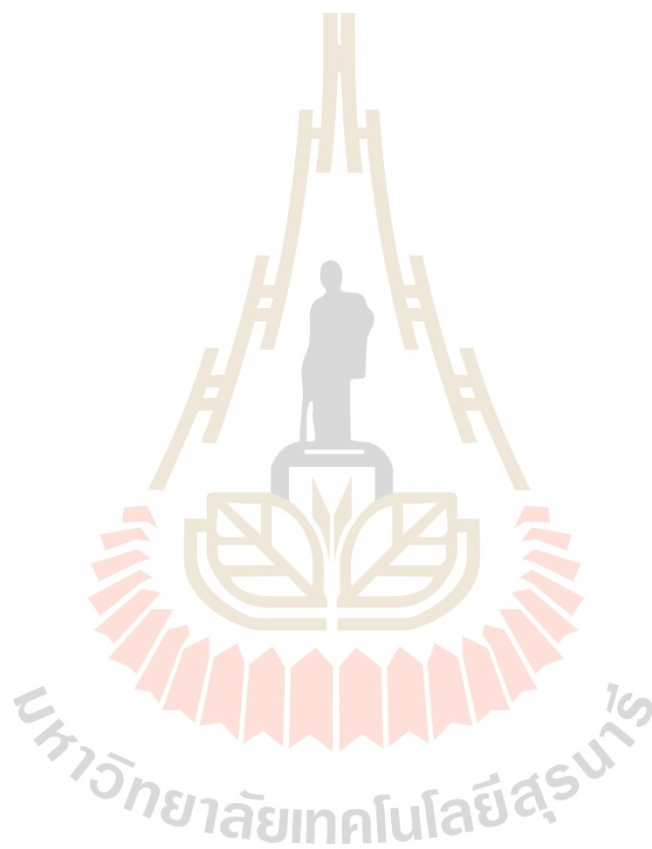
Chinawat Ekwongsa, Naratip Vittayakorn, Manoon Suttapun, Pinit Kidkhunthod, Narong Chanlek, Saroj Rujirawat, Rattikorn Yimnirun. “Temperature dependent local structure of MnFe_2O_4 determined by *in situ* X-ray absorption fine structure (EXAFS)” The First MRS Thailand International Conference 2017, Thailand

Chinawat Ekwongsa, Saroj Rujirawat, Naratip Vittayakorn, Manoon Suttapun, Rattikorn Yimnirun, Pinit Kidkhunthod. “Temperature dependent local structure of LiCoO_2 determined by *in situ* Co K-edge X-ray absorption fine structure (EXAFS)” The 17th International Conference on X-Ray Absorption Fine Structure 2018, Poland.

Chinawat Ekwongsa, Saroj Rujirawat¹, Pinit Kidkhunthod, Naratip Vittayakorn, Manoon Suttapun and Rattikorn Yimnirun. “*in situ* XAS Investigation of Reduction and Oxidation Processes In Cobalt and Iron Mixed Spinels”. The ASIAN Conference on X-ray Absorption Spectroscopy 2019, Thailand

Chinawat Ekwongsa, Prapan Manyum, Saroj Rujirawat, Narong Chanlek, Naratip Vittayakorn, Manoon Suttapun, Rattikorn Yimnirun and Pinit Kidkhunthod. “*in situ* XAS Investigation of Reduction and Oxidation Processes In Cobalt and Iron

Mixed Spinels CoFe_2O_4 ". The 5th International Conference on Smart Materials and Nanotechnology 2020, Thailand



Abstract submitted for the International Meeting on Ferroelectricity 2017, USA

Temperature dependent local structure of LiCoO₂ determined by *in situ* Co K-edge X-ray absorption fine structure (EXAFS)

Chinawat Ekwongsa^{1,*}, Naratip Vittayakorn², Manoon Suttapun², Rattikorn Yimnirun¹, Pinit Kidkhunthod³

¹*School of Physics, Institute of Science, and NANOTEC-SUT COE on Advanced Functional Nanomaterials, Suranaree University of Technology, NakhonRatchasima, Thailand 30000*

²*Department of Chemistry, Faculty of Science, King Mongkut's Institute of Technology Ladkrabang, Bangkok 10520, Thailand*

³*Synchrotron Light Research Institute (Public Organization), 111 University Avenue, Muang District, NakhonRatchasima 30000, Thailand*

Abstract

Lithium cobalt oxide (LiCoO₂) currently has a great attention as active cathode material lithium ion batteries. In this work, lithium cobalt oxide was prepared by solid state reaction and co-precipitation method. The synthesis parameters and phase formation behavior were investigated in details via several techniques, including thermal analysis, X-Ray Diffraction (XRD), Scanning Electron Microscopy (SEM) and X-ray Photoelectron Spectroscopy (XPS). A change in local structure was investigated using *in situ* extended X-ray absorption fine structure (EXAFS). The temperature ranged between 400°C and 700°C with air condition was applied for this study. The results will be presented and discussed in details.

Keywords: Lithium cobalt oxide; extended X-ray absorption fine structure.

* **Corresponding author's email:** Chinawatjo.sut@gmail.com

Abstract submitted for the Frist MRS Thailand International Conference 2017,

Thailand

Abstract submitted for the Frist MRS Thailand International Conference 2017, Thailand

Temperature dependent local structure of MnFe_2O_4 determined by *in situ* X-ray absorption fine structure (EXAFS)

Chinawat Ekwongsa^{1,*}, Naratip Vittayakorn², Manoon Suttapun², Pinit Kidkhunthod³,
Narong Chanlek³, Saroj Rujirawat¹, Rattikorn Yimnirun¹

¹*School of Physics, Institute of Science, and NANOTEC-SUT COE on Advanced Functional Nanomaterials, Suranaree University of Technology, Nakhon Ratchasima, Thailand 30000*

²*Department of Chemistry, Faculty of Science, King Mongkut's Institute of Technology Ladkrabang, Bangkok 10520, Thailand*

³*Synchrotron Light Research Institute (Public Organization), 111 University Avenue, Muang District, Nakhon Ratchasima 30000, Thailand*

*Corresponding Author's E-mail: Chinawatjo.sut@gmail.com

Abstract

The magnetic spinel ferrites, MnFe_2O_4 , have been widely studied for their novel magnetic and electronic properties. In this work, MFe_2O_4 were prepared by solid state reaction and co-precipitation method. The synthesis parameter and the phase formation behaviour were investigated in details via several techniques, including thermal analysis, X-Ray Diffraction (XRD), Scanning Electron Microscopy (SEM) and X-ray Photoelectron Spectroscopy (XPS). A change in local structure was investigated using *in situ* extended X-ray absorption fine structure (EXAFS). The temperature ranged between 50°C and 300°C with air condition was applied for this study. The results will be presented and discussed in details.

Keywords; The magnetic spinel ferrites; X-ray absorption fine structure.

Abstract submitted for the 17th International Conference on X-Ray Absorption Fine Structure 2018, Poland

Temperature dependent local structure of LiCoO₂ determined by *in situ* Co K-edge X-ray absorption fine structure (EXAFS)

Chinawat Ekwongsa^{1,*} Saroj Rujirawat¹, Naratip Vittayakorn², Manoon Suttapun², Rattikorn Yimnirun³, Pinit Kidkhunthod⁴

¹School of Physics, Institute of Science, and NANOTEC-SUT COE on Advanced Functional Nanomaterials, Suranaree University of Technology, Nakhon Ratchasima, 30000, Thailand

²Department of Chemistry, Faculty of Science, King Mongkut's Institute of Technology Ladkrabang, Bangkok 10520, Thailand

³School of Energy Science and Engineering, Vidyasirimedhi Institute of Science and Technology, Rayong 21210, Thailand

³Department of Chemistry, Faculty of Science, King Mongkut's Institute of Technology Ladkrabang, Bangkok 10520, Thailand

⁴Synchrotron Light Research Institute (Public Organisation), Nakhon Ratchasima, 30000, Thailand

*Corresponding Author: chinawatjo.sut@gmail.com

Recently, lithium cobalt oxide (LiCoO₂) has a great attention as active cathode material lithium ion batteries. In this work, LiCoO₂ powder was prepared by solid state reaction and co-precipitation method. The synthesis parameters and phase formation behavior were investigated in details via several techniques, including thermal analysis, including thermal analysis, X-Ray Diffraction (XRD) and Scanning Electron Microscopy (SEM). A change in local structure around Co atoms was investigated using *in situ* extended X-ray absorption fine structure (EXAFS). The temperature ranged between 400°C and 700°C with air condition was applied for this study. Furthermore the paramagnetism of samples was also observed using the vibrating sample magnetometry (VSM).

Abstract submitted for the ASIAN Conference on X-ray Absorption Spectroscopy
2019, Thailand

in situ XAS Investigation of Reduction and Oxidation Processes In
Cobalt and Iron Mixed Spinel

Chinawat Ekwongsa^{1,*}, Saroj Rujirawat¹, Pinit Kidkhunthod^{2,*}, Naratip Vittayakorn³,
Manoon Suttapun³ and Rattikorn Yimnirun⁴

¹*School of Physics, Institute of Science, and NANOTEC-SUT COE on Advanced Functional Nanomaterials, Suranaree University of Technology, Nakhon Ratchasima, 30000, Thailand*

²*Synchrotron Light Research Institute (Public Organization), 111 University Avenue, Muang District, NakhonRatchasima 30000, Thailand*

³*Department of Chemistry, Faculty of Science, King Mongkut's Institute of Technology Ladkrabang, Bangkok 10520, Thailand*

⁴*School of Energy Science and Engineering, Vidyasirimedhi Institute of Science and Technology (VISTEC), Payupnai, Wangchan, Rayong 21210, Thailand*

*Corresponding Author: chinawatjo.sut@gmail.com and pinit@slri.or.th

Symposia: Electrical, magnetic, and optical materials

The magnetic spinel ferrites, CoFe_2O_4 , have been widely studied for their novel magnetic and electronic properties. In this work, CoFe_2O_4 were prepared by solid-state reaction and co-precipitation method. The synthesis parameter and the phase formation behaviour were investigated in details via several techniques, including thermal analysis, X-ray diffraction (XRD) and Transmission electron microscopy (TEM). Reduction and oxidation processes were investigated using X-ray absorption near edge structure (XANES). A change in local structure was investigated using *in situ* extended X-ray absorption fine structure (*in situ* EXAFS). The temperature in the range of 25°C to 800°C has been investigated local structure of *in situ* EXAFS system.

The XRD patterns of the samples were confirmed the presence of CoFe_2O_4 pure phase (space group Fd-3m) at 800°C/6 hr. CoFe_2O_4 is reduced to a mixed wüstite in first place and, subsequently, to a Co-Fe alloy. Fe, instead, is quickly and almost quantitatively transformed into wüstite, which is only partially reduced to metal.

Abstract submitted for the 5th International Conference on Smart Materials and Nanotechnology 2020, Thailand

***in situ* XAS Investigation of Reduction and Oxidation Processes In Cobalt and Iron Mixed Spinel CoFe₂O₄**

Chinawat Ekwongsa^{1,*}, Prapan Manyum¹, Saroj Rujirawat², Narong chanlek², Naratip Vittayakorn³, Manoon Suttapun³, Rattikorn Yimnirun⁴ and Pinit Kidkhunthod^{2,*}

¹School of Physics, Institute of Science, and NANOTEC-SUT COE on Advanced Functional Nanomaterials, Suranaree University of Technology, NakhonRatchasima, Thailand 30000

²Synchrotron Light Research Institute (Public Organization), 111 University Avenue, Muang District, NakhonRatchasima 30000, Thailand

³Department of Chemistry, Faculty of Science, King Mongkut's Institute of Technology Ladkrabang, Bangkok 10520, Thailand

⁴School of Energy Science and Engineering, Vidyasirimedhi Institute of Science and Technology, Rayong 21210, Thailand

*Email: chinawatjo.sut@gmail.com

Abstract

The magnetic spinel ferrites, CoFe₂O₄, have been widely studied for their novel magnetic and electronic properties. In this work, CoFe₂O₄ were prepared by coprecipitation method. The synthesis parameter and the phase formation behaviour were investigated in details via several techniques, including thermal analysis, X-ray diffraction (XRD) and Transmission electron microscopy (TEM). Reduction and oxidation processes were investigated using X-ray absorption near edge structure (XANES). A change in local structure was investigated using *in situ* extended X-ray absorption fine structure (*in situ* EXAFS). The temperature in the range of 25°C to 800°C has been investigated local structure of *in situ* EXAFS system.

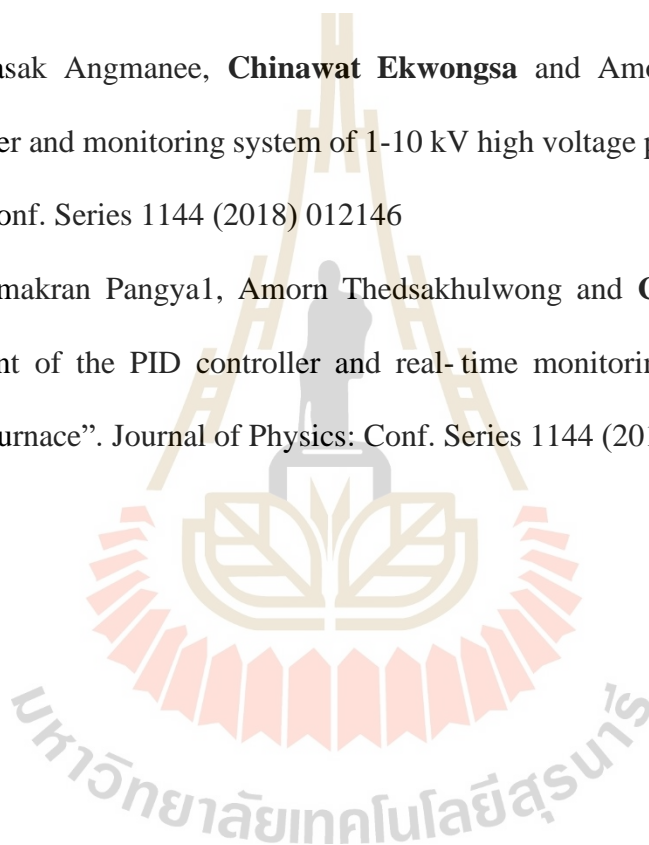
Keyword: The magnetic spinel ferrites and *in situ* EXAFS

International Publications

Chinawat Ekwongsa, Saroj Rujirawat, Pichitchai Butnoi, Naratip Vittayakorn, Manoon Suttapunc, Rattikorn Yimnirun and Pinit Kidkhunthod. “ Temperature dependent local structure of LiCoO₂ determined by *in situ* Co K-edge X-ray absorption fine structure (EXAFS)”. **Radiation Physics and Chemistry**. Volume 175, October 2020, 108545

Bundasak Angmanee, **Chinawat Ekwongsa** and Amorn Thedsakhulwong. “The controller and monitoring system of 1-10 kV high voltage power supply” Journal of Physics: Conf. Series 1144 (2018) 012146

Thammakran Pangya¹, Amorn Thedsakhulwong and **Chinawat Ekwongsa**. “Development of the PID controller and real-time monitoring system for a low-temperature furnace”. Journal of Physics: Conf. Series 1144 (2018) 012160





Contents lists available at ScienceDirect

Radiation Physics and Chemistry

journal homepage: www.elsevier.com/locate/radphyschem

Temperature dependent local structure of LiCoO₂ determined by in-situ Co K-edge X-ray absorption fine structure (EXAFS)

Chinawat Ekwongsa^a, Saroj Rujirawat^a, Pichitchai Butnoi^b, Naratip Vittayakorn^c, Manoon Suttapun^c, Rattikorn Yimnirun^d, Pinit Kidkhunthod^{b,*}

^a Research Network NANOTEC-SUT on Advanced Nanomaterials and Characterization, School of Physics, Institute of Science, Suranaree University of Technology, Nakhon Ratchasima, 30000, Thailand

^b Synchrotron Light Research Institute (Public Organization), 111 University Avenue, Muang District, Nakhon Ratchasima, 30000, Thailand

^c Department of Chemistry, Faculty of Science, King Mongkut's Institute of Technology Ladkrabang, Bangkok, 10520, Thailand

^d School of Energy Science and Engineering, Vidyasirimedhi Institute of Science and Technology, Rayong, 21210, Thailand

ARTICLE INFO

Keywords:

Lithium cobalt oxide
In-situ extended X-ray absorption fine structure
Local structure

ABSTRACT

Recently, lithium cobalt oxide (LiCoO₂) has a great attention as active cathode material lithium ion batteries. In this work, LiCoO₂ powder was prepared by solid state reaction and co-precipitation method. The synthesis parameters and phase formation behavior were investigated in details via several techniques, including thermal analysis, X-ray diffraction (XRD) and scanning electron microscopy (SEM). A change in local structure depending on temperature around Co atoms was investigated using in-situ extended X-ray absorption fine structure (EXAFS). The temperature ranged between 300 °C and 700 °C under air condition was applied for this study.

1. Introduction

These days, lithium cobalt oxide (LiCoO₂) has been widely attractive and a great interest for its application as cathode material in lithium ion batteries due to its high specific capacity, low self-discharge and excellent cycle life (Plichta et al., 1989; Gibbard, 1989; Nagura and Tazawa, 1990; Kang et al., 1999; Patridge et al., 2013). The crystalline, the average particle size and particle size distribution of this material are the important factors to achieve high performance rechargeable lithium batteries.

Generally, many researchers prepared LiCoO₂ by solid-state reaction. However, owing to insufficient mixing and the low reactivity of the starting materials, calcination at 850–900 °C for several hours is required to successfully synthesize LiCoO₂. Typically, LiCoO₂ exhibits two forms, a cubic phase and a hexagonal phase at low temperature (LT-LiCoO₂) and high temperature (HT-LiCoO₂), respectively. The cubic and hexagonal structures are based on the same oxide sub-lattice, and are distinguished by the spatial arrangement of cations (Antolini, 2004). It has a hexagonal structure in which the Li⁺ and Co³⁺ ions are ordered in the alternate (1 1 1) planes of octahedral sites, nearly cubic close packed oxygen lattice (Orman and Wiseman, 1984; Dahéron et al., 2008). To understand a formation of crystallized LiCoO₂ powders with a function of temperature, several works have been studied these materials using a solid-state reaction and co-precipitation as synthesized

methods. The crystal structure of the complex oxides of the LiCoO₂ was reviewed by Kellerman (Kellermann, 2001) where the formation, structure and transport properties of lithium cobalt oxide were studied carefully.

In this research work, LiCoO₂ powders will be studied with both structural and physical studies by X-ray diffraction (XRD) and scanning electron microscopy (SEM). A very simply synthesis method using solid state reaction and co-precipitation method has been used to synthesize these LiCoO₂ powders. Furthermore, the synchrotron-based X-ray absorption spectroscopy (XAS) technique including in-situ X-ray absorption near edge structure (in-situ XANES) and in-situ extended X-ray absorption fine structure (in-situ EXAFS) has been employed in order to deeply address the existence of cobalt oxidation states and local structural information around cobalt atoms.

2. Experiment and characterization

2.1. Sample preparation

The LiCoO₂ powder was synthesized by using the solid-state reaction and co-precipitation method in ethanol solution with continuous magnetic stirring. Reagent-grade metal nitrate, LiNO₃·6H₂O (99.0%, Fluka) and Co(NO₃)₂·6H₂O (99.90%, Sigma-Aldrich) powders were used as raw materials. LiNO₃·6H₂O and Co(NO₃)₂·6H₂O were dissolved

* Corresponding author.

E-mail address: pinit@sri.or.th (P. Kidkhunthod).

<https://doi.org/10.1016/j.radphyschem.2019.108545>

Received 27 September 2018; Received in revised form 15 October 2019; Accepted 25 October 2019

Available online 29 October 2019

0969-806X/ © 2019 Elsevier Ltd. All rights reserved.

in ethanol with mole ratio of 1:1:1. The total mole concentration is 2.1 M and this solution was referred to as solution A. The 3 M of KOH was dissolved ethanol solution, which is referred as solution B. 100 mL of solution A was added slowly to 500 mL of solution B with continuous magnetic stirring at room temperature for 1 h. Finally, the dark precipitation of precursor was obtained. A solution was separated by centrifugal separator of 7000 rpm for 10 min and then washed powder with ethanol until free from nitrate, potassium and hydroxide ions and dried in air.

2.2. Structural and morphological characterizations

The crystal structure and phase evolution of the powders were characterized using an X-ray diffractometer (XRD; Rigaku SmartLab) obtained by using Cu K α radiation with $\lambda = 1.5418 \text{ \AA}$. Room temperature XRD data was collected in the 2θ scan range of $10\text{--}60^\circ$ with step size of 0.02° and scanning rate of 2.5° per minute. The Microstructural observation was performed by using the SEM (FEI-Quanta 450).

2.3. XAS data analysis

Synchrotron-based XANES and EXAFS spectra were conducted at the SUT-NANOTEC-SLRI XAS Beamline (BL5.2) at the Synchrotron Light Research Institute (Public Organization), Thailand (Kidkhunthod, 2017; Klysubun et al., 2017). To characterize the valence states and local structural information of Co atoms, the in-situ experiment XAS including in-situ XANES and EXAFS spectra at Co K-edge spectra were collected in the transmission modes from room temperature to 700°C . The cobalt K-edge absorption data were all calibrated and aligned using reference Co metal spectra with the maximum value of the first derivative set to 7709 eV. The temperature-dependent XAS experiment was performed using in-house heating cell with an optimized pellet form of sample. Additionally, XAS in-house heating cells and supported gas systems and the following schematic diagram of temperature-dependent XAS study are shown in Fig. 1. To measured XAS spectra, synthesized powders were ground to fine powders and pressed into pellet prior to the experiment.

3. Result and discussion

3.1. Structural and morphological characterizations

For investigating the phase formation and the crystal structure of the prepared powders was characterized by X-ray diffraction technique (XRD). The XRD patterns of LiCoO_2 powders prepared by co-precipitation method before and after different calcination temperature where $2\theta = 10\text{--}60^\circ$ are shown in Fig. 2. The change of peak patterns

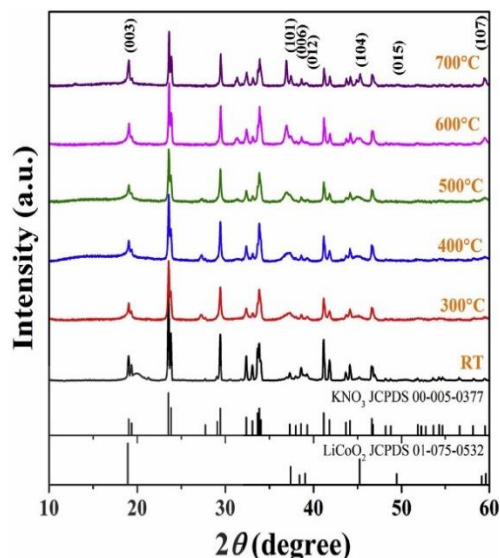


Fig. 2. XRD patterns of LiCoO_2 powders with various calcination temperatures.

and high intensity peaks indicate that phase formation and highly crystalline of powders were transformed by the different calcination temperature conditions. The XRD of all samples can be indexed to Rhombohedral phase LiCoO_2 (space group R-3m) and Orthorhombic phase KNO_3 phase (space group Pmcn) with database file of JCPDS card number 75-0532 and JCPDS card no. 00-005-0377, respectively. It indicates that the prepared powders are two-phase coexistence of LiCoO_2 and by-product KNO_3 , and no evidence detestable starting materials. Meanwhile, the increasing of calcination temperature can increase the crystallinity of LiCoO_2 . It can be seen that the intensity of crystalline LiCoO_2 increased with increasing calcination temperature. It is note that the increasing of (003) and (104) peaks confirmed the increasing of LiCoO_2 when increase calcination temperature. This behavior has been observed for many LiCoO_2 -based materials (Balandeh and Asgari, 2010; Khatun et al., 2014)

To further investigate the surface morphology of the prepared powders, the scanning electron microscopy (SEM) and the energy-dispersive X-ray (EDS) mapping images for the selected SEM region of prepared powders with different calcination temperature are showed in Fig. 3(a-f). The SEM image of all samples present a variety particle size. In addition, the lower calcination temperature powders present spherical particle. Furthermore, the higher calcination temperature present slightly increase cubic-like shape. To explain the distribution of each element in the sample and the elemental compositional information,

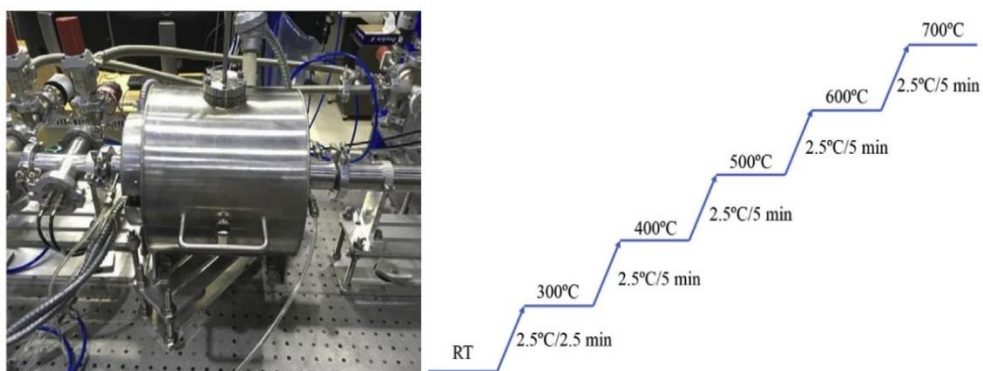


Fig. 1. In situ XAS in-house heating cells for transmission mode and Schematic diagram of In-situ XAS measurement.

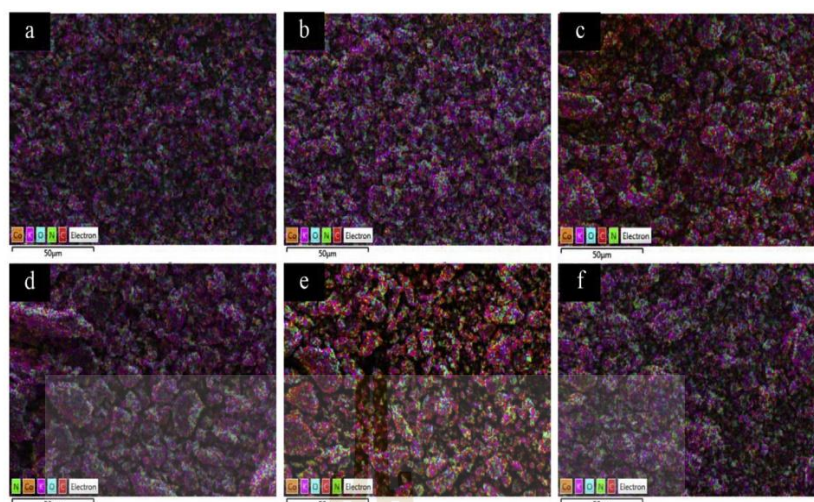


Fig. 3. SEM images of LiCoO₂ samples calcined at various calcination temperature: (a) RT, (b) 300 °C, (c) 400 °C, (d) 500 °C, (e) 600 °C and (f) 700 °C.

the EDS technique was analyzed which present in different colors dot in EDS mapping. The EDS elemental mapping images of the obtained sample confirms the presence of O, Co and N element as shown in EDS mapping, indicating that element atoms were uniformly distributed. However, the EDS technique cannot observe Li element because Li is small atomic number element.

3.2. Structural studies using in-situ XANES and EXAFS

Although, LiCoO₂ powders consist of phase of KNO₃, a majority LiCoO₂ phase can be used to study the electronic structure and local structure around Co atoms using in-situ XAS technique. Fig. 4 shows normalized XANES spectra at the Co K-edge LiCoO₂ samples at several temperatures: (a) RT, (b) 300 °C, (c) 400 °C, (d) 500 °C, (e) 600 °C, (f) 700 °C, CoO (Co²⁺) and Co₂O₃(Co³⁺) standard samples. The characteristic absorption edge of Co exists at 7709 eV, which corresponds to the energy required to eject a core electron from a cobalt atom. The most intense peak A near 7730 eV arises from the electronic transition 1s→4p. The magnified inset around 7710 eV (peak B) comes from the 1s→3d transition which shows a systematic decrease and small shifting to lower energy during rising temperature. This behavior is similar to previous observe by Patridge (Patridge et al., 2013). Moreover, this is consistent with a changing in Co oxidation from higher Co³⁺ to Co²⁺.

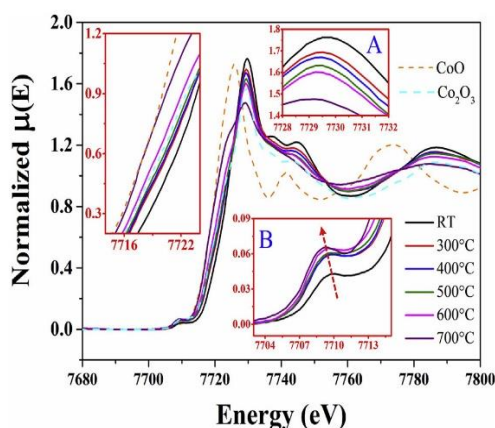


Fig. 4. In-situ XANES spectra of Co K edge of LiCoO₂ samples and standard samples.

As seen in Fig. 4, a shoulder around 7725 eV is observed only for calcination at 700 °C. This suggests a significant change in Co local structure especially for coordinated oxygen atoms surrounding Co atom. This will be discussed in EXAFS section. In more detail, from RT to 700 °C, the decreased intensity of normalized absorbance is clearly observed indicating more orbital mixing and more increase in distortion of the CoO₆ octahedra (Patridge et al., 2013).

In order to understand the local environment of Co atoms in the structure, the EXAFS spectra were intensively analyzed and fitted using Athena and Artemis programs as implement in the IFFEFIT packages (Ravel and Newville, 2005). The EXAFS spectra of the corresponding Fourier transform (FT) in R space at Co K-edge of all samples are shown in Fig. 5. It can be seen that the amplitude of Co–O and Co–Co peaks remain almost the same. These patterns can be observed with other systems of Li_xCoO₂ and Li_xNiO₂ (Deb et al., 2007; Rumble et al., 2010). Moreover, to investigate structural parameters of local environment around Co atom was analyzed based on FT fitting. Plots of Co K-edge K²-weighted Fourier transform fitting from experiment (black line) and fitting (red line) at different calcination temperature of LiCoO₂ are shown inset Fig. 5. The FT provides information on the partial atomic distribution around the Co atoms in the LiCoO₂ system. The FT shows first scattering contributions from the nearest neighbor O atoms at a distance about 1.92 Å, and the next nearest neighbors Co atoms at a distance about 2.81 Å. The contribution of Co–Li distance is hardly seen due to negligible scattering factor of lithium in comparison with Co. The peaks at longer distances are due to multiple scattering contributions. This implies the local environments around Cobalt atoms are almost identical. The Co–O and Co–Co models were used for the fit. The best parameters of the EXAFS fitting such as interatomic distances (R), Debye–Waller factors (σ²), amplitude reduction (S₀²) and R-factor were shown in Table 1. In this study, in order to study the influence of temperature to Co local structure in term of Debye–Waller factors (σ²), the amplitude reduction (S₀²) is set to be equally 0.75 for all temperatures. Moreover, the mean coordination numbers were obtained to be between 4.8(1) and 5.7(2) for both Co–O and Co–Co, respectively.

Again, as seen in Table 1, an increase trend in Debye–Waller factors is obtained with rising temperature (approximately of 10% relative error). This implies and supports the XANES results for more structural distortion around Co atoms in LiCoO₂ structure. In more detail, local bond lengths of Co-neighboring atoms determined by Co K-edge EXAFS fitting can be understood as a function of temperature as seen in Fig. 6 (less than ± 0.01 Å of error distance value). The higher temperature, the larger Co–O/Co–Co bonding distances.

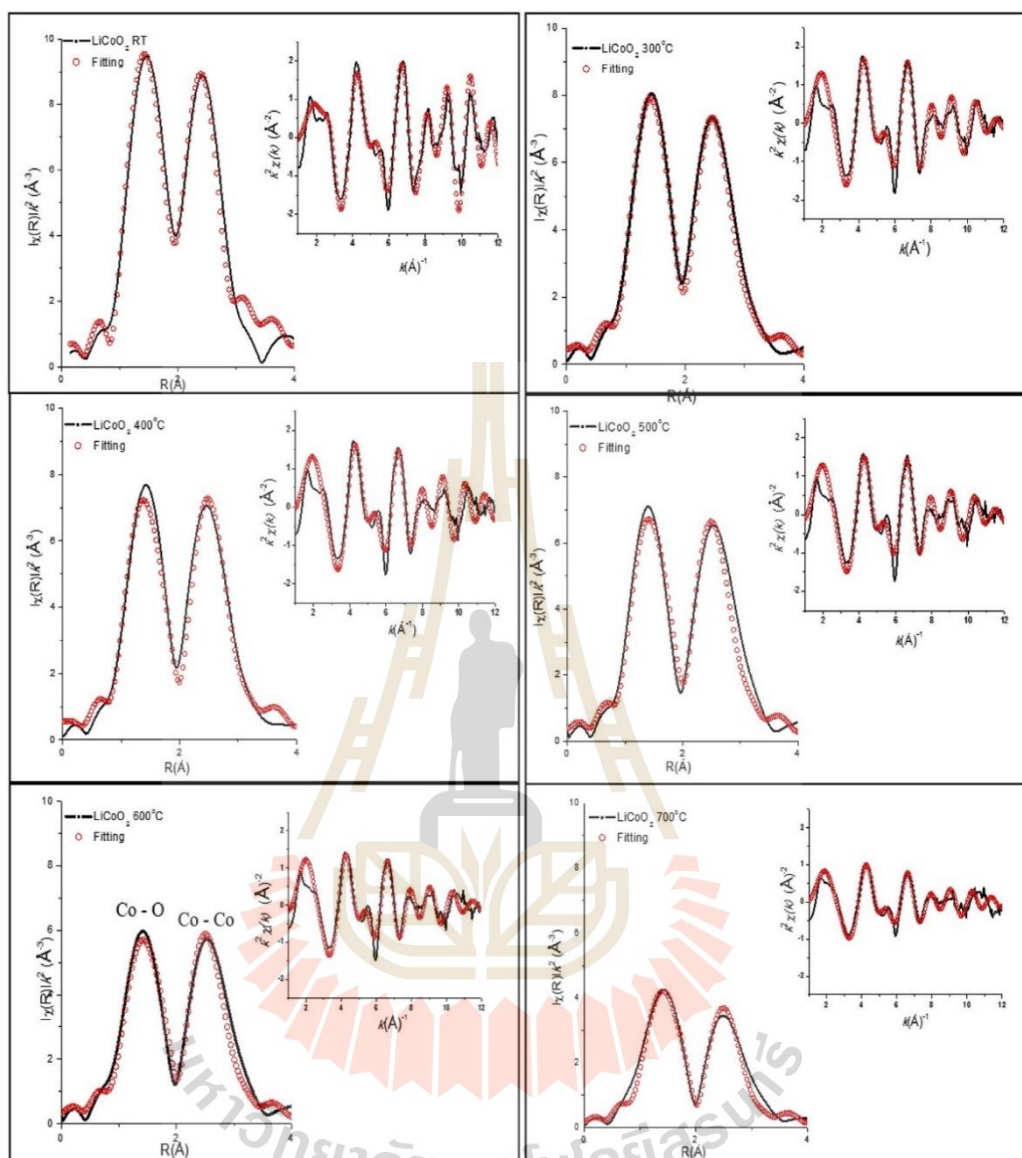


Fig. 5. Fourier transform at in-situ EXAFS spectra at Co K-edge EXAFS (weighted by k^2) from experiment (black line) and fitting (red circle) of LiCoO_2 at different temperature. Model fits to the experimental filtered EXAFS in the k -space are also shown (insets). Experimental filtered EXAFS in the k -space are also shown (insets). (For interpretation of the references to color in this figure legend, the reader is referred to the Web version of this article.)

Table 1
EXAFS fitting parameters including interatomic distances (R), coordination numbers (N), Debye–Waller factors (σ^2) and amplitude reduction (S_0^2).

Sample	Shell	σ^2	R(Å)	R-factor	S_0^2
LiCoO_2 25 °C	Co–O	0.0030	1.893(2)	1.10%	0.75
	Co–Co	0.0040	2.850(1)		
LiCoO_2 300 °C	Co–O	0.00630	1.905(1)	2.18%	0.75
	Co–Co	0.00730	2.861(1)		
LiCoO_2 400 °C	Co–O	0.00855	1.905(1)	3.27%	0.75
	Co–Co	0.00855	2.889(2)		
LiCoO_2 500 °C	Co–O	0.00824	1.922(1)	3.79%	0.75
	Co–Co	0.00864	2.888(1)		
LiCoO_2 600 °C	Co–O	0.00989	1.931(2)	2.96%	0.75
	Co–Co	0.00878	2.894(1)		
LiCoO_2 700 °C	Co–O	0.01304	1.927(1)	1.76%	0.75
	Co–Co	0.01920	2.911(1)		

4. Conclusion

Temperature-dependent on local structure of the LiCoO_2 powders was successfully studied by in-situ by Co K-edges X-ray absorption spectroscopy including in-situ XANES and EXAFS. The XANES spectra at the Co K-edge show a linearly decrease of edge energy during increasing temperature. This is consistent with a reduction change in Co oxidation state from higher Co^{3+} to Co^{2+} . Additionally, the EXAFS data provide a clear evidence of increasing bond lengths with the increasing temperature.

Acknowledgments

The authors would like to thank the Synchrotron Light Research Institute (Public Organization) (BL5.2), Thailand for the XAS facilities. Many thanks to School of Physics, Suranaree University of Technology

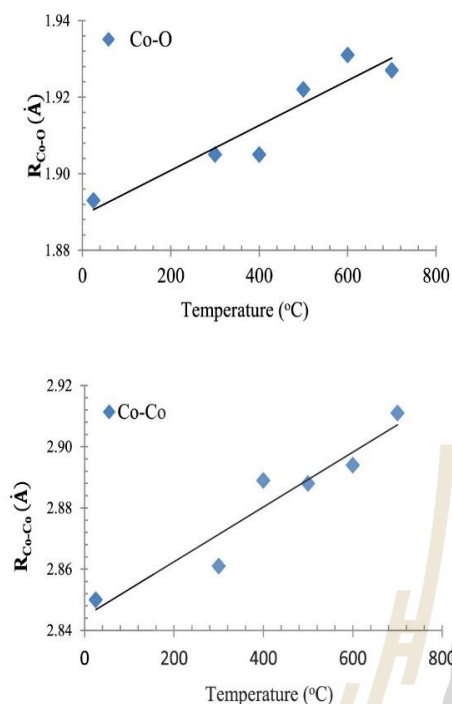


Fig. 6. The local neighboring Co-O (a) and Co-Co (b) distances in LiCoO₂ structure as a function of temperature.

for laboratory facilities. Moreover, many thank you for some financial support by the NANOTEC, NSTDA, Ministry of Science and Technology, Thailand, through its program of Research Network NANOTEC. C. E. would like to thank you the DPST for his Ph.D. scholarship.

References

Dahéron, L., Dedryvère, R., Martinez, H., Ménétrier, M., Denage, C., Delmas, C., Gonbeau,

- D., 2008. Electron transfer mechanisms upon lithium deintercalation from LiCoO₂ to CoO₂ investigated by XPS. *Chem. Mater.* 20 (2), 583–590.
- Antolini, E., 2004. LiCoO₂: formation, structure, lithium and oxygen nonstoichiometry, electrochemical behaviour and transport properties. *Solid State Ion.* 170 (1), 159–171.
- Balandeh, M., Asgari, S., 2010. Synthesis and characterization of LiNiO₂ nanopowder with various chelating agents. *J. Nanomater.*, 695083.
- Deb, A., Bergmann, U., Bergmann, U., Cramer, S.P., Cairns, E.J., 2007. In situ X-ray absorption spectroscopic study of Li_{1.05}Ni_{0.35}Co_{0.25}Mn_{0.4}O₂ Cathode Material Coated with LiCoO₂. *J. Electrochem. Soc.* 154 (6), A534–A541.
- Gibbard, H.F., 1989. High temperature, high pulse power lithium batteries. *J. Power Sources* 26 (1–2), 81–91.
- Kang, S.G., Kang, S.Y., Ryu, K.S., Chang, S.H., 1999. Electrochemical and structural properties of HT-LiCoO₂ and LT-LiCoO₂ prepared by the citrate sol-gel method. *Solid State Ion.* 120 (1–4), 155–161.
- Kellermann, D.G., 2001. Magnetic properties of complex oxides LiMO₂ (M = Sc–Ni) with different types of cationic ordering. *Russ. Chem. Rev.* 70 (9), 777.
- Khatun, F., Gafur, M.A., Ali, M.S., Islam, M.S., Serker, M.A.R., 2014. Impact of lithium composition on structural, electronic and optical properties of lithium cobaltite prepared by solid-state reaction. *J. Sci. Res.* 6 (2), 217–231.
- Kidkhunthod, P., 2017. Structural studies of advanced functional materials by synchrotron-based x-ray absorption spectroscopy: BL5.2 at SLRI, Thailand. *Adv. Nat. Sci. Nanosci. Nanotechnol.* 8 (3), 035007.
- Klysubun, W., Kidkhunthod, P., Tarawarakarn, P., Sombunchoo, P., Kongmark, C., Limpjumnong, S., Rujirawat, S., Yinnirun, R., Tumcharern, G., Faungnawakij, K., 2017. SUT-NANOTEC-SLRI beamline for X-ray absorption spectroscopy. *J. Synchrotron Radiat.* 24, 707–716.
- Nagura, T., Tazawa, K., 1990. Lithium ion rechargeable battery. *Prog. Batter. Sol. Cells* 9, 209–217.
- Orman, H.J., Wiseman, P.J., 1984. Cobalt (III) lithium oxide, CoLiO₂: structure refinement by powder neutron diffraction. *Acta Crystallogr.* C40, 12–14.
- Patridge, C.J., Love, C.T., Swider-Lyons, K.E., Twigg, M.E., Ramaker, D.E., 2013. In-situ X-ray absorption spectroscopy analysis of capacity fade in nanoscale-LiCoO₂. *J. Solid State Chem.* 203, 134–144. <https://www.sciencedirect.com/science/article/pii/S0022459613002028?via%3Dihub-1> <https://www.sciencedirect.com/science/article/pii/S0022459613002028?via%3Dihub-1>
- Plichta, E., Slane, S., Uchiyama, M., Saloman, M., Chua, D., Ebner, W., Lin, H., 1989. An improved Li/Li_{1-x}CoO₂ rechargeable cell. *J. Electrochem. Soc.* 136 (7), 1865–1869.
- Ravel, B., Newville, M., 2005a. ATHENA, ARTEMIS, HEPHAESTUS: data analysis for X-ray absorption spectroscopy using IFEFFIT. *J. Synchrotron Radiat.* 12 (4), 537–541.
- Ravel, B., Newville, M., 2005b. ATHENA and ARTEMIS: interactive graphical data analysis using IFEFFIT. *Phys. Scr. T* 115 (22), 1007–1010.
- Rumble, C., Conry, T.E., Doeff, M., Cairns, E.J., Penner-Hahn, J.E., Deb, A., 2010. Structural and electrochemical investigation of Li(Ni_{0.4}Co_{0.15}Al_{0.05}Mn_{0.4})O₂ cathode. *Material. J. Electrochem. Soc.* 157 (12), A1317–A1322.



Local structure and structural properties of vanadium oxide thin films prepared by radio-frequency reactive magnetron sputtering at various oxygen flow rate

Piyaporn Thangdee^a, Ekachai Chongserecharoen^b, Thanun Chunjaemsri^a, Chinawat Ekwongsa^a, Pinit Kidkhunthod^c, Narong Chanlek^c, Natthapong Wongdamnern^d, Prapan Manyum^e, Saroj Rujirawat^c, and Rattikorn Yimnirun^{f,g}

^aResearch Network NANOTEC-SUT on Advanced Nanomaterials and Characterization, School of Physics, Institute of Science, Suranaree University of Technology, Nakhon Ratchasama, Thailand; ^bFaculty of Science and Technology, Valaya Alongkorn Rajabhat University, Klong Luang, Pathumthani, Thailand; ^cSynchrotron Light Research Institute (Public Organization), Nakhon Ratchasama, Thailand; ^dFaculty of Science and Technology, Rajamangala University of Technology Suvarnabhumi, Nonthaburi, Thailand; ^eSchool of Physics and Center of Excellence in High Energy Physics and Astrophysics, Suranaree University of Technology, Nakhon Ratchasama, Thailand; ^fSchool of Energy Science and Engineering, Vidyasirimedhi Institute of Science and Technology (VISTEC), Wangchan, Rayong, Thailand; ^gResearch Network of NANOTEC-VISTEC on Nanotechnology for Energy, Vidyasirimedhi Institute of Science and Technology (VISTEC), Wangchan, Rayong, Thailand

ABSTRACT

In this work, vanadium oxide thin films were prepared by using radio frequency reactive magnetron sputtering with vanadium metal target. The effect of O₂ flow rate was investigated in terms of vanadium oxide thin films by varying O₂/Ar flow rate at 1/20, 2/20, 3/20, 4/20, 5/20, 6/20 (in sccm unit) with fixed RF power at 200 W and sputtering time at 80 minutes. The surface morphology and crystal structure of V₂O₅ thin films were investigated by scanning electron microscope (SEM), atomic force microscope (AFM), and X-Ray Diffractometer (XRD) respectively. The influence of the O₂/Ar ratio on a local structure of vanadium oxide thin films was studied by the Synchrotron x-ray absorption spectroscopy (XAS) technique. The oxidation states of vanadium oxide thin films were measured at V K-edge by the x-ray absorption near-edge structure (XANES). The results of XANES spectra at the V K-edge showed that the prepared films under the O₂/Ar flow rate at 1/20 sccm contained the vanadium with the oxidation states of V³⁺ and V⁵⁺ while the others contained only V⁵⁺. This is because the higher O₂/Ar flow rate possibly causes an increase in energy flux at the substrate and the 1s→3d transition peak's intensity, which could lead to a higher deposition rate. To achieve the desired V₂O₅ structure, the gas flow rate could be adjusted properly. The evolution of the local structure around V atoms was studied using the extended x-ray absorption fine structure (EXAFS) which supported the XANES results indicating that the structural environment around V atoms is in good agreement with the V₂O₅ orthorhombic structure. Finally, XANES and EXAFS fitting results confirmed that the O₂ flow rate affected the local structure of vanadium oxide thin films.

ARTICLE HISTORY

Received 24 July 2021
Accepted 25 October 2021

KEYWORDS

Vanadium oxide thin films; O₂/Ar ratio; x-ray absorption near-edge structure (XANES); extent x-ray absorption fine structure (EXAFS); radio-frequency reactive magnetron sputtering

1. Introduction

The vanadium pentaoxide (V_2O_5) is one of the promising materials for many applications. V_2O_5 , a wide band gap and an n-type semiconductor material, is widely studied because of its interesting thermochromic and electrochromic properties. Progress is currently made to improve its performance for use as a gas sensor. V_2O_5 thin films have got much piqued interest. The active sites generated by V^{5+} ions are responsible for gaseous molecule adsorption and catalytic processes. The electrochromic, electrolyte, and ion storage layers make up a standard electrochromic device (ECD). On the transparent substrates covered with a transparent conductive film, both electrochromic and storage layers are deposited. ECDs work by varying the optical characteristics of different hues. In ECDs, V_2O_5 is used as a counter electrode material. It produces electrochemical redox reactions that balance charge transfer at the electrochromic working electrode during the optical switching. The double injection of ions and electrons can be used to describe the usual electrochromic process of V_2O_5 , the electrical double-layer phenomenon is used to store energy in electrochemical capacitors (ECs), often known as “supercapacitors.” Electrochemical double-layer capacitors (EDLCs) with a non-faradaic charge character and pseudocapacitors based on a faradaic electrochemical redox reaction are the two types of ECs. V_2O_5 has received an interest among transition-metal oxides used as ECs electrodes due to its pseudocapacitive properties, broad oxidation states, and high specific capacitance [1–5]. A wide variety of chemical and physical deposition techniques has been employed for fabricating the V_2O_5 thin films. Zahid Ali et al. [6] have studied in which the direct current (DC) magnetron sputtering was used to create zinc oxide coatings on a silicon substrate. The goal of this study was to see how the Ar:O₂ ratio affected the film’s crystal structure, surface morphology, electrical, and optical properties. The structural characterization revealed the hexagonal ZnO films that were orientated preferentially along the (002) plane. During the reactive sputtering process, the ZnO (002) peak got more intense and narrow as the amount of Ar increased. The increased sputtering of Zn from its target was linked to increased surface diffusion of adatoms on the substrate, which improved the crystallinity of the films with increasing Ar quantity. The decrease in band gap was attributed to a decrease in oxygen vacancies due to improved crystallinity in the films. At higher argon concentrations than oxygen, the electrical resistivity was reduced due to a reduction in structural defects. However, a fundamental step of these employed techniques is a finding of the appropriate conditions to fabricate the V_2O_5 films with reproducible phase composition and morphology. This task can be readily solved with the radio frequency magnetron sputtering yielding a film uniformity over a substrate area with a reasonable deposition rate [7].

Dwight Acosta et al. [8] have reported that the magnetron sputtering in a vacuum and an O₂ environment on glass and FTO substrates produced the V_2O_5 in thin-film configurations. This result showed that larger grains occurred in samples grown in an O₂ atmosphere, which was thought to be connected to changes in optical transmittance and electrical conductivity parameters. When V_2O_5 samples were heated to roughly 255 °C, a sudden shift in electrical resistivity was detected, which was linked to a metal-semiconductor transition. To further clarify the effect of O₂ flow rate on the local-crystal structure of the V_2O_5 thin-film, so this work aims to observe the change in

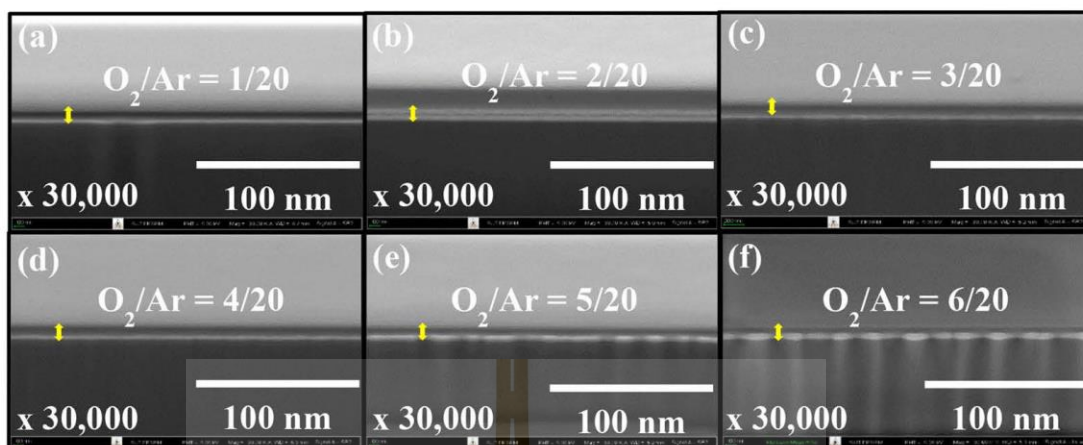


Figure 2. SEM cross-section images of vanadium oxide thin films at O_2/Ar flow rate of (a) 1/20, (b) 2/20, (c) 3/20, (d) 4/20, (e) 5/20 and (f) 6/20 (in sccm unit).

spectroscopy (EDS) (JEOL JSM-6010LV) and atomic force microscope (AFM) (Park Systems AFM XE-120). The local structure was characterized by synchrotron-based XANES and EXAFS spectra at the SUT-NANOTEC-SLRI XAS Beamline (BL 5.2) at the Synchrotron Light Research Institute (Public Organization), Thailand.

3. Results and discussion

3.1. The films morphology

Figure 1 showed the AFM images of vanadium oxide thin films at the O_2/Ar flow rate of (a) 1/20, (b) 2/20, (c) 3/20, (d) 4/20, (e) 5/20, and (f) 6/20 (in sccm unit). The surface roughness of prepared films with the O_2/Ar flow rate of 3/20, 4/20, 5/20, and 6/20 (in sccm unit) is higher than that of 1/20 and 2/20 (in sccm unit) because an increase of the working gas flow rate is thought to boost the energy flux at the substrate, which could contribute to a faster deposition rate and larger grain growth [9].

The SEM cross-section images and EDS spectra of vanadium oxide thin films with the O_2/Ar flow rate of (a) 1/20, (b) 2/20, (c) 3/20, (d) 4/20, (e) 5/20, and (f) 6/20 (in sccm unit) were shown in Figures 2 and 3, respectively. From the SEM cross-section images, the average thickness of the films was approximately 152.59 nm because the sputtering duration was kept constant at 80 minutes, so the average thickness of films was considerably equal.

From the EDS results, V and O signal was clearly observed indicating an existence of V and O atoms in the films. It should be noted that the samples are composed of only two elements (vanadium and oxygen). The atomic and weight ratios of O/V of the films with all conditions were shown in Table 1. The film with the O_2/Ar flow rate of 3/20 (in sccm unit) possessed an atomic and weight ratio of 2.29 and 0.72, respectively, which are very close to those O/V ratios of V_2O_5 [10].

As seen from Table 1, higher concentrations of O_2 gas resulted in a drop in deposition rate due to a decrease in the sticking coefficient. Furthermore, as the O_2 concentration rose, the argon gas pressure fell, obstructing the passage of argon ions toward

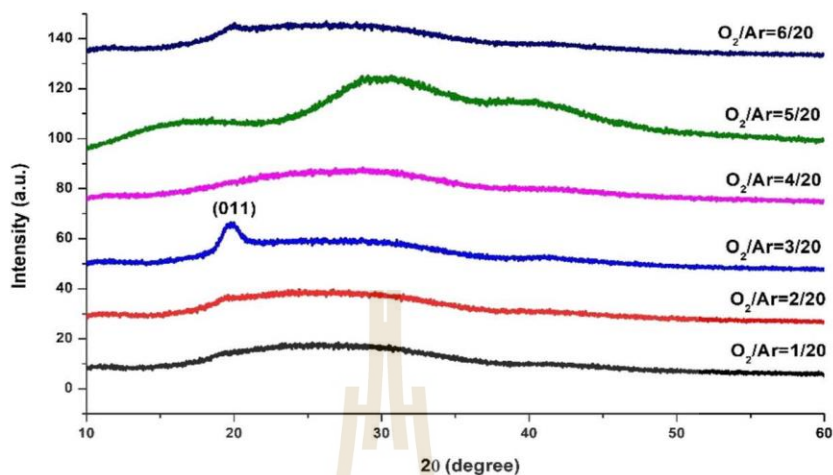


Figure 4. X-ray diffraction patterns of vanadium oxide thin films at the O_2/Ar flow rate of 1/20, 2/20, 3/20, 4/20, 5/20, and 6/20 (in sccm unit).

3.3. Local structure of V_2O_5 thin films

A majority vanadium oxide phase can be used to study the electronic structure and local structure around V atoms using the XAS technique. Figure 5 showed the normalized V K-edge XANES spectra and their first derivatives of the O_2/Ar flow rate of 1/20, 2/20, 3/20, 4/20, 5/20, and 6/20 (in sccm unit) thin-film, V-foil, V_2O_3 , and V_2O_5 standard samples. The characteristic absorption edge of V existed at 5465 eV, which corresponds to the energy required to eject a core electron from a vanadium atom. The most intense peak near 5464–5469 eV [13–16] deconvoluted from XANES showed that the films contained the V^{3+} and V^{5+} with the oxidation states of 3+ and 5+ (from Linear combination fit in Table 2.) [17–18]. Since the deposited VO_x was a mix of vanadium oxide phases. The white line peaks observed in XANES spectra referred to the electronic $1s \rightarrow 3d$ transitions, whereas the broad peaks around 5490 eV came from the $1s \rightarrow 4p$ transition [19]. So, the O_2/Ar flow rate obviously affected the oxidation state of vanadium oxide thin films. As mentioned previously, the XANES results were used for the study of oxidation state of vanadium thin films at the O_2/Ar ratio of 1/20, 2/20, 3/20, 4/20, 5/20, and 6/20 (in sccm unit). The plots showed that, vanadium thin films contained the $1s \rightarrow 3d$ transition peak (around 5464–5469 eV) and the $1s \rightarrow 4p$ transition peak (around 5490 eV) at all O_2/Ar ratios (as seen in Figure 5(c)) depicting that the crystal structure of V_2O_5 (V^{5+}) was orthorhombic wurtzite. From Figure 6, the O_2/Ar ratio of 1/20 (in sccm unit) revealed the lowest intensity at the $1s \rightarrow 3d$ transition peak compared to the others. By increasing the O_2/Ar ratio to 2/20 (in sccm unit), the $1s \rightarrow 3d$ transition peak intensity increased. The increase in an intensity of $1s \rightarrow 3d$ transition peak is attributed to the development of the V_2O_5 (V^{5+}) formation. Similarly, when O_2/Ar ratio increased to 3/20–6/20 (in sccm unit), the $1s \rightarrow 3d$ transition peak's intensities further increased comparative to that of 1/20 ratio. Especially, focusing on the O_2/Ar ratio of 3/20 (in sccm unit), this condition performed the highest intensity peak of the $1s \rightarrow 3d$ transition. This implies to the strongest enhancement in the vanadium metal form to V_2O_5 (V^{5+}). The sample with an O_2/Ar flow rate of 1/20 (in sccm unit) was made up

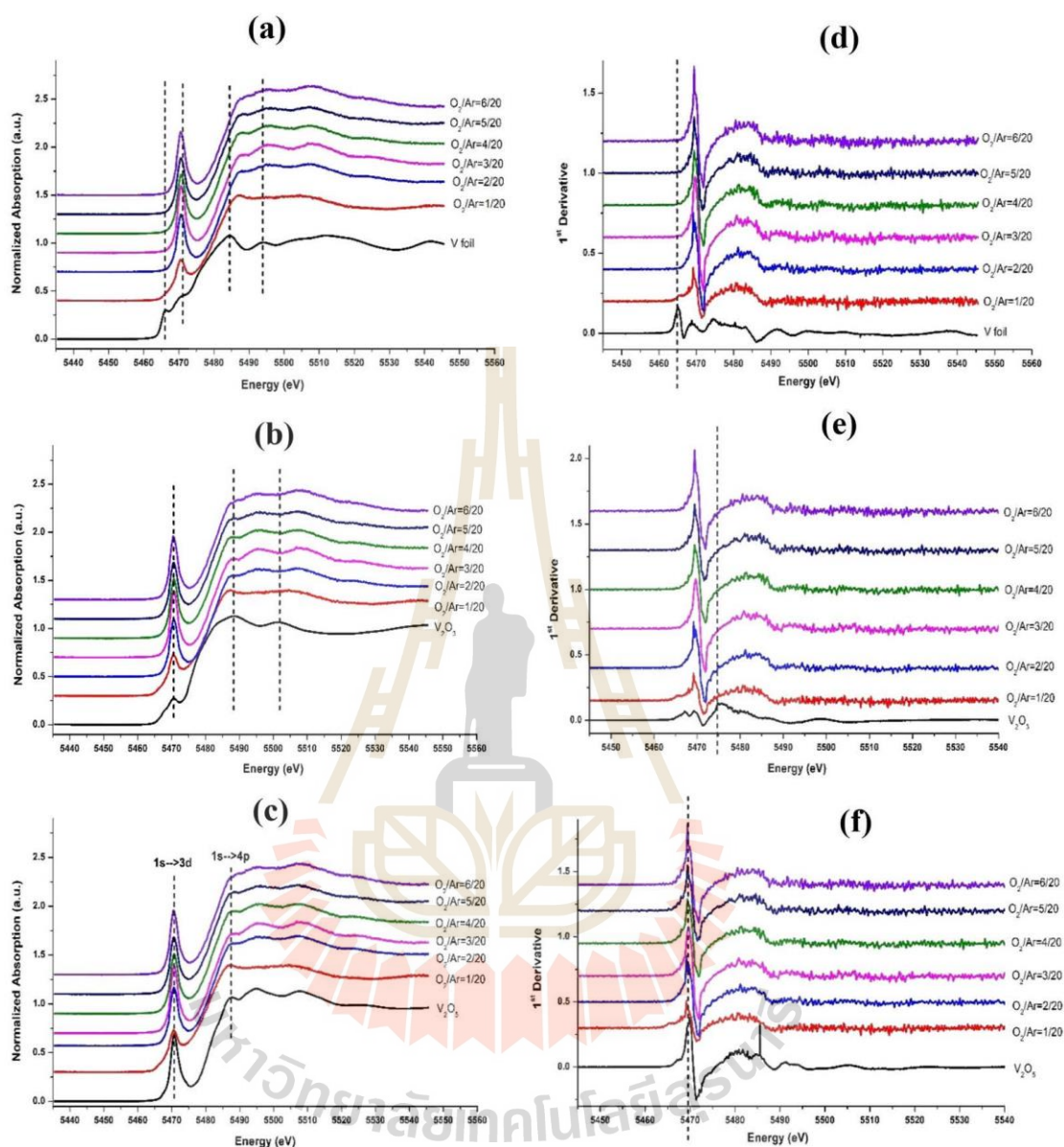


Figure 5 Normalized V K-edge XANES spectra (a–c) and the corresponding first derivatives (d–f) of vanadium oxide thin films at the O_2/Ar flow rate of 1/20, 2/20, 3/20, 4/20, 5/20, and 6/20 (in sccm unit) with V-foil, V_2O_3 , and V_2O_5 standard samples [12].

Table 2. Linear combination fit of R-factor, % V_2O_3 , and % V_2O_5 of vanadium oxide thin films at different O_2/Ar flow rates.

O_2/Ar flow rate (in sccm unit)	R-factor	% V_2O_3	% V_2O_5
1/20	0.0024125	55.8	44.2
2/20	0.0026809	4.6	95.4
3/20	0.0041960	0	100
4/20	0.0018633	3.9	96.1
5/20	0.0039409	4.8	95.2
6/20	0.0106780	0	100

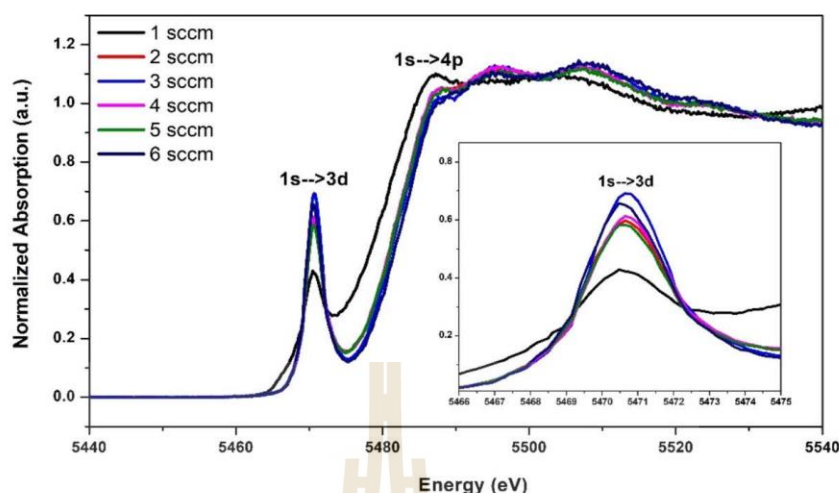


Figure 6 Normalized V K-edge XANES spectra of vanadium oxide thin films at the O_2/Ar flow rate of 1/20, 2/20, 3/20, 4/20, 5/20, and 6/20 (in sccm unit).

of a mix of amorphous V_2O_5 and V_2O_3 , whereas the rest was made up entirely of amorphous V_2O_5 , except the 3/20 ratio condition which had the highest crystallinity. An increase of O_2 flow rate is highly believed of causing an increase in energy flux and enlargement of the $1s \rightarrow 3d$ transition peak's intensity at the substrate, which can lead to a higher deposition rate. Therefore, to achieve a desired V_2O_5 structure, the gas flow rate would be adjusted to accomplish. The sole XANES results were not able to provide deeply information on the local structure of vanadium oxide. The peak near 5464–5469 eV [20] could be due to a mixture of several coordinations or a rather large distribution of crystal fields around vanadium [21]. This suggests a significant change in V local structure especially for coordinated oxygen atoms surrounding V atom. This would be further discussed in the EXAFS section.

In order to understand the local environment of V atoms in the structure, the EXAFS spectra were intensively analyzed and fitted using Athena and Artemis programs as implement in the IFEFFIT packages [9, 15]. The EXAFS spectra of the corresponding Fourier transform (FT) in R space at V K-edge of all samples were shown in Figure 7. It can be seen that the amplitudes of V–O and V–V peaks were not significantly different. These patterns can be identified as the V_2O_5 orthorhombic structure as they were best fitted with the V_2O_5 model with a good R-factor (good R-factor for fitting is between 1–5%) . In addition, the investigation of structural parameters of the local environment around the V atom was analyzed based on FT fitting. Plots of V K-edge K^3 weighted Fourier transform fitting from the experiment (red line) and fitted line (black circle) of all vanadium oxide thin films were shown in Figure 7. The FT provided information on the partial atomic distribution around the V atoms in the V_2O_5 system. For the sample with the O_2/Ar flow rate of 2/20, 3/20, 4/20, 5/20, and 6/20 (in sccm unit), the resulting filtered data and wavenumber in a range of 2–9 Å were shown in Figure 7 [22]. The FT spectra of R space showed that the single scattering contributions from the location of four V–O shells and the next location of two V–V shells were determined [23]. The V–O and V–V models of the V_2O_5 orthorhombic structure were used for the fit. The parameters of the EXAFS fitting such as interatomic distances (R),

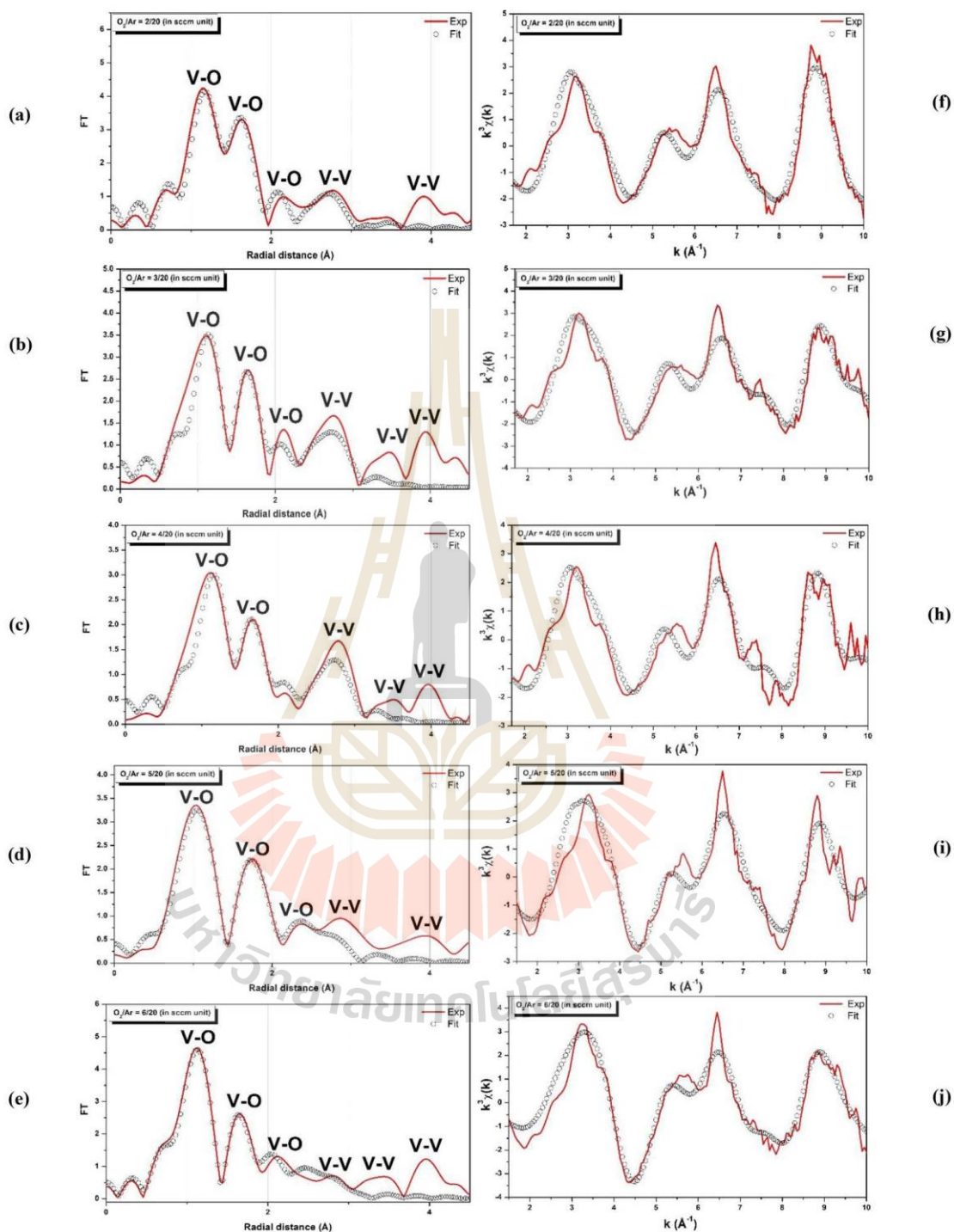


Figure 7. Fourier transform of EXAFS spectra at V K-edge (left) obtained from the experiment (red line) and fitting (black circle) of vanadium oxide thin films at the O_2/Ar flow rate of (a) 2/20, (b) 3/20, (c) 4/20, (d) 5/20 and (e) 6/20 (in sccm unit) and k^3 -weighted EXAFS data (right) of vanadium oxide thin films at the O_2/Ar flow rate of (f) 2/20, (g) 3/20, (h) 4/20, (i) 5/20 and (j) 6/20 (in sccm unit).

Table 3. EXAFS fitting parameters of interatomic distance (R), coordination number (N), Debye-Waller factor (σ^2), and amplitude reduction (S_0^2) of O₂/Ar flow rate at 2/20, 3/20, 4/20, 5/20, and 6/20 (in sccm unit).

Sample	Shell	N	σ^2	R(Å)	R-factor	S_0^2
2/20 (in sccm unit)	V-O	1	0.00090	1.62346	2.42%	0.70
	V-O	1	0.00102	1.83479		
	V-O	2	0.00569	1.95214		
	V-O	1	0.00718	1.61986		
	V-V	2	0.01316	3.12490		
	V-V	1	0.01432	3.40020		
5/20 (in sccm unit)	V-O	1	0.00112	1.51349	3.32%	0.850
	V-O	1	0.00127	1.71048		
	V-O	2	0.00296	1.91254		
	V-O	1	0.00313	1.66504		
	V-V	2	0.01581	3.06517		
	V-V	1	0.01720	3.33522		
3/20 (in sccm unit)	V-O	1	0.00300	1.59091	4.18%	0.70
	V-O	1	0.00339	1.79799		
	V-O	2	0.00607	1.92997		
	V-O	1	0.00766	1.63959		
	V-V	2	0.01034	3.10404		
	V-V	1	0.01125	3.37750		
4/20 (in sccm unit)	V-O	1	0.00427	1.61004	3.86%	0.7
	V-O	1	0.00483	1.81962		
	V-O	2	0.00745	1.95514		
	V-O	1	0.00940	1.62942		
	V-V	2	0.01052	3.10334		
	V-V	1	0.01145	3.37675		
6/20 (in sccm unit)	V-O	1	0.00311	1.58977	1.60%	0.98
	V-O	1	0.01005	1.55009		
	V-O	2	0.01106	1.82494		
	V-O	1	0.01600	2.32811		
	V-V	2	0.01700	3.04011		
	V-V	1	0.01750	3.35546		

Debye-Waller factors (σ^2), amplitude reduction (S_0^2), and R-factor are shown in Table 3 [24]. In the special case at 1/20 of O₂/Ar flow rate (in sccm unit) sample, EXAFS data was not fitted by Artemis programs because the unit cell of 1/20 of O₂/Ar condition (in sccm unit) was combined by the 55.8% V₂O₃ and 44.2% V₂O₅ (from Linear combination fit). Additionally, the EXAFS fitting data of the 2/20–6/20 of O₂/Ar flow rate (in sccm unit) samples implied and supported the XANES results for the structural environment around V atoms in the V₂O₅ orthorhombic structure. A local structure was discovered to be affected directly by the flow rate of O₂/Ar gas. Increasing the O₂/Ar gas flow rate is thought to enhance energy flux at the substrate, which might contribute to a faster deposition rate.

4. Conclusions

In this study, vanadium oxide thin films were prepared by RF-magnetron sputtering from the V-metal target. The effect of O₂/Ar ratio on the local structure was investigated in terms of vanadium oxide films by varying an O₂ flow rate at 1–6 sccm and fixing Ar flow rate at 20 sccm. The AFM and EDS spectra results showed that the surface roughness of prepared films with the O₂/Ar flow rate of 3/20, 4/20, 5/20, and 6/20 (in sccm unit) was higher than that of 1/20 and 2/20 ratio (in sccm unit) and the film with

the O₂/Ar flow rate of 3/20 (in sccm unit) possessed the atomic and weight ratio of 2.29 and 0.72, respectively, very close to the O/V atomic and weight ratio of V₂O₅. From XRD results, the V₂O₅ phase was identified. It was further confirmed by the XANES and EXAFS fitting results. The XANES spectra at the V K-edge showed that the prepared films contained the oxidation state of V³⁺ and V⁵⁺. By increasing the O₂/Ar ratio, the 1s→3d transition peak intensity increased. The increase in an intensity of 1s→3d peak is attributed to the development of V₂O₅ (V⁵⁺) formation. Additionally, the EXAFS data implied and supported the XANES results for the structural environment around V atoms in the V₂O₅ orthorhombic structure. As a result, it was discovered that the flow rate of O₂/Ar gas could affect the deposition rate of RF-sputter systems on a local structure. Increasing the O₂/Ar gas flow rate is thought to enhance the energy flux at the substrate, which might contribute to a faster deposition rate. When there are additional constraints, such as a fixed sputtering power or working gas pressure, the gas flow rate can be adjusted to create the desired V₂O₅ structure. Furthermore, chamber evacuation maximum throughput capabilities must be considered for the range in which the working gas flow rate will be adjusted in order to obtain a better control of sputtering chamber conditions.

Acknowledgments

We would like to acknowledge Thailand Research Fund, Suranaree University and Technology (SUT), the Synchrotron Light Research Institute (Public Organization) (BL5.2), Thailand for the XAS facilities and Science Achievement Scholarship of Thailand (SAST) for financial support.

References

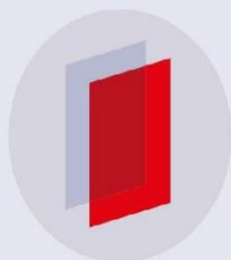
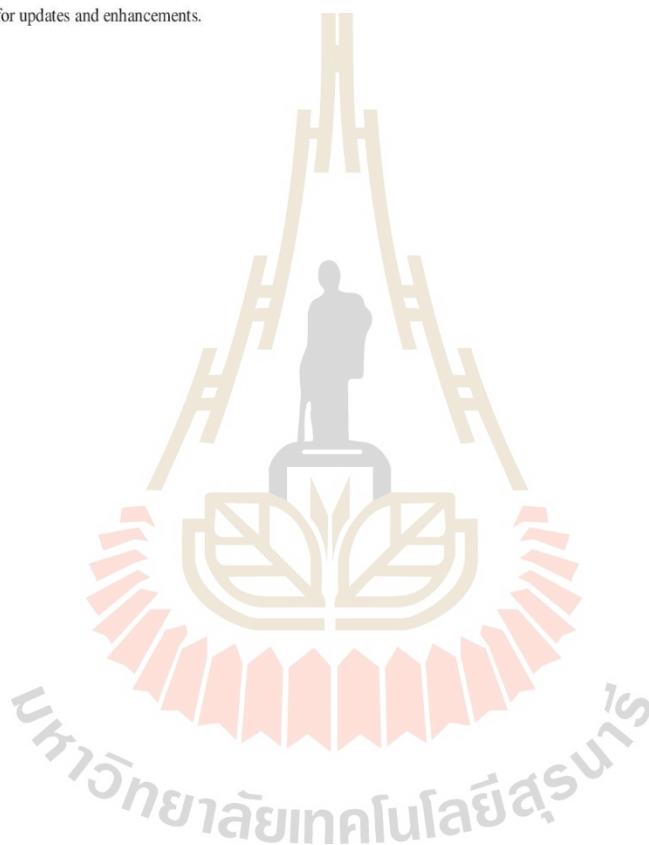
- [1] D. Aurbach *et al.*, Prototype systems for rechargeable magnesium batteries, *Nature* **407** (6805), 724 (2000). DOI: 10.1038/35037553.
- [2] N. G. Prakash *et al.*, Molybdenum doped V₂O₅ thin films electrodes for supercapacitors, *Mater. Today: Proc.* **3**, 4076 (2016). DOI: 10.1016/j.matpr.2016.11.076.
- [3] J. Wu *et al.*, A scalable free-standing V₂O₅/CNT film electrode for supercapacitors with a wide operation voltage (1.6 V) in an aqueous electrolyte, *Adv. Funct. Mater.* **26** (33), 6114 (2016). DOI: 10.1002/adfm.201601811.
- [4] M. A. Sutar *et al.*, Enhancing electrochemical performance of V₂O₅ thin film by using ultrasonic wetting, *IOSR-JAP.* **7**, 41–45 (2015). DOI: 10.9790/4861-07624145.
- [5] G. L. Sandhya *et al.*, Structural and supercapacitive performance of V₂O₅ thin films prepared by dc magnetron sputtering, *IOSR JAC.* **10** (05), 64 (2017). DOI: 10.9790/5736-1005026469.
- [6] A. Zahid *et al.*, Effect of Ar:O₂ ratio on reactively magnetron sputtered ZnO film's properties, *Mater. Res. Express* **6**, 116419 (2019). DOI: 10.1088/2053-1591/ab44b9.
- [7] A. Mauger and C. M. Julien, V₂O₅ thin films for energy storage and conversion, *AIMS Mater. Sci.* **5** (2), 349 (2018). DOI: 10.3934/matserci.2018.3.349.
- [8] D. Acosta *et al.*, V₂O₅ Thin films deposited by rf magnetron sputtering: the influence of oxygen content in physical properties, *Mater. Sci. Eng* **A6** (3–4), 81 (2016). DOI: 10.17265/2161-6213/2016.3-4.007.
- [9] A. Muntaser *et al.*, Effects of gas flow rate on the structure and elemental composition of tin oxide thin films deposited by RF sputtering, *AIP Adv.* **7**, 125105 (2017). DOI: 10.1063/1.5001883.

- [10] N. Kumagai *et al.*, Intercalation of lithium in r.f.-sputtered vanadium oxide film as an electrode material for lithium-ion batteries, *J. Appl. Electrochem.* **28** (1), 41 (1997). DOI: 10.1023/A:1003293617237.
- [11] Y. Chan *et al.*, Synthesis of V_2O_5 nanoflakes on PET fiber as visible-light-driven photocatalysts for degradation of RhB dye, *J. Catal.* **2014**, 1 (2014). DOI: 2014/370696. DOI: 10.1155/2014/370696.
- [12] P. Kidkhunthod *et al.*, A structural study and magnetic properties of electrospun carbon/manganese ferrite($C/MnFe_2O_4$) composite nano fibers, *J. Magn. Magn. Mater.* **401**, 436 (2016). DOI: 10.1016/j.jmmm.2015.10.085.
- [13] S. S. G. Mancini *et al.*, Structure of oriented V_2O_5 gel studied by polarized x-ray-absorption spectroscopy at the vanadium K edge, *Phys. Rev. B.* **40** (18), 12229 (1989). DOI: 10.1103/PhysRevB.40.12229.
- [14] O. Siper *et al.*, Geometric and electronic structure effects in polarized V K-edge absorption near-edge structure spectra of V_2O_5 , *Phys. Rev. B.* **60**, 14115 (1999). DOI: 10.1103/PhysRevB.60.14115.
- [15] J. Wong *et al.*, K-edge absorption spectra of selected vanadium compounds, *Phys. Rev. B.* **30** (10), 5596 (1984)., DOI: 10.1103/PhysRevB.30.5596.
- [16] B. Poumellec *et al.*, Experimental and theoretical studies of dipole and quadrupole contributions to the vanadium K-edge XANES for $VOPO_4 \cdot 2H_2O$ xerogel, *Phys. Rev. B.* **58** (10), 6133 (1998). DOI: 10.1103/PhysRevB.58.6133.
- [17] C. J. Patridge *et al.*, In-situ X-ray absorption spectroscopy analysis of capacity fade in nanoscale- $LiCoO_2$, *J. Solid State Chem.* **203**, 134 (2013). DOI: 10.1016/j.jssc.2013.04.008.
- [18] C. Ekwongsa *et al.*, Temperature dependent local structure of $LiCoO_2$ determined by in-situ Co K-edge X-ray absorption fine structure (EXAFS), *Radiat. Phys. Chem.* **175**, 108545 (2020). DOI: 10.1016/j.radphyschem.2019.108545.
- [19] M. Nabavi *et al.*, Structure and properties of amorphous V_2O_5 , *Philos. Mag. Lett.* **63** (4), 941 (1991). DOI: 10.1080/13642819108205549.
- [20] Z. Y. Wu *et al.*, Quadrupolar transitions and medium-range-order effects in metal K-edge x-ray absorption spectra of 3d transition-metal compounds, *Phys. Rev. B.* **70** (3), 033104 (2004)., DOI: 10.1103/PhysRevB.70.033104.
- [21] B. Ravel, and M. Newville, ATHENA, ARTEMIS, HEPHAESTUS: data analysis for X-ray absorption spectroscopy using IFEFFIT, *J. Synchrotron. Radiat.* **12** (Pt 4), 537 (2005). DOI: 10.1107/S0909049505012719.
- [22] R. Prins, and D. C. Koningsberger, X-ray absorption: Principles, applications, techniques of EXAFS, SEXAFS, XANES. <https://www.osti.gov/biblio/5927479>(1988).
- [23] G. G. Li, F. Bridges, and C. H. Booth, X-ray-absorption fine-structure standards: A comparison of experiment and theory, *Phys. Rev. B.* **52** (9), 6332 (1995). DOI: 10.1103/PhysRevB.52.6332.
- [24] A. N. Mansour *et al.*, In situ XAS investigation of the oxidation state and local structure of vanadium in discharged and charged V_2O_5 aerogel cathodes, *Electrochim. Acta* **47** (19), 3151 (2002). DOI: 10.1016/S0013-4686(02)00234-7.

PAPER • OPEN ACCESS**The controller and monitoring system of 1-10 kV high voltage powersupply**

To cite this article: B Angmanee *et al* 2018 *J. Phys.: Conf. Ser.* **1144** 012146

View the [article online](#) for updates and enhancements.

**IOP | ebooks™**

Bringing you innovative digital publishing with leading voices to create your essential collection of books in STEM research.

Start exploring the collection - download the first chapter of every title for free.

The controller and monitoring system of 1-10 kV high voltage power supply

B Angmanee¹ C Ekwongsa² and A Thedsakhulwong^{1*}

¹ Department of Physics, Faculty of science, Ubon Ratchathani University, 85, Sathonlamark Rd. Warinchamrab, Ubon Ratchathani, 34190, Thailand

² School of Physics, Suranaree University of Technology, 111, University Rd, Muang Nakhon Ratchasima, Nakhon Ratchasima 30000, Thailand

*Email: amorn.t@ubu.ac.th

Abstract. The controller and monitoring system of 1-10 kV high voltage power supply was developed. The system composed of an Arduino mega 2560 microcontroller boards, a digital to analog conversion (DAC) part, a high voltage module and the designed software on a personal computer. The software was developed by LabVIEW software for controlled the high voltage module and displayed the high voltage values. The microcontroller board used for the digital data transmission to the DAC part and converted the high voltage value to digital data for monitoring. The DAC part generated the analog signal from a board for adjusting a high voltage value of a module. The completed system can be controlled the high voltage and the real-time monitored the high voltage value of a module with the resolution of 2.5 V. The error of actual high voltage values with the setting one was maximum of 5%

1. Introduction

The high voltage (HV) applications have received a lot of attention over the years. It is well known that high voltage power can cause electric fields [1], [2]. Based on research in biology, the researchers introduced high voltage to study the effects of E. coli bacteria on living under the electric field of 4 kV/cm [3]. In engineering research, high voltage has been used to study the distribution of diamond particles for grinding and abrasive coatings that using a high voltage of 6 kV, which results in a more uniform distribution than the conventional ones [4]. In addition, the research on the agricultural thread has introduced high voltage to study the condition of eggs, which use the electric field from 30 kV/m, 60 kV/m and 90 kV/m [5]. And recently, the study of materials science has studied the properties of materials that change under the power of electric fields in the range of 700 V/mm to 2 kV/mm, which stimulate materials by synchrotron light sources in the energy range of x-ray. Some properties of the material change [6], [7]. However, the inaccuracies and the precision in these researches are the handlings of high voltage control systems. In this paper, we focus on studying and creating high voltage generators that provide precise voltage control that can be controlled and monitored on a computer. In our experiment, we used the Arduino Mega 2560 board for the interface and developed the control system with LabVIEW software. We can control the high voltage generator in the range of 1 kV to 10 kV so that it can be applied to other research. To be more precise. The experimental details are shown in Part 2, the analysis and discussions are shows in part 3, and the summary is shown in Part 4.



2. Experimental

2.1 The circuit designing

In generating the high voltage, we used the module for high voltage generators and connected to the Arduino mega 2560 control board. The circuit shown in Figure 1 is a circuit specially designed for high voltage generation. Figure 1(a) Show about the Arduino mega 2560 is used to connect to computers and electronic circuits. Figure 1(b) show about the digital to analog converter circuit (DAC) MCP4922 is used to convert the signal from the board. Figure 1(c) are amplifier circuit (non-inverting amplifier circuit) LM358. Figure 1(d) drives the current circuit (P55NF06) and Figure 1(e) is high voltage module.

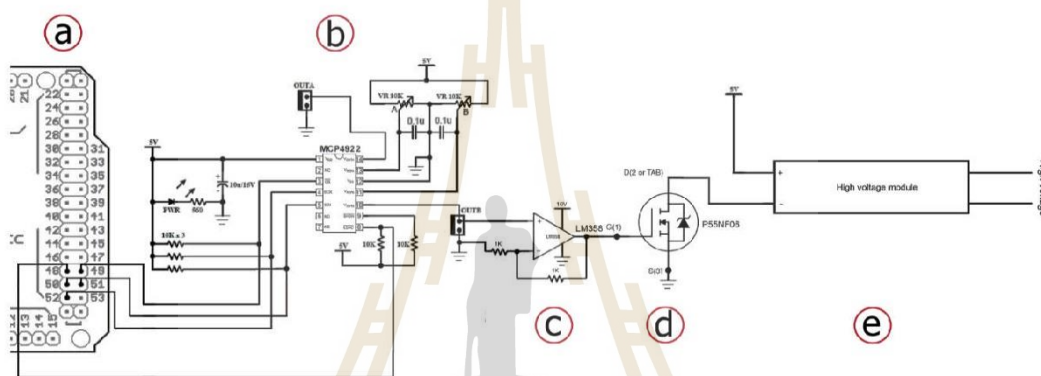


Figure 1. The high voltage circuit parts **a)** an Arduino mega 2560 board **b)** Digital to analog converter circuit (DAC) MCP4922 **c)** an amplifier circuit **d)** a current driver circuit (P55NF06) and **e)** the high voltage module.

The high voltage values were adjusted by varies the digital value in the application on a computer. The Arduino board received the data and transmit to DAC circuits then convert to analog form. The signals were amplified by an amplifier circuit for drives the high voltage module by a driver circuit. The appearance high voltage values were monitored by the high voltage probe and collected by the program on a computer via the Arduino board as shown in Figure 2.

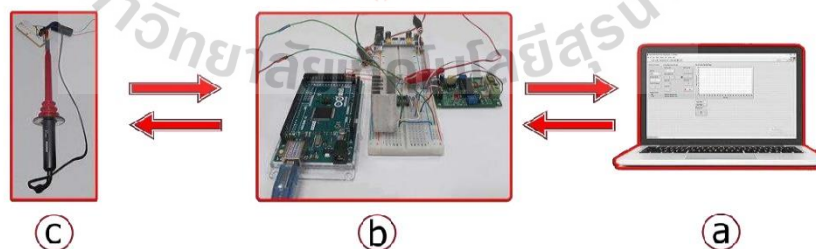


Figure 2. The controller and monitoring system **a)** the computer used for controls and collects the data. **b)** The electronic circuit part. **c)** The high voltage output and the high voltage probe.

2.2 The software designing

The development of control systems using the LabVIEW software (Home Edition) interface with Arduino board. The control is divided into two parts, as part of the development of the application program for processing LINX applications and part of a window for control, parameter setting, and display in high voltage generators.

3. Results and Discussion

The program development is divided into the two-part with the part of the controlling panel and the part of the program processing panel. Shown in Figure 3.

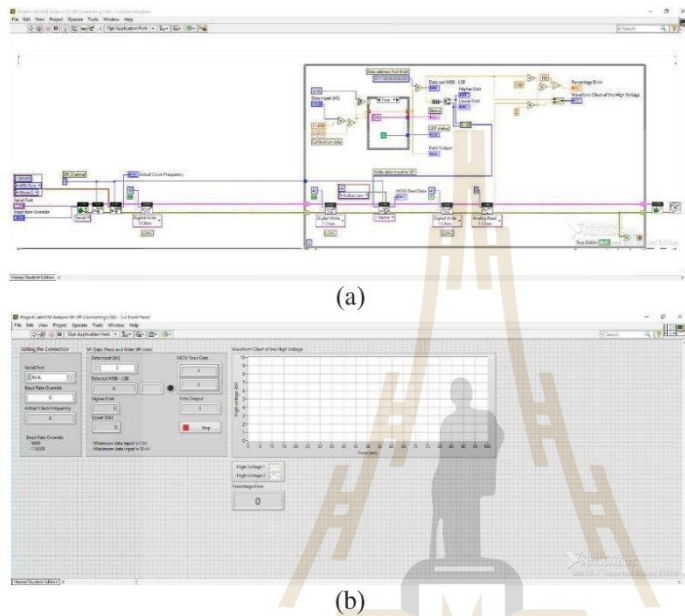


Figure 3. Shown about the development program of the panel on the computer control system. a) The panel of the processing program is used to send and receive the data with the electronic circuit part. b) The panel of the monitoring is used to set the parameter to generate the high voltage and to display the data from generating.

The digital data transmission from the Arduino board to DAC via the SPI bus with 16-bit data transfer. Figure 4 shown the comparison of SCLK and MOSI waveform with the various data.

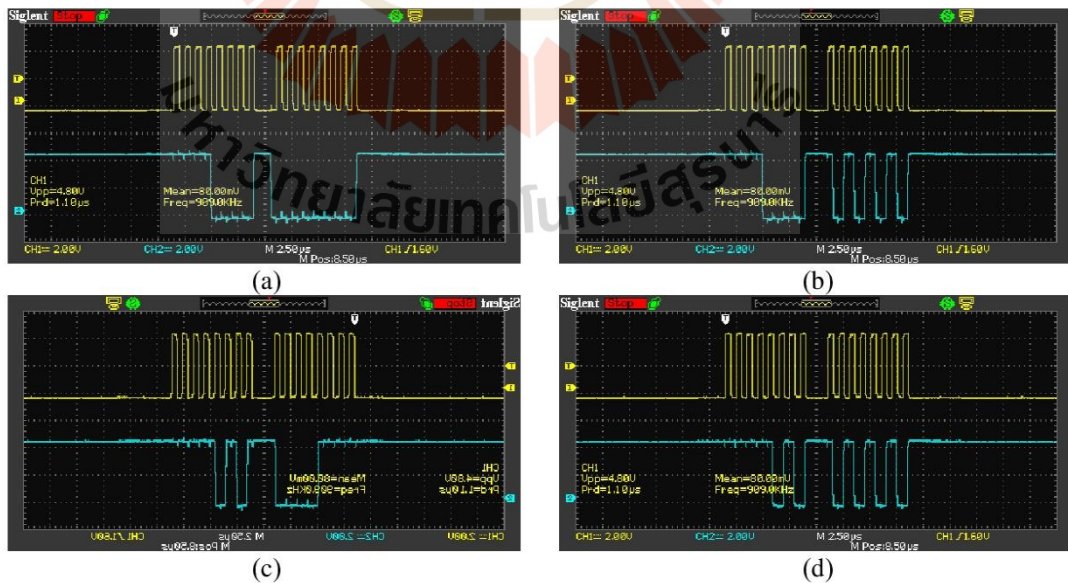


Figure 4. characteristics of digital signals, the clock signal is measured by a 16 bit oscilloscope a) send digital information to 1111 0000 0000 0000 b) Send digital information to 1111 0000 1010 1010 c) send digital information to 1111 0000 1010 0000 And d) send digital information to 1111 1010 1010 1010.

Figure 5 shown the relation between the digital values and the DAC output voltage. The analog output was linearity with the $R^2 = 1$ and 1.22 mV/bit resolution. The results have shown that the analog output can be adjusted by the developed program on a computer.

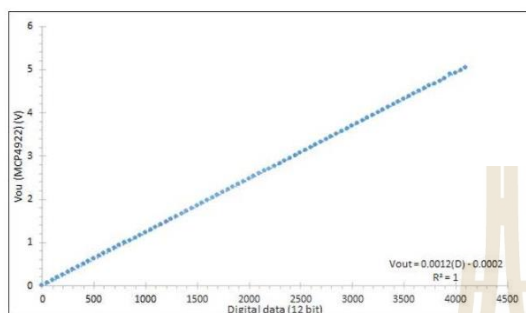


Figure 5. The relation between the digital values and the DAC output voltage.

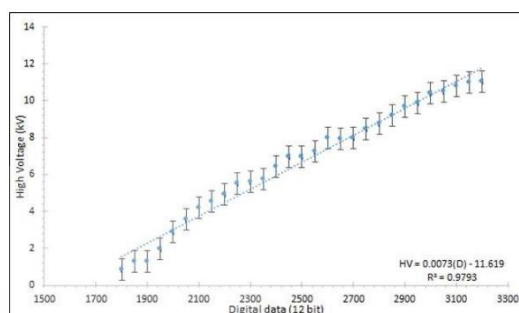


Figure 6. The relation between the digital value and the high voltage output of the high voltage module.

Figure 6 shown the relation between the digital value and the high voltage output of the high voltage module. The high voltage value can be varied in the range of 1 - 10 kV with the input digital values in the range of 0 - 1700. The high voltage output closely linear with the $R^2 = 0.9793$ and the 2.5 V/bit resolution. The appearance high voltage value can be monitored by the probe and displayed in the developed program on a computer. The error has occurred over this digital range was 5% maximum.

4. Conclusion

In this work, the high voltage is generated from a high voltage module in the range of 1 kV to 10 kV. The error was occurred over this digital range was 5% maximum. In the controller used the developed program on a computer for connection to an Arduino mega 2560 board and an electronic circuit. The high voltage values can be varied and real-time monitoring with the program.

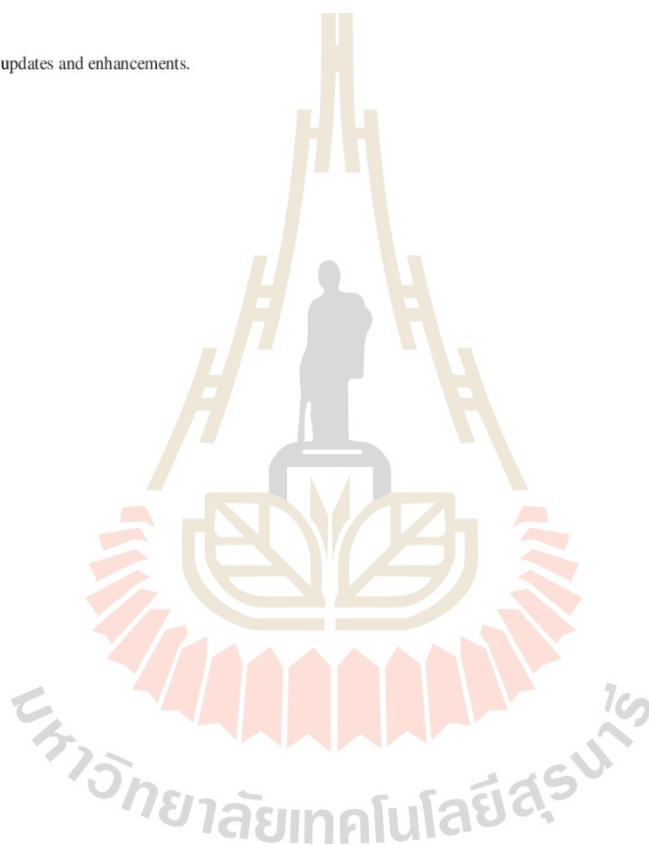
References

- [1] Jackson J D 1962 *Classical Electrodynamics* chapter 1 p 1-44
- [2] Edminister J A 1993 *Electromagnetics* vol 2 chapter 1-8 p 1-134
- [3] Aizhi B, Ruiyun L, Xinyu W, Xiaowei Y and Hongjian Y 2016 *High Voltage Engineering* **42** 2534-2539
- [4] Chen F, Zhang L, Yin S, Huang S, Tang Q 2018 *The International Journal of Advanced Manufacturing Technology* **96** 1393-1401
- [5] Guibao S, Xinxin W and Guodong P 2009 *Transactions of the CSAE* **25** 318-323
- [6] Kempet W, Marungsri B, Yimnirun R, Klysubun W, and Pojprapai S 2013 *Ferroelectrics* **453** 106-112
- [7] Kempet W, Marungsri B, Yimnirun R, Klysubun W, Fangsuwannarak T, Rattanachan S, Pisitpipathsin N, Promsawat M and Pojprapai S 2016 *Ferroelectric* **492** 35-42

PAPER • OPEN ACCESS**Development of the PID controller and real-time monitoring system for low-temperature furnace**

To cite this article: T Pangya *et al* 2018 *J. Phys.: Conf. Ser.* **1144** 012160

View the [article online](#) for updates and enhancements.

**IOP ebooks™**

Bringing you innovative digital publishing with leading voices to create your essential collection of books in STEM research.

Start exploring the collection - download the first chapter of every title for free.

Development of the PID controller and real-time monitoring system for a low-temperature furnace

T Pangya¹, A Thedsakhulwong^{1*} and C Ekwongsa²

¹Department of Physics, Faculty of science, Ubon Ratchathani University, Warinchamrap, Ubon Ratchathani, 34190, Thailand

²School of Physics, Institute of science, Suranaree University of Technology, Mung, Nakhon Ratchasima, 30000, Thailand

*Email: amorn.t@ubu.ac.th

Abstract. The PID controller and real-time monitoring system for a low-temperature furnace was developed. The system has two parts, the PID controller, and the real-time monitoring part. An Arduino mega2560 microcontroller board was used for measuring and controlling the furnace temperature. A type-K thermocouple and a MAX31850 IC were applied for a furnace temperature measurement. The microcontroller board and a MAX31850 were connected via the One-wire bus to convert the temperature values and send them to a personal computer. The PID parameters can be varied by a user in the program, which was developed by LabVIEW Software on a computer. The laboratory-made furnace was established for testing the controller and monitoring system. The results have shown that the temperature with the range of 25-500 degree Celsius can be controlled. By the trial and error method with the PID parameters, k_p was 250, T_i was 0.05 and T_d was 0.20, the target temperature can be controlled with the maximum error of 1 degree Celsius.

1. Introduction

The temperature controller is a necessity in research on the thermal properties of substances. There are many types of research that have been conducted previously using temperature controller systems. Such as the effect of heating rate on structural and functional properties of wheat and potato starch-water systems in food science technology [1]. The investigation of the effect of each temperature-dependent material property on the transient temperature, residual stress and distortion of the welding process [2] and examples of research that use high-temperature control. Such as the high-temperature ablation properties of NANO zirconia reinforced fused silica ceramic [3]. In materials process technology, all of the above require the high resolution of the temperature controller and monitoring system.

The Proportional Integral Derivative (PID) Controller is the most common method for the temperature control system design. The heat treatment furnace in the industrial, which used Intelligent Fuzzy Logic and PID controllers to design of temperature controller [4]. Recently, the LabVIEW program applied to design PID control systems [5] and the PID temperature autotuning control design can be accomplished by using LabVIEW [6].



This research has development of the PID temperature control system and real-time temperature monitoring Using LabVIEW interface for Arduino. The temperature measured with sensor MAX31850 Communication with the master microcontroller over the 1-Wire bus. Read temperature data from a sensor with Arduino MEGA2560. Then we get temperature data from Arduino and real-time temperature monitoring with the LabVIEW software. In this research design of PID temperature control by Ziegler Nichols and trial error method.

2. Experimental

2.1 Hardware design.

The system composes of the temperature measurement and the Arduino microcontroller board. The furnace temperature was measured by the thermocouple amplifier with 1-wire breakout Board-MAX31850K. The Arduino board read the temperature data and send to display on a computer via USB port. The target temperature maintains by on/off a solid state relay (SSR) which controls the period with the Arduino. The diagram of the system shows in Figure 1.

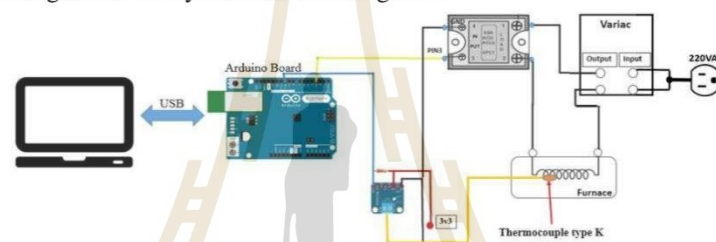


Figure 1. The diagram of the PID controller and real-time monitoring system.

2.2 Software design.

The PID parameters setting can be varies and real time temperature monitoring can be shows on the front panel of the developed program, respectively. The front panel of the temperature control system designed shows in Figure2.

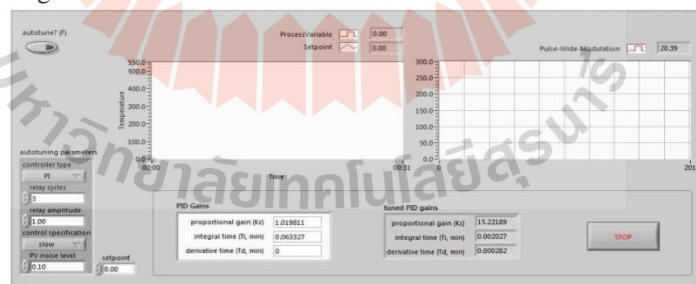


Figure 2. The front panel of the temperature controller

The block diagram of PID control program shows in Figure 3. The program read the furnace temperature from the Arduino and real time display in the front panel. The period for on/off the SSR accumulates from the PID parameters and send to the Arduino for on/off the SSR. The target temperature and the various PID parameters are the input parameter of the program. The Ziegler Nichols function from equation (1) used to calculate the output of signal and the trial and error used to find optimizes parameter of this system. Where K_p , T_i and T_d is Parameter of proportional, integral and Derivative respectively

$$U = K_p \left(1 + \frac{1}{T_i} \int T_d \right) \quad (1)$$

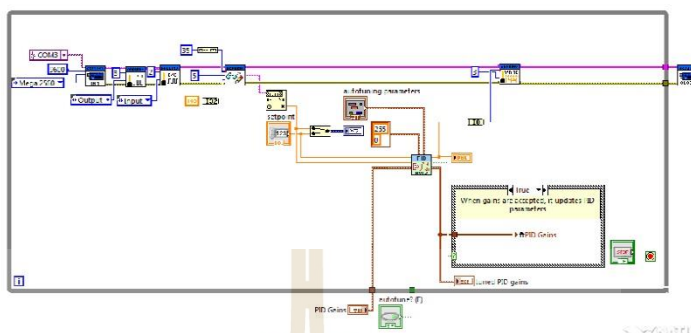


Figure3. Block diagram of PID control from LabVIEW

3.Result and discussion

The Ziegler Nichols function used to generates the output signal for controller. The PID parameter was varied by the trial and error method.

3.1 The K_p parameter optimization

Table 1. Shows the temperature settling value, the steady state error, and the overshoot where T_i was 0, T_d was 0 and the parameter K_p was varied the K_p has the effect on the settling and steady state error. The optimize K_p was 250.

Table1. List of comparisons of response parameter of all design K_p at $T_i = 0$, $T_d = 0$

Parameter	Settling value	Steady state error (°C)	Overshoot
$K_p = 50$	This temperature is below the setpoint at 3°C	± 6	No overshoots.
$K_p = 100$	This temperature is below the setpoint at 3°C	± 6	No overshoots.
$K_p = 150$	This temperature is below the setpoint at 2°C	± 5	No overshoots.
$K_p = 200$	This temperature little below the setpoint at 1°C	± 3	No overshoots.
$K_p = 250$	This temperature is oscillates around the setpoint at ± 2 °C	± 2	Overshoot is absorb

3.2 The T_i parameter optimization

Table 2. Show the rising time, the steady state error, and the overshoot temperature where the K_p was 250, the T_d was 0, and the T_i was varied. The results shown that the T_i has the effect of rising time and the oscillates of temperature. The optimize T_i value was 0.05.

Table2. List of comparisons of response parameter of all design T_i at $K_p = 250$, $T_d = 0$.

Parameter	Rising time (s)	Steady state error(°C)	Overshoot (°C)
$T_i = 0.05$	120	± 1	5
$T_i = 0.10$	155	± 2	5
$T_i = 0.15$	165	± 3	5
$T_i = 0.20$	185	± 4	5
$T_i = 0.30$	210	± 6	7

3.3 The T_d parameter optimization.

Table 3. Show the rising time, the steady state error, and the overshoot temperature where the K_p was 250, the T_i was 0.05, and the T_d was varied. The results shown that the least T_d has minimum rising time and the minimum oscillates was 1 °C with the T_d value was 0.20

Table3. List of comparisons of response parameter of all design Td at $Kp = 250$, $Ti = 0.05$

Parameter	Rising time (s)	Steady state error (°C)	Overshoot (°C)
$Td = 0.05$	120	± 3	4
$Td = 0.10$	180	± 2	3
$Td = 0.15$	195	± 2	3
$Td = 0.20$	180	± 1	2
$Td = 0.25$	180	± 2	4

The experiment shown that the optimize of the Kp parameter was 250, the Ti parameter was 0.05, and the Td parameter was 20.

3.4 Test the temperature control.

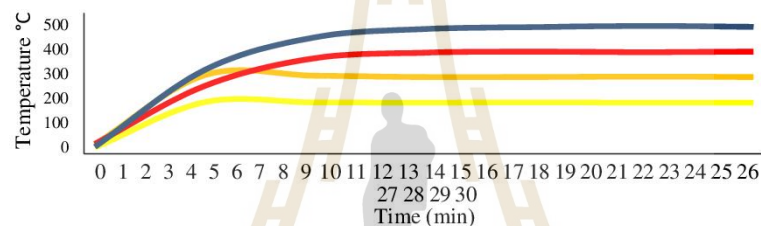


Figure 4. The various target temperature control with the optimized PID parameter.

The results shown that all of target temperature can be controlled with the maximum error of 1°C. The rising time of control was 270, 290, 720, and 1200 second with the target temperature 200°C, 300°C, 400°C, 500°C respectively.

4. Conclusion

In research, to developed and designed the PID temperature control which can be monitoring the temperature on the computer display. From experiments to find parameters of PID show that the best of Kp cause to the system response better and the output is a small steady-state error. The best Ti value cause to decrease the response of the system and the best Td cause to decrease overshoot of the system and increase the response of the system. By trial and error method with the PID parameters, Kp was 250, Ti was 0.05 and Td was 0.20. The experimental results of control temperature can be controlled to a stable temperature. The maximum error is 1°C and rising time of temperature 200°C, 300°C, 400°C, and 500°C was 270, 290, 720, and 1200 second respectively.

References

- [1] Mulumbaa P, Doranb L, Danthineb S, Bleckerb C and Mera F 2018 *Food science and Technology* **88** 196-202
- [2] Zhu XK and Chao YJ 2002 *Computer & Structures* **80** 967-976
- [3] Wan W, Luo J, Feng Y, Ouyang Y, Chen D and Qiu T 2018 *Ceramic International* **44** 7273-7275
- [4] Srinivasulu Raju S, Chaitanya Kumar R, Ravi K, Viswanath M 2013 *International J. Advanced Research in Computer Science* **4** 12-17
- [5] Muhammad Asraf H and Nur Dalila KA 2016 *J. Telecommunication, Electronic and Computer Engineering* **9** 53-57
- [6] Kumar S, Bhattacharyya J and Bhattacharyya M 2016 *International Research Journal of Engineering and Technology* **3** 341-345

Table 3. List of comparisons of response parameter of all design T_d at $K_p = 250$, $T_i = 0.05$

Parameter	Rising time (s)	Steady state error (°C)	Overshoot (°C)
$T_d = 0.05$	120	± 3	4
$T_d = 0.10$	180	± 2	3
$T_d = 0.15$	195	± 2	3
$T_d = 0.20$	180	± 1	2
$T_d = 0.25$	180	± 2	4

The experiment shown that the optimize of the K_p parameter was 250, the T_i parameter was 0.05, and the T_d parameter was 20.

3.4 Test the temperature control.

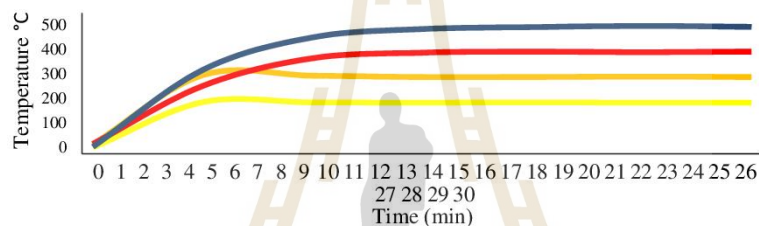


Figure 4. The various target temperature control with the optimized PID parameter.

The results shown that all of target temperature can be controlled with the maximum error of 1°C. The rising time of control was 270, 290, 720, and 1200 second with the target temperature 200°C, 300°C, 400°C, 500°C respectively.

4. Conclusion

In research, to developed and designed the PID temperature control which can be monitoring the temperature on the computer display. From experiments to find parameters of PID show that the best of K_p cause to the system response better and the output is a small steady-state error. The best T_i value cause to decrease the response of the system and the best T_d cause to decrease overshoot of the system and increase the response of the system. By trial and error method with the PID parameters, K_p was 250, T_i was 0.05 and T_d was 0.20. The experimental results of control temperature can be controlled to a stable temperature. The maximum error is 1°C and rising time of temperature 200°C, 300°C, 400°C, and 500°C was 270, 290, 720, and 1200 second respectively.

References

- [1] Mulumbaa P, Doranb L, Danthineb S, Bleckerb C and Mera F 2018 *Food science and Technology* **88** 196-202
- [2] Zhu XK and Chao YJ 2002 *Computer & Structures* **80** 967-976
- [3] Wan W, Luo J, Feng Y, Ouyang Y, Chen D and Qiu T 2018 *Ceramic International* **44** 7273-7275
- [4] Srinivasulu Raju S, Chaitanya Kumar R, Ravi K, Viswanath M 2013 *International J. Advanced Research in Computer Science* **4** 12-17
- [5] Muhammad Asraf H and Nur Dalila KA 2016 *J. Telecommunication, Electronic and Computer Engineering* **9** 53-57
- [6] Kumar S, Bhattacharyya J and Bhattacharyya M 2016 *International Research Journal of Engineering and Technology* **3** 341-345

CURRICULUM VITAE

Name: Mr. Chinawat Ekwongsa

Education Background:

2011-2015 B. Sc. (Physics) Khon Kean University with scholarship from the Development and Promotion of Science and Technology Talents Project (DPST), Khonkean, Thailand.

2015-2021 Ph. D. (Physics) Suranaree University of Technology with the Development and Promotion of Science and Technology Talents Project (DPST), Nakorn Ratchasima, Thailand.

Academic Experience:

1. Research Assistant at Synchrotron Light Research Institute (Public Organization), Thailand.
2. Teaching Assistant at Laboratory, School of Physics, Suranaree University of Technology, Thailand.